

**DIGITAL OUTCROP MODELING OF THE EARLY TRIASSIC UPPER  
KHARTAM MEMBER OF KHUFF FORMATION; IMPLICATIONS FOR  
RESERVOIR HETEROGENEITY AND QUALITY, CENTRAL SAUDI  
ARABIA**

BY

Mutasim Sami Mutasim Osman

A Thesis Presented to the  
DEANSHIP OF GRADUATE STUDIES

**KING FAHD UNIVERSITY OF PETROLEUM & MINERALS**

DHAHRAN, SAUDI ARABIA

In Partial Fulfillment of the  
Requirements for the Degree of

**MASTER OF SCIENCE**

In

**GEOLOGY**

MAY 2014

KING FAHD UNIVERSITY OF PETROLEUM & MINERALS

DHAHRAN- 31261, SAUDI ARABIA

**DEANSHIP OF GRADUATE STUDIES**

This thesis, written by **MUTASIM OSMAN** under the direction his thesis advisor and approved by his thesis committee, has been presented and accepted by the Dean of Graduate Studies, in partial fulfillment of the requirements for the degree of **MASTER OF SCIENCE IN GEOLOGY**.



Dr. Osman M. Abdullatif  
(Advisor)



Dr. Abdulaziz M. Al-Shaibani  
Department Chairman



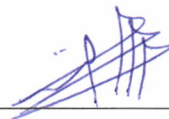
Dr. Salam A. Zummo  
Dean of Graduate Studies



Dr. Gabor Korvin  
(Member)

9/6/14

Date



Dr. Mohammed S. Al-Farhan  
(Member)

©Mutasim Osman

2014

*Dedication*

*To my dear Mother and dear Father*

*To my Sisters and Brothers*

*To all my Family and Relatives*

*To my Fiancée*

*To all Friends in my life*



## **ACKNOWLEDGMENTS**

I would like to thank the Earth Sciences Department at KFUPM for their support during my master program. Great thanks and appreciation goes for my thesis committee represented by Dr. Osman Abdullatif, Prof. Gabor Korvin and Dr. Mohammed Al-Farhan for their guidance, support and patience.

I also would like to acknowledge funding and support of the Deanship of Scientific Research for this work provided by King Abdulaziz City for Science and Technology (KACST) through the Science & Technology Unit at the King Fahd University of Petroleum and Minerals (KFUPM) and project No. 10-OIL1379-04 as part of the National Science, Technology and Innovation Plan. Special thanks goes to the team group participated in the field work from LiDAR and Hyperspectral Research Laboratory, KACST and KFUPM.

I would like to acknowledge my colleagues at the ESD for their help and support and also thanks to the Sudanese community at KFUPM.

# TABLE OF CONTENTS

ACKNOWLEDGMENTS .....	V
TABLE OF CONTENTS .....	VI
LIST OF TABLES .....	IX
LIST OF FIGURES .....	X
ABSTRACT .....	XVII
ملخص الرسالة .....	XIX
CHAPTER 1 INTRODUCTION .....	1
1.1 Introduction .....	1
1.2 Problem Statement .....	4
1.3 Objectives .....	5
1.4 Study Area .....	7
CHAPTER 2 LITERATURE REVIEW .....	12
2.1 Introduction .....	12
2.2 Tectonic Setting and Paleogeography of the Arabian Plate .....	12
2.3 Stratigraphy of Khuff Formation .....	19
2.4 Permian – Triassic Khuff Reservoirs .....	27
2.5 Terrestrial Laser Scanning .....	32
CHAPTER 3 METHODOLOGY .....	39
3.1 Introduction .....	39
3.2 Sedimentological and Stratigraphical Analysis .....	40
3.3 Spectrum Gamma Ray Analysis .....	40

<b>3.4</b>	<b>Laboratory and Petrophysical Analysis.....</b>	<b>41</b>
<b>3.5</b>	<b>Digital Outcrop Modeling (DOM) .....</b>	<b>44</b>
3.5.1	Digital Data Collection .....	44
3.5.2	Processing of the Digital Data .....	48
3.5.3	Interpretation of the Digital Model .....	53
<b>CHAPTER 4</b>	<b>SEDIMENTOLOGY AND STRATIGRAPHY .....</b>	<b>54</b>
<b>4.1</b>	<b>Introduction .....</b>	<b>54</b>
<b>4.2</b>	<b>The Permian\Triassic Boundary Interval .....</b>	<b>55</b>
<b>4.3</b>	<b>Facies Analysis and Interpretation .....</b>	<b>59</b>
4.3.1	Poorly sorted intraclasts packstone.....	70
4.3.2	Graded mudstones and wackestones to packstones .....	70
4.3.3	Shoal complex association .....	74
4.3.4	Thin marl limestone alternating with grainstones .....	76
<b>4.4</b>	<b>High Resolution Stratigraphy.....</b>	<b>83</b>
<b>4.5</b>	<b>Interpretation and Discussion.....</b>	<b>88</b>
<b>CHAPTER 5</b>	<b>DIGITAL OUTCROP MODEL.....</b>	<b>93</b>
<b>5.1</b>	<b>Introduction .....</b>	<b>93</b>
<b>5.2</b>	<b>Field Planning .....</b>	<b>93</b>
<b>5.3</b>	<b>Digital Data Acquisition .....</b>	<b>96</b>
<b>5.4</b>	<b>Digital Data Processing .....</b>	<b>99</b>
<b>5.5</b>	<b>Interpretation of the Digital Model .....</b>	<b>116</b>
<b>5.6</b>	<b>Interpretation and Discussion.....</b>	<b>133</b>
<b>CHAPTER 6</b>	<b>RESERVOIR HETEROGENEITY AND QUALITY .....</b>	<b>135</b>
<b>6.1</b>	<b>Introduction .....</b>	<b>135</b>
<b>6.2</b>	<b>Data from Reservoir Unit A .....</b>	<b>139</b>
<b>6.3</b>	<b>Data from Reservoir Unit B .....</b>	<b>145</b>
<b>6.4</b>	<b>Data from Reservoir Unit C .....</b>	<b>151</b>
<b>6.5</b>	<b>Interpretation and Discussion.....</b>	<b>157</b>

<b>CHAPTER 7 CONCLUSIONS AND RECOMMENDATIONS .....</b>	<b>160</b>
<b>7.1 Conclusions .....</b>	<b>160</b>
<b>7.2 Recommendations .....</b>	<b>161</b>
<b>REFERENCES.....</b>	<b>162</b>
<b>VITAE.....</b>	<b>175</b>

## LIST OF TABLES

Table 2.1	Some of the published studies about Khuff Formation in the Middle East .....	31
Table 4.1	Summary of the lithofacies reported in this study and their description and interpretation .....	89
Table 4.2	A comparison between lithofacies associations for Upper Khartam Member in Saudi Arabia and its equivalent in Oman .....	92
Table 5.1	Average thickness for every bed from the field and from the ArcMap software. ....	131
Table 6.1	The key used to evaluate the reservoir heterogeneity .....	138
Table 6.2	A: The measurements of the first reservoir unit A; B: statistical parameters of the reservoir unit A .....	140
Table 6.3	A: The measurements of the second reservoir unit B; B: statistical parameters of the reservoir unit B .....	146
Table 6.4	A: The measurements of the third reservoir unit C; B: statistical parameters of the reservoir unit C .....	152
Table 6.5	A comparison between the three reservoir units .....	159

## LIST OF FIGURES

Figure 1.1	Different scale of heterogeneities from mm scale (thin section) to 1000 km scale (basin) (Martinius et al., 2007) .....	6
Figure 1.2	Geological map of the Arabian Peninsula showing the distribution of the lithological units, the Khuff Formation belt illustrated in purple (Powers, 1968).....	8
Figure 1.3	The distribution of the outcrops of the Khuff members in Buraydah quadrangle, Qasim area (Vaslet et al., 2005) .....	9
Figure 1.4	The location of the study area in Buraydah quadrangle NW of Riyadh; A: map showing the Qasim area; B: map showing Buraydah quadrangle; C: close view to the location of the outcrop (Google earth, 2014).....	10
Figure 1.5	Part of the outcrop of Upper Khartam Member of Khuff Formation in Al-Tarafiyah town, Buraydah quadrangle, Qasim, Central Saudi Arabia .....	11
Figure 2.1	The accretionary evolution of Arabian Shield (Al-Husseini, 2000).....	14
Figure 2.2	The main structural elements of the Arabian plate (Al-Husseini, 2000).....	15
Figure 2.3	Paleolatitude positions of the Arabian Plate during the Paleozoic (Konert et al., 2001) .....	17
Figure 2.4	Regional correlation of the chronostratigraphy of the lithostratigraphic units of the Khuff Formation in the outcrop compared to subsurface composition in Saudi Arabia, Oman, UAE and Iran. Note that the study interval (Khartam Member) is highlighted by yellow (Eltom et al., 2014b) .....	18
Figure 2.5	Environments of deposition and major facies of the Khuff Formation and equivalents in the Arabian Plate (Ziegler, 2001) .....	21
Figure 2.6	The composite section of Khuff Formation in Buraydah quadrangle (Vaslet et al., 2005) .....	22
Figure 2.7	The evolution of the Khuff transgression through the deposition of: (a) Al-Shiqqah and Huqayl members; (b) Huqayl and Dhahisan members, and the evolution of the Khuff regression during the deposition of: (c) Midhnab Member, and (d) Khartam member (Vaslet et al., 2005).....	26

Figure 2.8	Part of a generalized Paleozoic stratigraphic column for Saudi Arabia showing the stratigraphic position and the reservoir units of Unayzah and Khuff Formations (after Dasgupta et al., 2002).....	28
Figure 2.9	The LiDAR system instrument Optech with an attached digital camera in front of the Upper Khartam outcrop .....	34
Figure 3.1	Portable Spectral Gamma Ray SGR Gamma GF Surveyor II logging tool .	43
Figure 3.2	LiDAR workflow from the collection of the data to the interpretation for the final model (modified from Bellian et al., 2002) .....	45
Figure 3.3	Tripod Riegl VZ-4000 laser scanner mounted on the ground in front of the Upper Khartam outcrop .....	47
Figure 3.4	Tripod prism reflector mounted in front of Upper Khartam outcrop .....	50
Figure 4.1	A: Outcrop photograph shows the carbonates of Upper Khartam and the yellow dolomitic mudstone of the Lower Khrtam Member and the red claystone interval; B: spectral gamma-ray (SGR) logs for U, Th, K from the outcrop (after Eltom et al., 2014b).....	57
Figure 4.2	A: The total GR in API for SGR logs from the study area; B: digitized published GR in API logs of Upper Khuff equivalent outcrop in UAE (Maurer et al., 2009) (Eltom et al., 2014b) .....	58
Figure 4.3	The field description of the vertical section KM-1 and the structures appearing on it along with the gamma ray data and porosity and permeability data .....	61
Figure 4.4	The porosity-permeability relationship within the strata in the vertical section KM-1.....	62
Figure 4.5	The field description of the vertical section KM-2 and the structures appearing on it along with the gamma ray data and porosity and permeability data .....	63
Figure 4.6	The porosity-permeability relationship within the strata in the vertical section KM-2.....	64
Figure 4.7	The field description of the vertical section KM-3 and the structures appearing on it along with the gamma ray data and porosity and permeability data .....	66



Figure 4.8	The porosity-permeability relationship within the strata in the vertical section KM-3.....	67
Figure 4.9	The field description of the vertical section KM-4 and the structures appearing on it along with the gamma ray data and porosity and permeability data .....	68
Figure 4.10	The porosity-permeability relationship within the strata in the vertical section KM-4 .....	69
Figure 4.11	A: The Permian\Triassic boundary interval, B and C: outcrop photographs for intraclasts bed (marine ravinments); (D) thin-section photomicrograph of a sample from this bed. Note the angular clasts in (B) and (C) and fine quartz in (D).....	72
Figure 4.12	(A) and (B) outcrop photographs for the stacked beds of graded mudstones to packstones lithofacies. The sedimentary structure in this lithofacies includes (C) horizontal lamination; (D) climbing lamination; (E) and (F) low angle trough crossbedding; (G) to (I) The dominant grain types are very fine to fine ooids, detrital peloids and calcisiltites .....	73
Figure 4.13	Outcrop photographs show the architectures of the shoal complex facies. The top of these photographs A: show intercalated grain-dominated and mud-dominated beds. The middle of this photograph shows rippled oolitic sand overlain by relatively thick massive oolitic sand which is interpreted as stabilized shoal; The middle part of the photograph B: shows a channel cut into mud-dominated facies this was interpreted as a distal part of a channel prograding into a proximal outer shelf; The bottom part C: shows photograph of oolitic sand bars cut by channel overlain by the stabilized shoal oolitic sand (Eltom et al., 2014b) .....	78
Figure 4.14	Shoal complex lithofacies association. (A) and (B) well-preserved rippled beds intercalated with fine to very fine marl; (C) thin-section photomicrographs of fine ooids and peloids; (D) oolitic grainstone with massively bedded at the base well-preserved crossbedding at the top; (E) thin-section photomicrograph of moderately to well-sorted oolitic	

	grainstone; (G) horizontally laminated bed; (F) HCS; (I) thin-section photomicrographs of poorly sorted micritized oolitic grainstone.....	79
Figure 4.15	Microbiolites in the Upper Khartam Member. (A) plain view of thrombolites in the outcrop; (B) photomicrographs of thrombolites sample showing lamination and clotted fabric; (C) plain view of stromatolite in the outcrop .....	80
Figure 4.16	Landsat image showing general morphology of different parts of the shoal complex in Crooked-Acklins Island, Bahamas . After Rankey and Peeder (2001) and Rankey (2013) .....	81
Figure 4.17	Thin bed fine limestones alternating with grainstones. (A) alternating beds of fine grained limestone and grainstones; (B) and (C) cut and fill structures in the forms of gutter casts; (D) cut and fill structures in the forms of pot casts (Eltom et al., 2014b) .....	82
Figure 4.18	High Frequency Sequences and the stacking pattern of Upper Khartam Member (after Eltom et al., 2014b) .....	86
Figure 4.19	Depositional model (ramp complex) showing stratigraphic distribution of lithofacies along the outcrop sections of the Upper Khartam Member. Note that although HFS-1 and -2 represent the deepest part of the model, the lowermost interval of HFS-1 is interpreted as very shallow water (first transgression) (after Eltom et al., 2014b) .....	87
Figure 5.1	The planning for the LiDAR scanning in the field .....	95
Figure 5.2	Summary of the workflow for the acquisition of the digital data .....	97
Figure 5.3	The acquisition of the digital data .....	98
Figure 5.4	Summary of the workflow for the processing of the digital data .....	100
Figure 5.5	Visualizing of the colored point clouds using RiSCAN Pro software; A: the interface of the software and the map view from the point clouds; B and C: zoom out display from the target outcrop; D and E: zoom in to the face of the target outcrop of the Upper Khartam Member .....	101
Figure 5.6	Importing the ASCII files in IMAlign; A: the interface of the software and one file has been imported and displayed; B and C: different views and zoom in to the point cloud data.....	103

Figure 5.7	Cleaning the point cloud; A: selecting the undesired points; B: The selected points marked by red color; C and D: the point cloud after cleaning the point cloud .....	104
Figure 5.8	A: displaying the model on the clipping plane; B: selecting the first part to be triangulated; C: inverting the selection; D: hide the rest of the model .	105
Figure 5.9	Triangulation process; A: starting the interpolation for the previously selected part; B: the triangulated model for the same part; C: zoom in to the triangulated part, note the holes which appear in this part .....	106
Figure 5.10	A: the triangulated part of the model; B: zoom in to the rectangular part in A and it shows the triangles created by the interpolation process .....	107
Figure 5.11	A and B: triangulation for the second and the third parts of the same first point cloud file; C: the final triangulated model after combining the whole triangulated parts of the file .....	109
Figure 5.12	A: reduce the overlapping between the four triangulated scan files; B: display of the whole triangulated model.....	110
Figure 5.13	A, B and C: different views for the triangulated model showing how integrating between the four scans assist to fill in the gaps between them	111
Figure 5.14	IMEdit interface; A: visualize the model in IMEdit; B: zoom in to the final triangulated model in IMEdit.....	112
Figure 5.15	Editing the model; A: click on and select the holes appearing in the model; B: the model after filling the holes .....	113
Figure 5.16	A: exporting the polygonal model as object file; B: the draping software used to superimpose the photos of the outcrop on the model.....	114
Figure 5.17	Part of the final draped polygonal model displayed in IMEdit tool .....	115
Figure 5.18	Summary of the workflow for the interpretation of the digital data .....	117
Figure 5.19	Importing the draped polygonal model to ArcGIS; A: the interface of ArcScene tool with the model displayed on it; B and C: zoom in to the model in ArcScene.....	118
Figure 5.20	Bed surfaces delineation; A and B: the black dots point to the tracing of the surface from the beginning to the end of the bed; C: The top and bottom horizons for each bed have been traced laterally and drawn .....	119

Figure 5.21	The projected lines and the original point's line displayed clearly in this part of the model .....	120
Figure 5.22	The bed horizons on the outcrop, the highlighted aqua horizons point to the top and bottom of specific bed were selected to populate the facies code of this bed .....	122
Figure 5.23	Texture and facies digital model; A: digital model shows the texture distribution along the outcrop according to the shown legend; B and C: zoom in to the texture model using the same legend as in A; D: the lithofacies distribution along the outcrop according to the attached legend; E and F: zoom in to the same lithofacies model using the same legend as in D .....	123
Figure 5.24	The stratigraphic digital model; A: stratigraphy showing the depositional sequences and their surfaces according to the legend; B, C, D and E: show the same stratigraphy model but from different angle of views using the same legend and the highlighted surfaces are the sequences surfaces .....	124
Figure 5.25	The digital model displayed in ArcScene and the yellow axis are the two axial projection systems used to extract the traces .....	126
Figure 5.26	The two groups of traces are colored by red and blue, the axial projection systems are illustrated in yellow .....	127
Figure 5.27	The extracted traces from the model; A: ArcMap interface display of the imported shape file for the whole traces from the model; B: zoom in to the western blue traces; C: zoom in to the eastern red traces .....	128
Figure 5.28	Bed thickness measurements; A: the thickness measurements along the eastern part of the outcrop; B: the thickness measurements along the western part of the outcrop .....	129
Figure 5.29	Summary of the workflow from the acquisition of the digital data to the build and interpretation of the photorealistic model .....	132
Figure 6.1	Cross plots for unit A; A: the distribution of the porosity values along the lateral profile; B: the distribution of the permeability values along the lateral profile; C: histogram for the porosity data; D: histogram for the permeability data .....	141

Figure 6.2	Cross plots for unit A; A: porosity vs permeability data; B: RQI vs $\Phi_z$ data .....	142
Figure 6.3	Thin sections, SEM and XRD analysis for the selected samples from the reservoir unit A .....	144
Figure 6.4	Cross plots for unit B; A: the distribution of the porosity values along the lateral profile; B: the distribution of the permeability values along the lateral profile; C: histogram for the porosity data; D: histogram for the permeability data .....	147
Figure 6.5	Cross plots for unit B; A: porosity vs permeability data; B: RQI vs $\Phi_z$ data .....	148
Figure 6.6	Thin sections, SEM and XRD analysis for the selected samples from the reservoir unit B .....	150
Figure 6.7	Cross plots for unit C; A: the distribution of the porosity values along the lateral profile; B: the distribution of the permeability values along the lateral profile; C: histogram for the porosity data; D: histogram for the permeability data .....	153
Figure 6.8	Cross plots for unit C; A: porosity vs permeability data; B: RQI vs $\Phi_z$ data .....	154
Figure 6.9	Thin sections, SEM and XRD analysis for the selected samples from the reservoir unit C .....	156

## ABSTRACT

Full Name : Mutasim Sami Mutasim Osman  
Thesis Title : Digital Outcrop Modeling of The Early Triassic Upper Khartam  
Member of Khuff Formation; Implications for Reservoir Heterogeneity  
and Quality, Central Saudi Arabia  
Major Field : Geology  
Date of Degree : May 2014

The Permian – Triassic Khuff Formation is considered to be the most prolific for the natural gas production in the world, 43% of the natural gas reserve. The Khuff reservoirs exhibit vertical and lateral heterogeneities which cannot captured fully within the inter-well spacing from the subsurface data. The outcrop of the Upper Khartam Member in Central Saudi Arabia represents an excellent analog for the upper parts of Khuff-Band the whole Khuff-A reservoirs. The main objective of this work is to investigate the reservoir heterogeneity and quality and to reconstruct digital outcrop model of the Upper Khartam Member. This study included sedimentological, stratigraphical and digital laser scanning (LiDAR) modeling. Detailed laboratory analyses were carried out using thin sections, SEM and XRD investigations in this work. Four vertical stratigraphic sections were implemented to cover the whole outcrop of Upper Khartam and a composite section was constructed. Three horizontal stratigraphic sections were also investigated along three reservoir bodies named from bottom to top A, B and C within Upper Khartam and 80 samples were collected. The composite section bounded at the bottom by the Permian\Triassic boundary and at the top by a sequence boundary within the Upper Khartam Member. The investigations revealed that the studied part of Upper Khartam comprising of six lithofacies association deposited in three depositional settings. The

depositional environments are: marine transgression, fore shoal and shoal complex. The high resolution stratigraphic study infers that Upper Khartam consists of three high frequency sequences (HFSs) those are from bottom to top HFS-1, HFS-2 and HFS-3. Each depositional sequence bounded at the bottom and top by sequence boundary. The terrestrial laser scanner was used to scan the outcrop from four different scan positions. The Polyworks software was used for the processing and to produce the photorealistic model for Upper Khartam. ArcGIS combined with the Geo Analysis Tool were utilized to interpret the digital models. Both the digital facies and stratigraphic models covered the part of the outcrop that shows the upper portion of HFS-1 and entire HFS-2 and HFS-3. The digital modeling allows accurate structural and statistical measurements of lithofacies and integrated with the traditional field data on it and examined the lateral continuity and the architecture of the strata in the outcrop. The results show variability in reservoir heterogeneity and quality from extremely heterogeneous in unit C to very heterogeneous in units A and B. The main controls on reservoir heterogeneity are depositional and post-depositional diagenesis at outcrop scale. The integration of the results of this work with subsurface data might help to provide better understanding and prediction of the quality of Khuff reservoirs in the subsurface.



## ملخص الرسالة

الاسم الكامل: معتصم سامي معتصم عثمان

عنوان الرسالة: نمذجة رقمية للمتكشف الصخري خرطم الأعلى (الترياسي الأولي) من متكون الخف: تضمين لخصائص ونوعية المكن، وسط المملكة العربية السعودية

التخصص: ماجستير العلوم في الجيولوجيا

تاريخ الدرجة العلمية: مايو ٢٠١٤

يعتبر متكون الخف البرمي – الترياسي مكن مهم للغاز الطبيعي في العالم حيث يحتوي على ٤٣ % من احتياطي الغاز. يمثل متكشف خرطم الأعلى شبيها سطحيًا جيدًا للجزء الأعلى من مكن الخف ب و مكن الخف أ تحت سطح الأرض. تهدف هذه الرسالة إلى دراسة تباين خصائص ونوعية صخور المكن وعمل نموذج رقمي لمتكشف خرطم الأعلى. تحتوي الدراسة على طرق بحث رسوبية وطبقية حقلية ومعملية ومع تقنية ونمذجة الليدار الأرضي. احتوت التحاليل المعملية على استخدام التحليل البتروغرافي وتحليل تشتت الأشعة السينية (X-RD) وتحليل المايكروسكوب الإلكتروني الماسح (SEM). اعتمد التحليل السحني الحقلية على أربعة قطاعات رأسية في المتكشف الصخري. ثلاثة قطاعات أفقية أيضًا تم عملها على طول ثلاثة وحدات مكنية سميت أ، ب و ج من الأسفل إلى الأعلى ولقد تم جمع وتحليل ٨٠ عينة منها. يشير التحليل السحني إلى وجود ستة مجموعات سحنية ترسبت في ثلاث بيئات رسوبية وهي بيئة البحر المتقدم، والشول الأمامي و مجموعة الشول. التحليل الطبقي يشير إلى وجود ثلاثة تتابعات طبقية دقيقة. لقد مكنت تقنية الليدار الأرضي في متكشف خرطم من تأسيس نمذجة رقمية دقيقة وقياسات تركيبية وإحصائية للسحنات وتكاملها مع المعلومات الحقلية من حيث الامتداد الرأسي والأفقي ومعمارية الطبقات. تشير دراسة أجسام المكن الثلاثة أ، ب و ج إلى تنوع خصائص تلك الأجسام حيث كان المكن ج هو الأعلى تباينًا ويقل التباين في أ و ب. وهذا التنوع ناتج من عمليات الترسيب وعمليات النشأة المتأخرة. تكامل نتائج دراسة النمذجة لمتكشف خرطم مع

المعلومات التحت سطحية ربما يساعد على فهم وتنبؤ أفضل عن نوعية مكن الخف تحت سطح الأرض.

# CHAPTER 1

## INTRODUCTION

### 1.1 Introduction

The economic requests to increasing the production of oil and gas fields and the recent technological developments have led to an evolution of more advanced techniques. Understanding the reservoir properties and efficiency is playing a major role in the exploration and the development stages of oil and gas production. This has led to development of reservoir characterization and geological modelling (Jia et al., 2012; Eltom et al., 2014a). The Permian – Triassic carbonates of Khuff reservoirs and equivalents in Saudi Arabia and other Middle East countries are estimated to contain about 43% of the world's natural gas reserves (BP Statistical Review of World Energy, 2013). The deficiency of techniques and difficulty to define the accurate reservoir heterogeneity in the subsurface promote the utilization of surface outcrop analogs (Pranter et al., 2006). Recently, terrestrial laser scanning LiDAR (Light Detection And Ranging) technique has become widely used in digital outcrop stratigraphic imaging and modeling. When combined with directly sampled data, digital modeling can generate high-precision facies models. Also, it helps in constructing 3D outcrop-based geological models which can improve the understanding of the geologic and flow simulation

(Pringle et al., 2004, 2006; Bellian et al., 2005; Enge et al., 2007; Al-Farhan, 2010; Fabuel-Perez et al., 2010; Jia et al., 2012; Hodgetts, 2013).

Outcrop analogs provide precious information that could help in characterizing the facies boundaries, internal facies distribution, and their high-frequency cycles (Lindsay and Hughes, 2010; Eltom et al., 2014a). Also, the outcrop analogs reveal valuable information regarding potential reservoir units, such as; dimensions of geobodies, their volume, orientation in 2D or 3D, and the by-products of the diagenesis; which are difficult to acquire from the subsurface (Eltom et al., 2012). All these lead to better understanding of the reservoir sedimentology, stratigraphy and heterogeneity, and their effect on the reservoir quality and architecture. Consequently, this will assist to obtain more accurate results in reservoir characterization and permit decision makers to take confident solutions related to the development and management of oil and gas reservoirs (Hodgetts, 2013).

Many previous studies have indicated that the application of digital outcrop analog modeling for reservoir characterization is suitable in numerous aspects as follows:

- Provides better understanding of facies architecture and environment.
- Determines the geometry of the rock bodies within the reservoir.
- Describes the reservoir heterogeneity in different scales.
- Provides correlation guidelines.
- Helps to interpret the controls on sediment architecture.

In Saudi Arabia, excellent outcropping strata equivalent to the Paleozoic Formations are exposed in a curve belt extending from South West to North West of Saudi Arabia (Al-Dukhayyil, 2007). These outcropping strata provide good opportunity to characterize and model their subsurface equivalents. The well exposed Permian – Triassic Khuff carbonates in central Saudi Arabia offer good outcrop analog to some of the subsurface Khuff reservoirs (Vaslet et al., 2005). The Khuff Formation reservoirs and their equivalent stratigraphic units occur in Saudi Arabia, Oman, United Arab Emirates, Iran, Bahrain, and Qatar (Beydoun 1989; Alsharhan and Narin, 2003; Al-Husseini, 2004; Al-Dukhayyil, 2007; Al-Dukhayyil and Al-Tawil, 2007). The geological understanding of Khuff Formation in Saudi Arabia is vital and of great importance for exploration, development and management of its hydrocarbon resources. The study of the Khuff Formation reservoirs has been a challenge due to the complexity of facies as a result of depositional and post-depositional controls (Janson et al., 2013). Therefore, detecting and defining the geological heterogeneity at micro- and macro-scale, facies and stratigraphic hierarchy will help to assess reservoir architecture and quality. Also, evaluating their effectiveness in exploration and development will lead to enhance the economic hydrocarbon production from the Khuff reservoirs. The Khuff reservoir analogs will allow examining and assessing geological heterogeneity that is hard to assess and evaluate from subsurface because of the limitations of data and methods of investigations (Janson et al., 2013). This study aims to conduct Terrestrial LiDAR scanning, sedimentological, stratigraphical and petrophysical studies using strata in Qasim area in Central Saudi Arabia which are equivalent outcrop analogs for the upper parts of Early Triassic Khuff-B and the whole Khuff-A reservoirs in the subsurface (Al-Dukhayyil,

2007; Al-Dukhayyil and Al-Tawil, 2007). This study is valuable also in the field of applying and developing new data-integration technology (LiDAR) related to the Kingdom's energy resources.

## **1.2 Problem Statement**

Because of the known complexity in the carbonate reservoirs around the world, they are difficult to characterize in terms of heterogeneity at different scale of observations (Figure 1.1). Generally, the heterogeneity within the carbonate reservoirs is difficult to understand from the subsurface because of the limitations of the data and hence for the Khuff-B and Khuff-A reservoirs in the subsurface (Janson et al., 2013). This heterogeneity is either depositional or diagenetical (post - depositional) and happens in different scales from mm to km and it has a major effect on the reservoir architecture and quality. In this study a digital outcrop analog model for Upper Khartam Member of Khuff Formation integrated with the geological data were conducted to test the reservoir heterogeneity at different scales. Digital modeling, and computer-based processing and interpreting were utilized in this research. Also, sedimentological, petrophysical and outcrop Spectrum Gamma Ray (SGR) logging were conducted and included in the study framework. The toolbox defined in this research was considered to answer two main research questions related to the modeling of outcrop analogs.

This study is designed to answer the following research questions:

- Can the High Resolution Stratigraphy (HRS) of the Upper Khartam Member of Khuff Formation be enhanced through the application of integrated outcrop study using LiDAR, petrophysical and SGR data?
- What are the new geological insights that can be obtained from the study of Upper Khartam Member outcrop to improve the understanding of reservoir heterogeneity and continuity?

### **1.3 Objectives**

This integrated outcrop analog study is expected to provide better understanding and prediction for the heterogeneity within the Upper Khartam Member in different scales. This might be useful to understand the heterogeneity within the equivalent Khuff-B and Khuff-A reservoirs. The main goals of this study are:

- Establish high resolution stratigraphy for Upper Khartam Member based on the field geological data.
- Characterize the reservoir heterogeneity at outcrop scale of lithofacies, cyclicity and facies continuity; and at micro scale by examining microfacies and petrophysical properties.
- Establish high resolution digital outcrop analog model for Upper Khartam Member using LiDAR, field and laboratory data.



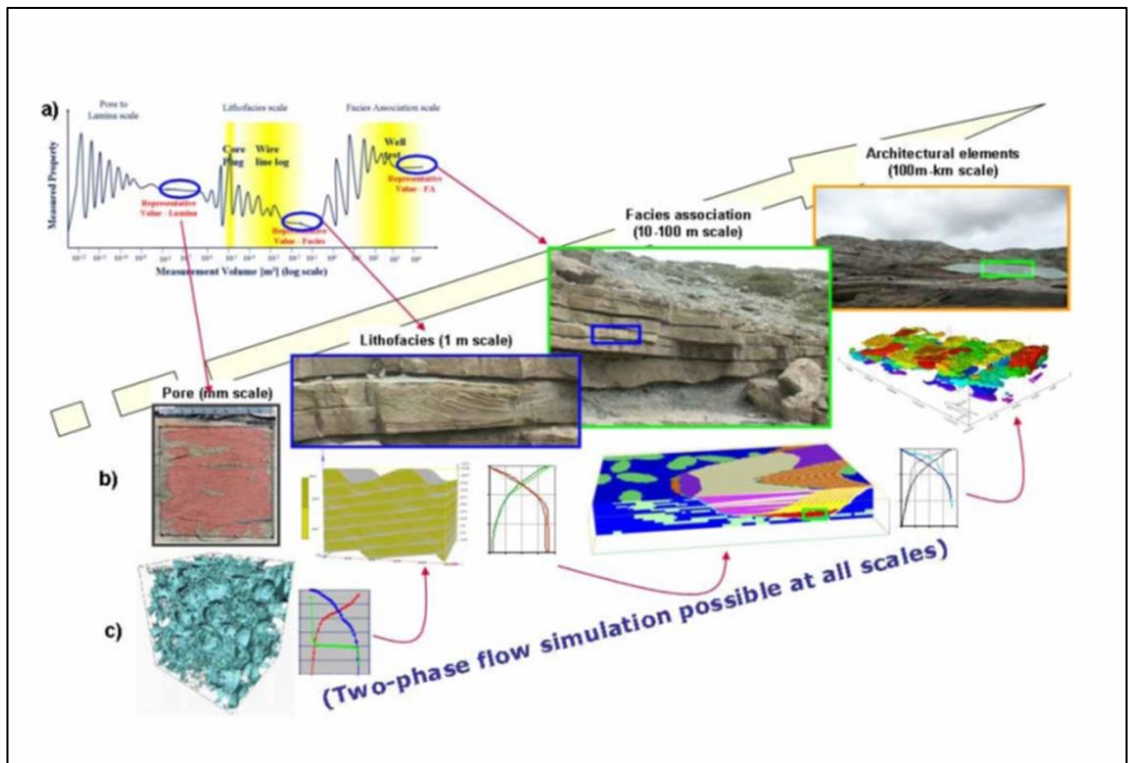


Figure 1.1 Different scale of heterogeneities from mm scale (thin section) to 1000 km scale (basin) (Martinius et al., 2007)

## **1.4 Study Area**

The outcrops of the Khuff Formation are well exposed in an arch belt extending from the North West to the South West of Saudi Arabia and bordering the Arabian Shield (Figure 1.2) and (Figure 1.3).

One of the excellent outcrops for Khuff Formation is found NW to Riyadh especially in the Buraydah quadrangle. The study area is located in Al-Tarafiyah town in Buraydah Quadrangle (Figure 1.4), Qasim area, central Saudi Arabia. In this location, Khartam Member of Khuff Formation is well exposed as a road cut (Figure 1.5).

The area is approximately peneplain with some hills around the road cut and this town is little populated. The dip of the outcrop is to the east so the general drainage in the region follows the same direction.

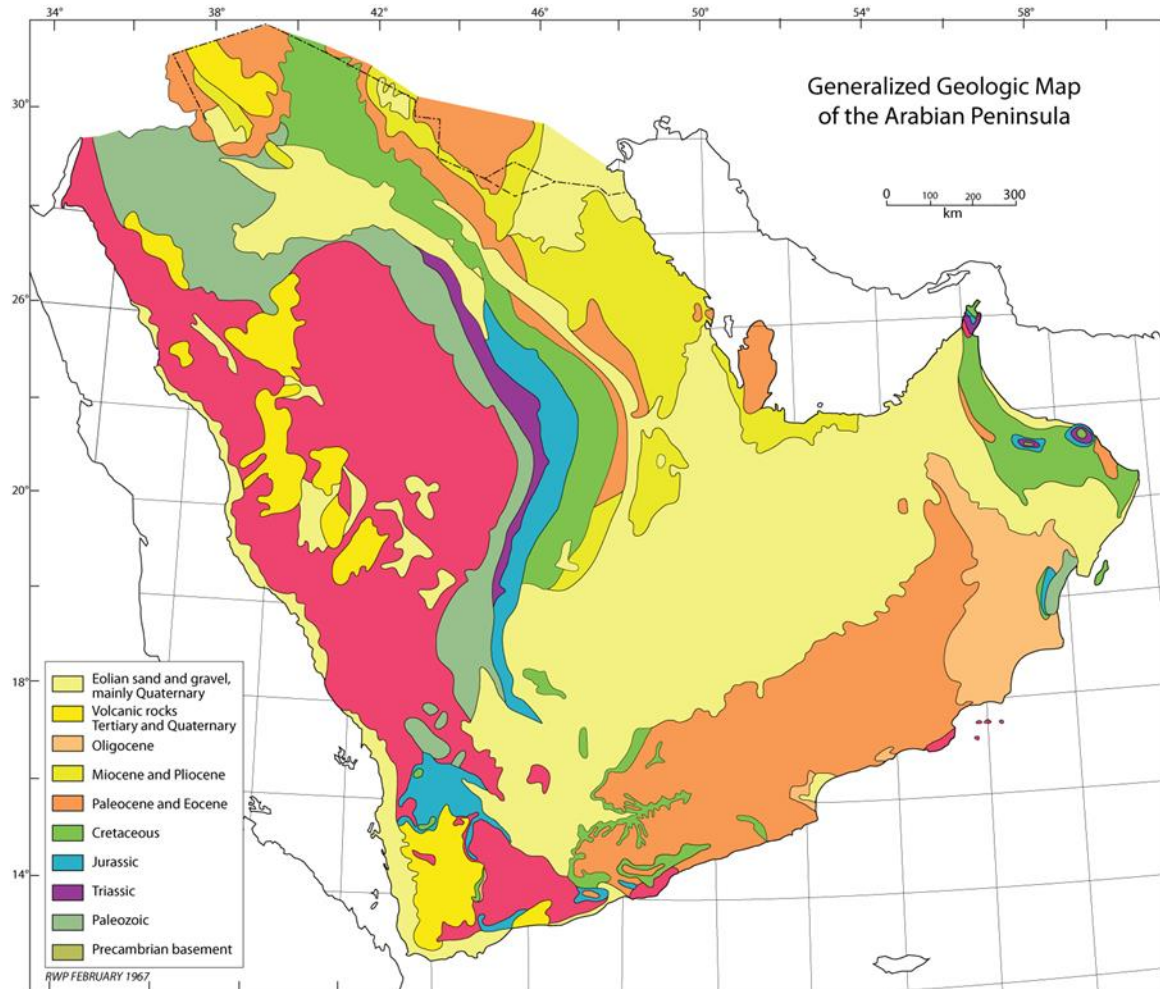


**Figure 1.2 Geological map of the Arabian Peninsula showing the distribution of the lithological units, the Khuff Formation belt illustrated in purple (Powers, 1968)**

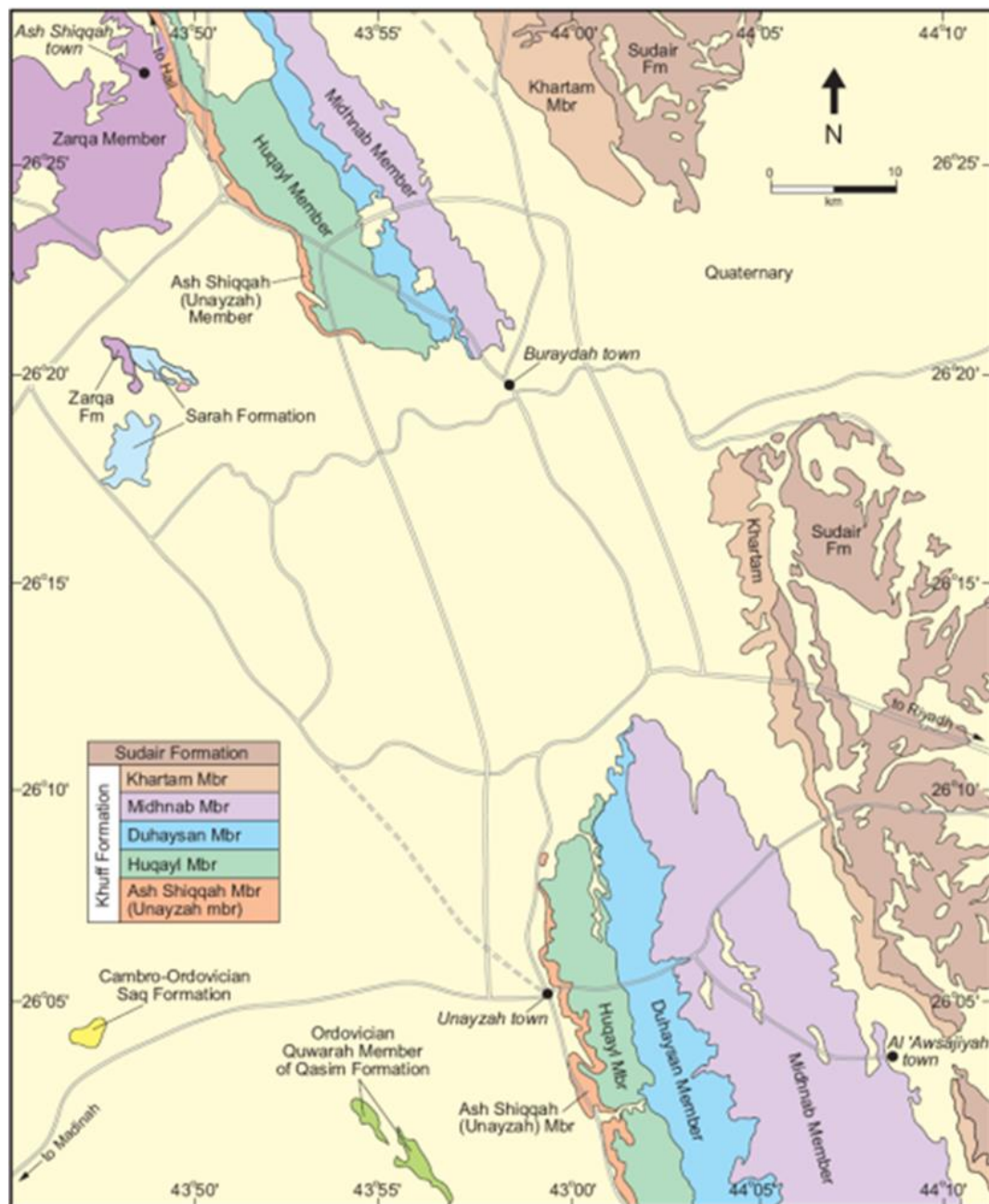
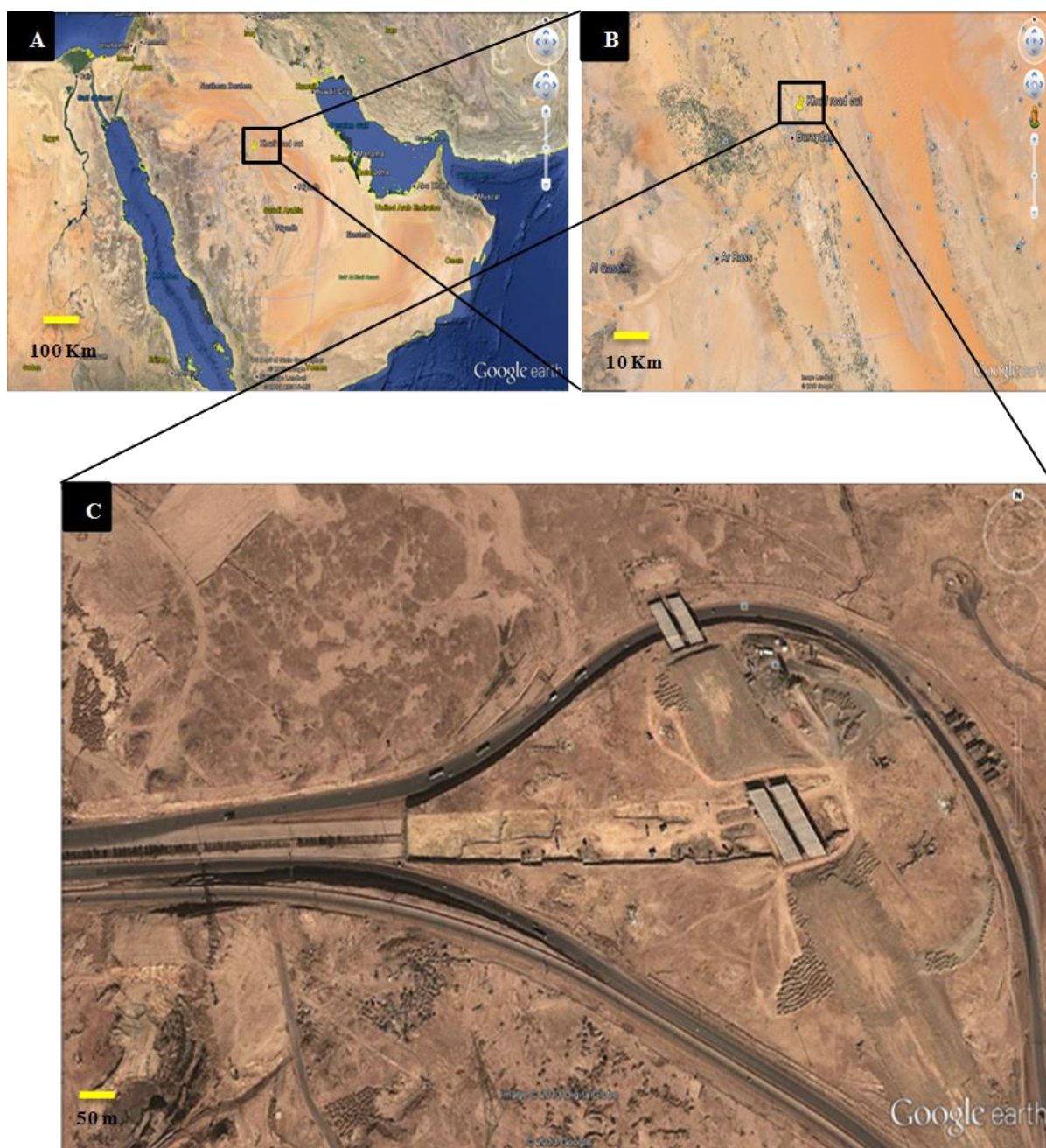


Figure 1.3 The distribution of the outcrops of the Khuff members in Buraydah quadrangle, Qasim area (Vaslet et al., 2005)





**Figure 1.4** The location of the study area in Buraydah quadrangle NW of Riyadh; A: map showing the Qasim area; B: map showing Buraydah quadrangle; C: close view to the location of the outcrop (Google earth, 2014)



**Figure 1.5 Part of the outcrop of Upper Khartam Member of Khuff Formation in Al-Tarafiyah town, Buraydah quadrangle, Qasim, Central Saudi Arabia**

## **CHAPTER 2**

### **LITERATURE REVIEW**

#### **2.1 Introduction**

The Arabian plate is considered to be the most important one in the field of oil and gas exploration and production that because the Gulf countries are the largest producers of oil and gas in the world, oil in Saudi Arabia and gas in Qatar. This section will summarize the literature on tectonic setting, paleogeography, Khuff Formation and Khartam Member sedimentology and stratigraphy in the outcrop and subsurface.

#### **2.2 Tectonic Setting and Paleogeography of the Arabian Plate**

The consolidation of the Arabian Shield in the eastern part during the Late Precambrian took place by the accretions between the micro-plates. The most important Amar collision was before 640 – 620 Ma, when the Al-Rayn micro-plate moved westward and collided with the Arabian Shield through the N – S Amar suture (Figure 2.1). This collision formed a number of anticlines that extend N – S and were surrounded by NE Bin Batin and NW Abu Jifan faults (Al-Husseini, 2000). Then, a stage of extension occurred, due to A-type granitic pluton, causing some collapse in the shield. The last stage of that extension resulted in the Najd fault system that moved the whole area in a

left-lateral side about 300 km; this caused rifts to form in NE direction (Al-Husseini, 2000). The main structural elements in the Arabian plate, then, had three main trends: North trending system, Northwest trending system and Northeast trending system (Figure 2.2). The intercalation between the three fault systems resulted in a jointed and complex basement architecture that has been reactivated by subsequent younger deformations (Konert et al., 2001). The Hercynian collision during the Late Paleozoic led to reactivation of basement fault systems and formed main NS-trending and basement-involved horst blocks in the eastern and central Saudi Arabia. A break-up unconformity identified as “Pre-Khuff Unconformity” and has the age of 255 Ma, indicates the start of the Neo-Tethys Ocean along the Oman – Zagros suture where the greatest wide transgression had arisen causing the development of the Neo-Tethys Ocean (Al-Aswad, 1997 and Konert et al., 2001).



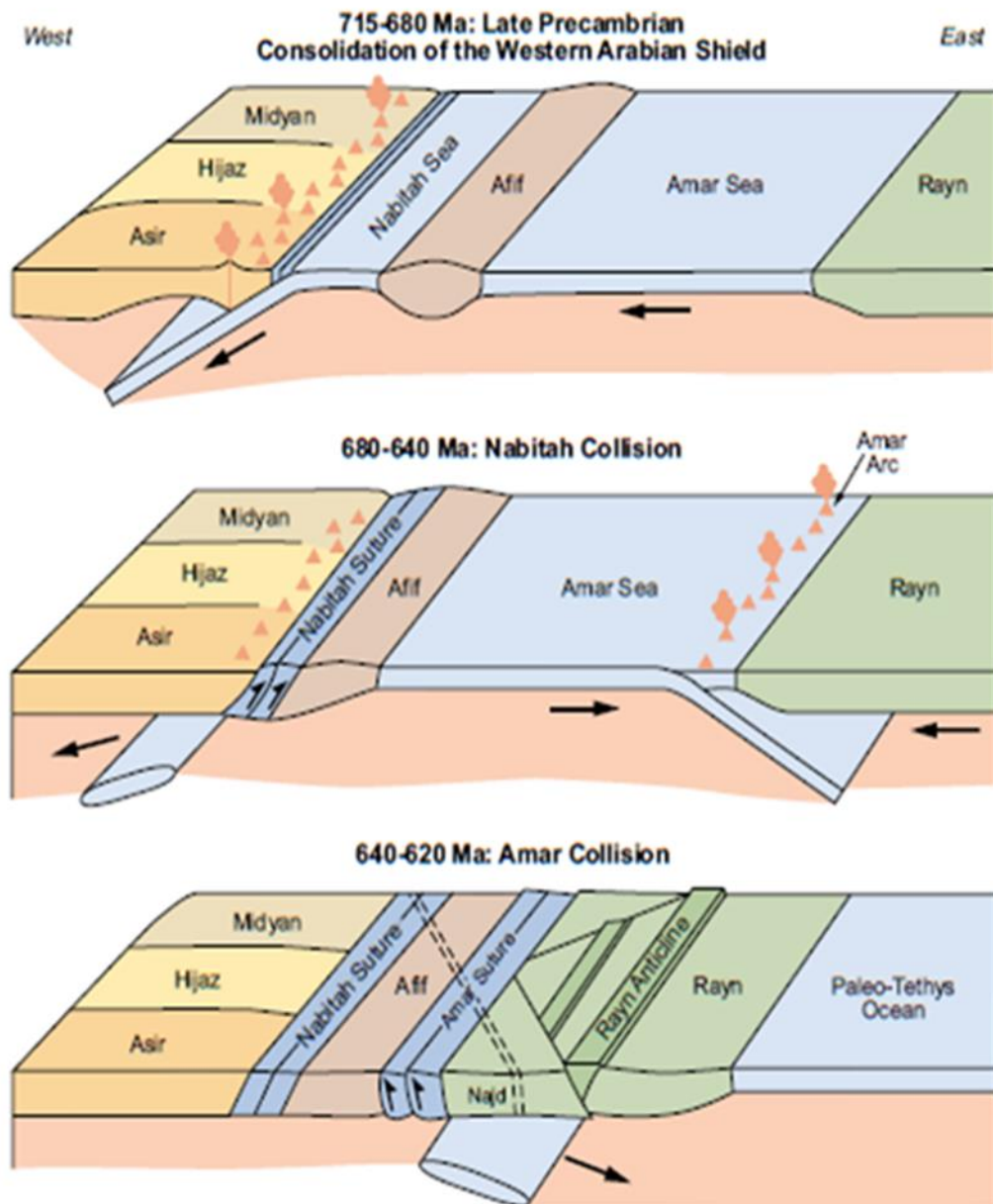
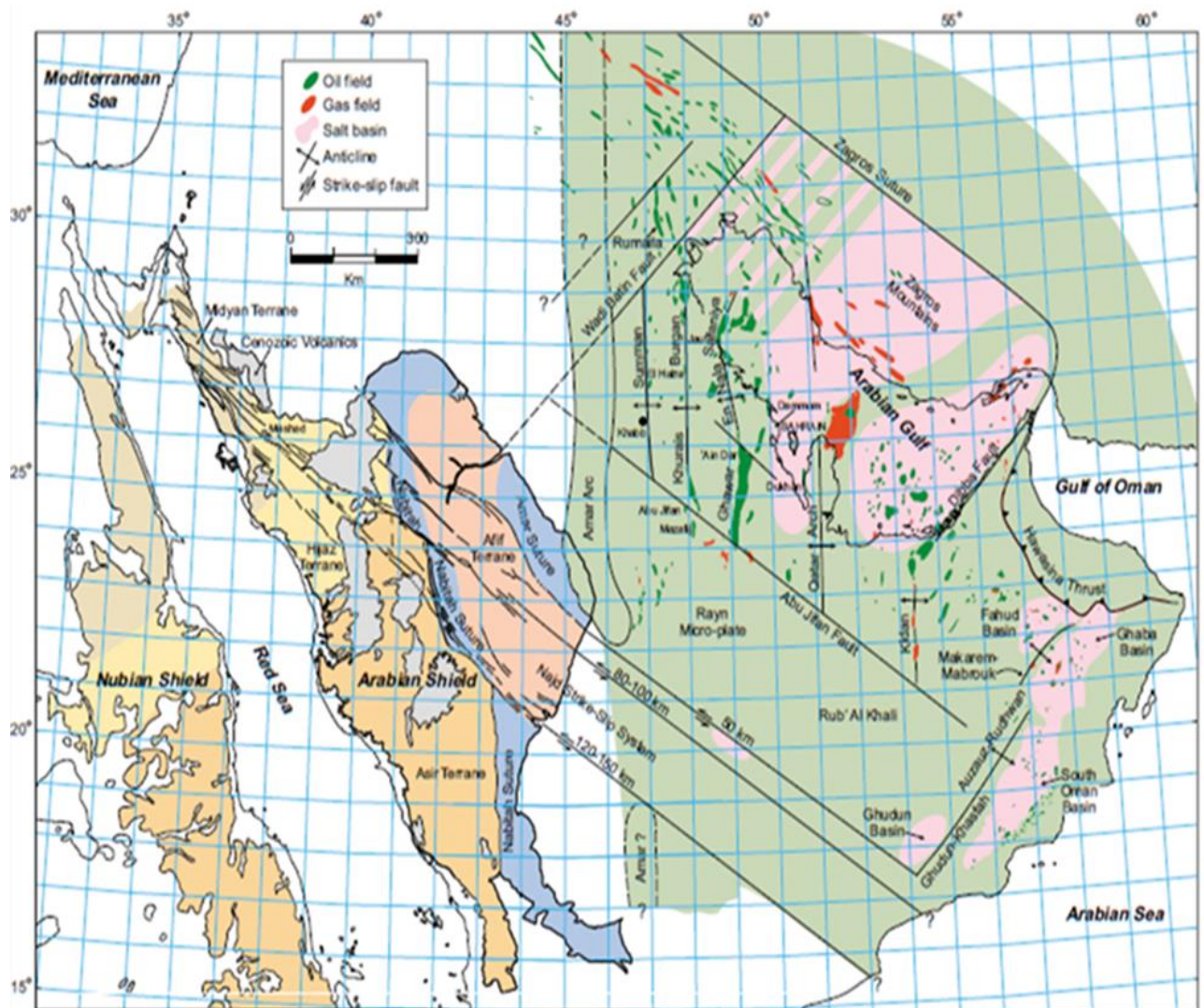


Figure 2.1 The accretionary evolution of Arabian Shield (Al-Husseini, 2000)



The Arabian Plate passed through different positions from the Proterozoic to the Phanerozoic in an arcwise movement. During the Permian the Arabian Plate moved rapidly to the north and reached the equator in the Early Triassic (Konert et al., 2001) (Figure 2.3). The Late Permian time marks a major change in sedimentation from dominantly clastic to commonly carbonate. During this epoch, the sea spread over much of the Arabian foreland and there deposited a sheet of shallow-water limestone that extends from South East Turkey, Iran, Saudi Arabia to Oman (Figure 2.4) (Ziegler, 2001). Khuff Formation belongs to the tectono-stratigraphic megasequence AP6 which lasted about 73 my and dominated by thick Permo-Triassic platform and ramp carbonates with minor evaporites and clastics (Sharland et al., 2001).

The paleogeographic setting of the Arabian Plate during Khuff time is characterized by rapid thermal collapse of the new northeast Arabian passive margin and continuing northward continental drift (Al-Jallal, 1995). This resulted in widespread early Late Permian Khuff transgression and development of new passive margins with Neo-Tethys expressed by very rapid subsidence. This subsidence led to a major marine transgression and deposition of the Khuff Formation (Al-Jallal, 1995). Several authors have studied marine fossils (macro- and micro- invertebrates) in Khuff outcrops in central Saudi Arabia. These studies revealed similarities and correlations of these fossils with the associations in the Arabian platform and the western Tethyan realm. This allowed establishing paleoecological and paleobiogeographical relationships between different Palaeo-Tethyan areas (Vachard et al., 2005; Angiolini et al., 2006; Chirat et al., 2006; Crasquin-Soleau et al., 2006).

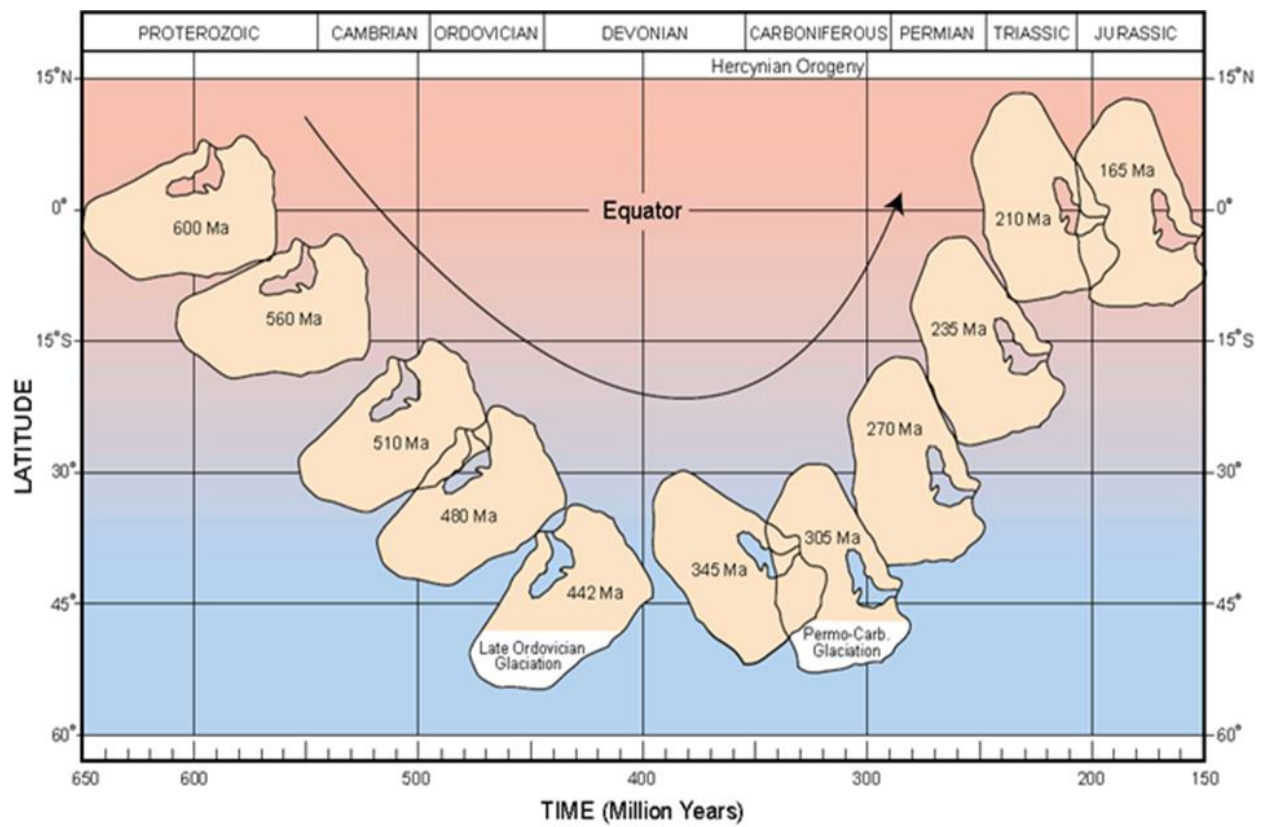


Figure 2.3 Paleolatitude positions of the Arabian Plate during the Paleozoic (Konert et al., 2001)

Series	Stage	Saudi Arabia			Oman (Angolini et al 2003)	Oman (Koehler et 2010)		Iran (Insalaco et al. 2006)			Revised SP2 Subsurface Sharland et al. (2001,2004)	Musandam Mountains, UAE (Maurer et al, 2009)		
		Member	Subsurface Equivalent	Subsurface Equivalent (Billings et al 2004)			Khuff 3rd order cycles	North	South	3rd - order (Reservoir)				
Early Triassic	Induan	Sudair	Sudair	Khuff A "Black anhydrite"	Sudair	Sudair		Aghar Shale	Sudair Shale		Ti30	Bah Formation		
		Khartam	Khuff A	Khuff B/C	Khuff	Upper Khuff	KS 1	Kangan		K 1			KS 1	
							KS 2			K 2			Ti20	KS 2
						Middle Khuff	KS 3	Upper Dalan		K 3			P40	KS 3
							KS 4			K 4			P30	KS 4
Late Permian	Changhsingian	Midhnab	Khuff B/C	Khuff B/C		Lower Khuff	KS 5	Nar Anhydrite	Middle Anhydrite		P20		KS 5	
		Duhaysan	Khuff C	Khuff C				Lower Dalan	Lower Khuff	K 5-7				
	Wuchiapingian	Huqqayl	Khuff D anhydrite											
			Khuff D											
Middle Permian	Capitanian	Ash Shiqqah	Ash Shiqqah	Khuff D anhydrite										
	Wordian-Roadian			Khuff D										
				Ash Shiqqah										

**Figure 2.4 Regional correlation of the chronostratigraphy of the lithostratigraphic units of the Khuff Formation in the outcrop compared to subsurface composition in Saudi Arabia, Oman, UAE and Iran. Note that the study interval (Khartam Member) is highlighted by yellow (Eltom et al., 2014b)**

## 2.3 Stratigraphy of Khuff Formation

The name of Khuff Formation was given after the 'Ayn Khuff (lat 24°55' N, long 44°43' E) close to Riyadh – Jeddah road (Powers et al., 1966). Khuff Formation was first defined by Steineke and Bramkamp, 1952, and then improved and formally described in its type section by Steineke et al., 1958. Powers et al., 1966, subdivided the Khuff Formation into three members, Unayzah, Midhnab and Khartam. Delfour et al., 1982, studied the type section in Al-Dawadimi quadrangle for the Khuff Formation and subdivided it informally into Unayzah, Huqayl, Duhaysan, Midhnab and Khartam Members. At the base, Khuff clastics have unconformable contact with the underlying massive Saq sandstone, of presumed Cambro-Ordovician age. The top boundary was placed at a sharp contact between Khuff carbonate and red and green gypsiferous Triassic Sudair Shale. Al-Aswad and Kamel, 1992, studied the microfossils in Khuff Formation and they found foraminifera, ostracods and calcareous algae that indicate Late Permian age for the Khuff Formation. Crasquin-Soleau et al., 2006, discovered ostracod fauna for the first time in the Khuff Formation in Saudi Arabia and improved the existence of the Permian – Triassic boundary that appears between the lower and upper units of Khartam Member.

The Permian – Triassic Khuff Formation comprises of a horizontally constant succession characterized by cyclic sedimentation of carbonates and evaporites precipitated in a shallow marine shelf environment. This indicates the existence of a flat carbonate ramp extending for more than 2500 Km in SE – NW strike direction and more than 1500 Km in SW – NE dip direction (Zeller et al., 2011). This resulted in a creation of layer-cake type platform comprising of metre – scale marker beds traceable for hundreds of

kilometres across the Arabian platform (Al-Jallal, 1995). The climatic conditions are interpreted as transitional from icehouse to greenhouse with sea-level fluctuations of moderate wavelength and amplitude. The climate is interpreted as arid similar to present day Arabian Gulf climate (Al-Jallal, 1995; Alway et al., 2002).

The paleogeographic setting and the distribution of environments and facies during the deposition of the Khuff Formation and its equivalents are illustrated in (Figure 2.5). In Saudi Arabia, the deposition of Khuff occurred over shallow continental shelf and made of transgressive carbonates (Janson et al., 2013). The Permian and Triassic successions of the Arabian Peninsula are extending north to south in a belt bordering the Arabian Shield. The formation is almost 180 m thick in the type section (Vaslet et al., 2005) and has been studied through outcrop sections and subdivided into five members which are Al-Shiqqa (formerly Unayzah Member of Khuff Formation), Huqayl, Dhahsan, Midhnab and Khartam Members (Manivit et al., 1986; Vaslet et al., 2005; Angilini et al., 2006), with basal khuff clastics within the first member (Figure 2.6). Each member was formed during different depositional cycles beginning with sub-tidal carbonates and shallowing upward into a regressive phase of mainly intertidal and sabkha sediments deposited on a carbonate – evaporate shelf (Al-Jallal, 1995 and Alsharhan and Nairn, 2003).



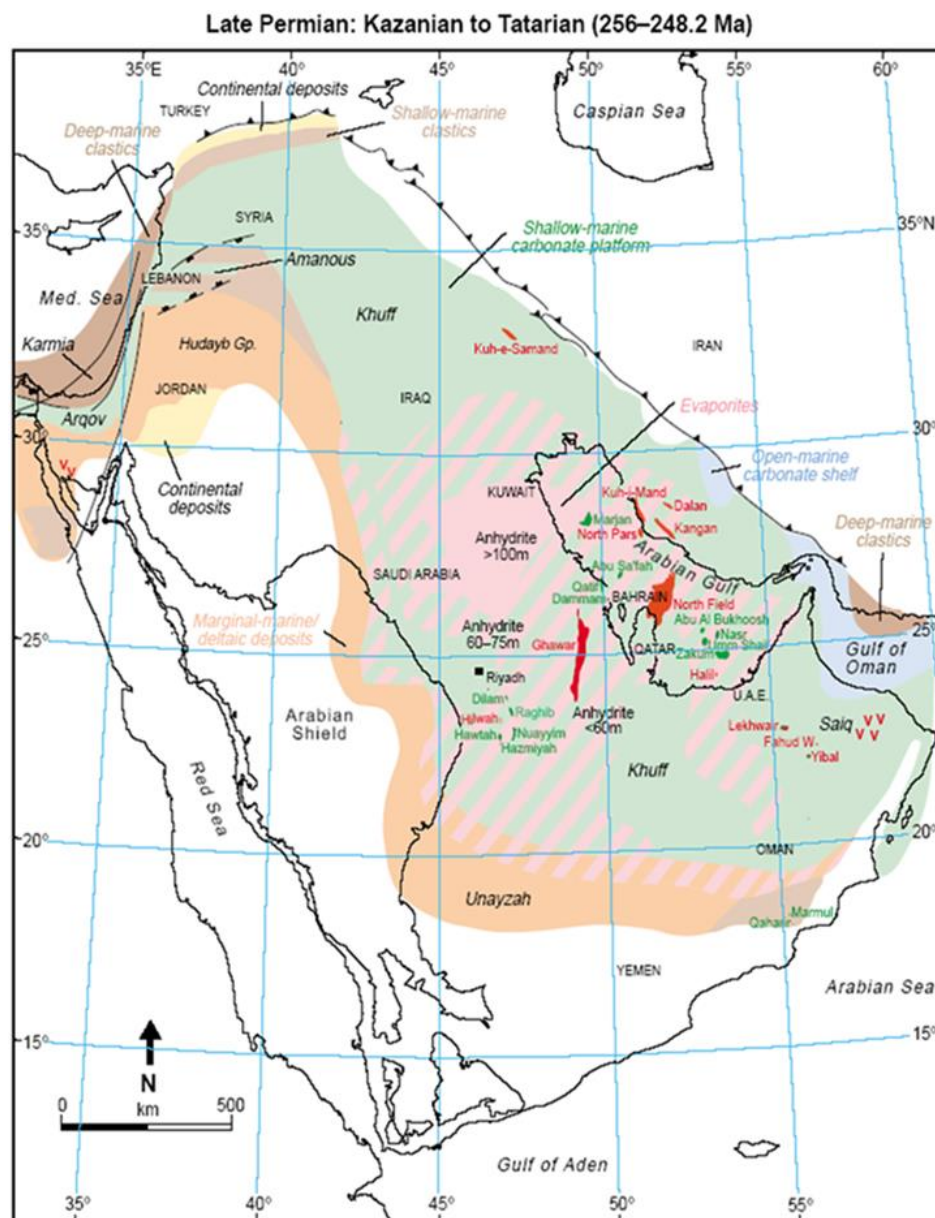


**Figure 2.5 Environments of deposition and major facies of the Khuff Formation and equivalents in the Arabian Plate (Ziegler, 2001)**



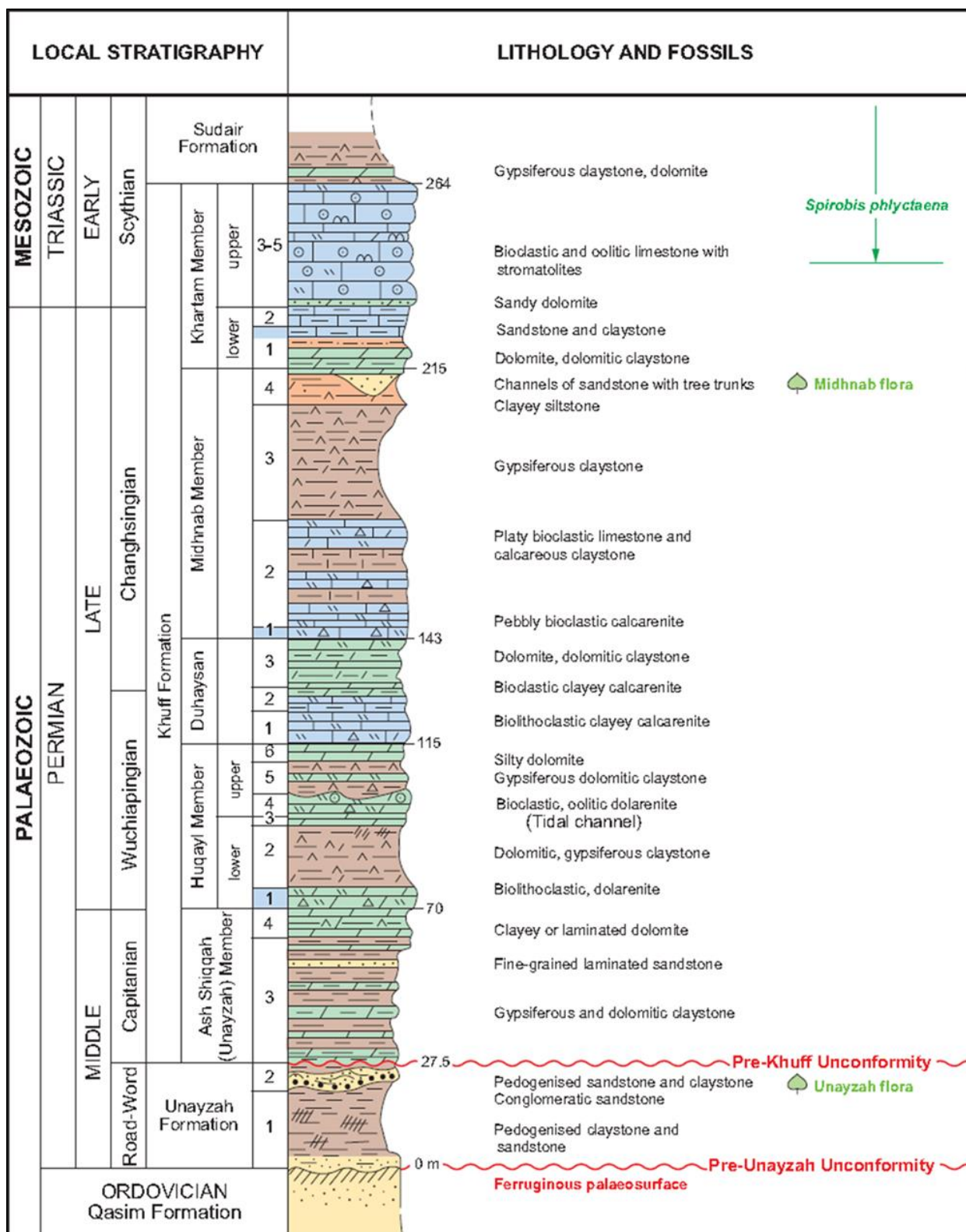


Figure 2.6 The composite section of Khuff Formation in Buraydah quadrangle (Vaslet et al., 2005)

The members of Khuff Formation are excellently cropping out in Buraydah quadrangle, Qasim area, and are well distributed and preserved. Angiolini et al., 2006 and Vaslet et al., 2005, studied the Khuff outcrops in different approaches and the following are brief descriptions for the basic information about each member in the type section:

**- Al-Shiqqa Member:**

The Al-Shiqqa Member is equivalent to the outdated Unayzah Member of Khuff Formation. It has the age of Middle Permian and deposited in environments ranging from transitional to continental and supratidal. The member consists of terrigenous sediments with sandy and silty dolomite, gypsiferous claystone and dolomite at the top (Vaslet et al., 2005).

**- Huqayl Member:**

The age of Huqayl Member is Late Permian. It resembles the marine transgressive event consisting of two sequential units. The lower unit started by bioclastic intraclastic dolomite, and then changed to gypsiferous clay and clayey dolomite. The upper unit consists of bioclastic dolomite arranged in tidal channels, gypsiferous clay and fine grained cherty dolomite, clayey dolomite with local chert nodules or dissolution breccias or pseudomorphs of gypsum and anhydrite.

- **Duhaysan Member:**

The Duhaysan Member is assigned to Late Permian in age. It is interpreted to be deposited in subtidal to littoral settings. The member consists of dolomitic calcarenite, gypsiferous dolomitic clay, and peloidal limestone with bioturbation (Vaslet et al., 2005).

- **Midhnab Member:**

Based on benthic foraminifers, conodonts and isotope analysis Midhnab Member is dated as a late Permian Changhsingian to Late Capitanian or early Wuchiapingian (Angiolini et al., 2006). This member shows a sequence oscillating from marine fossiliferous limestone at the base, to gypsiferous and dolomitic rocks at the top and deposited in restricted environment. In north central Arabia, the Midhnab Member changes at the top to continental sandstone channels and claystones in meandering stream system and swamps (Angiolini et al., 2006).

- **Khartam Member:**

Khartam Member is the uppermost mainly carbonate unit of the Khuff Formation. It is subdivided into two marine units characterized by littoral to tidal and intertidal paleoenvironments. The lower unit, dated as Late Permian, was deposited in supratidal to tidal environments and consists of coquina and peloidal limestone, bioclastic dolomite and dolomitic claystone. The upper unit dated as Early Triassic, was deposited in littoral to tidal and intertidal environments and consists of oolitic and peloidal limestone with

calcitized and stromatolitic construction, dolomitic coquina limestone and clayey dolomite and massive oolitic limestone (Vaslet et al., 2005).

The evolution of the transgression and regression periods through the precipitation of Khuff Formation and the depositional environments for each member are illustrated in Figure 2.7.

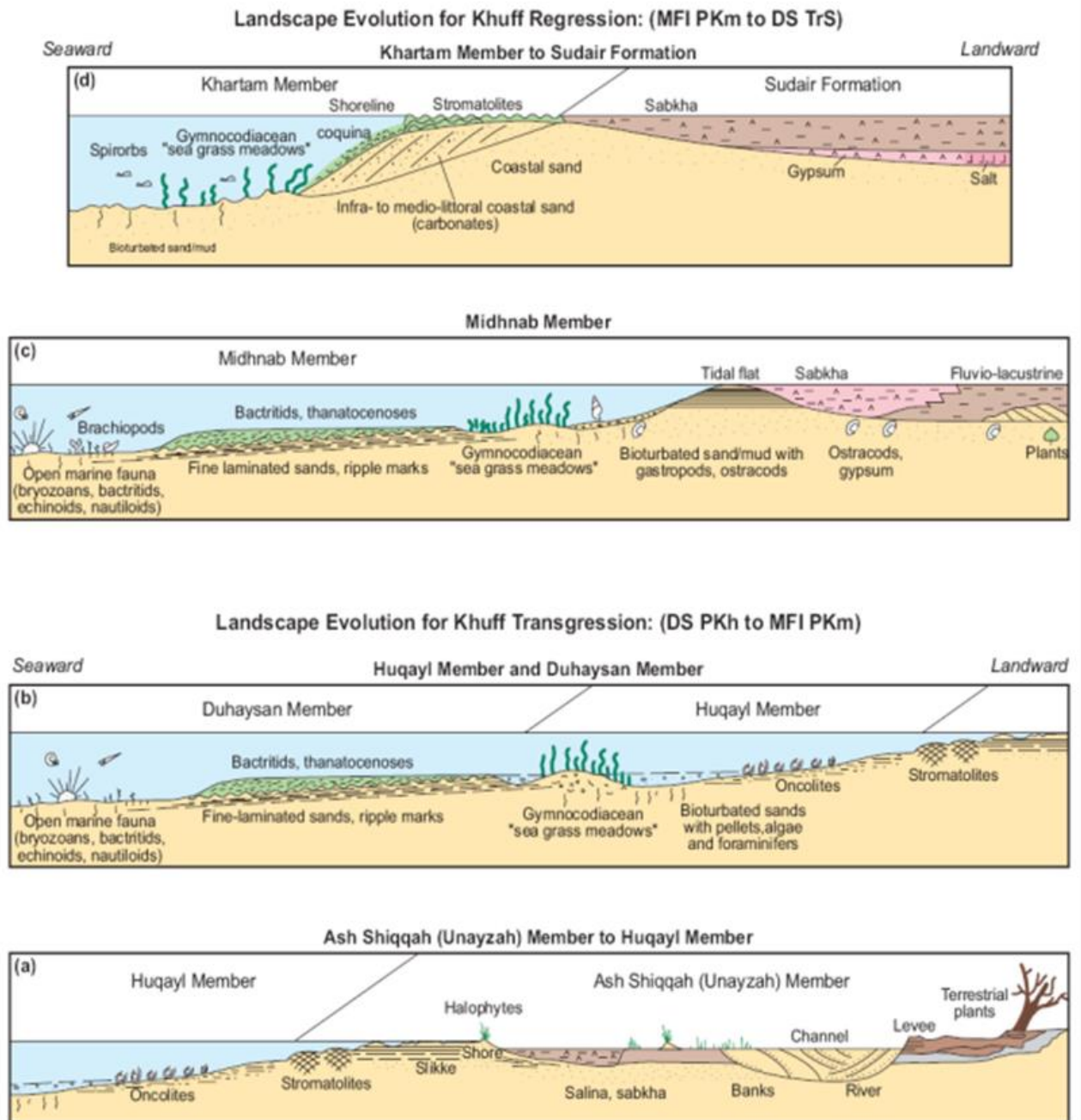


**Figure 2.7** The evolution of the Khuff transgression through the deposition of: (a) Al-Shiqqah and Huqayl members; (b) Huqayl and Duhasan members, and the evolution of the Khuff regression during the deposition of: (c) Midhnaab Member, and (d) Khartam member (Vaslet et al., 2005)

## **2.4 Permian – Triassic Khuff Reservoirs**

Khuff Formation and its reservoirs in the Middle East have different nomenclature in Iran, Bahrain, Qatar, Oman and Saudi Arabia. The Khuff in the subsurface in Saudi Arabia is divided into five members those are in ascending order Khuff E, Khuff D, Khuff C, Khuff B and Khuff A (Figure 2.8). Three producing reservoir intervals were discovered those are from bottom to top: Khuff-C, Khuff-B and Khuff-A. Khuff reservoirs in Central Arabia were deposited in shallow water environment with restricted marine fauna, but, the environment tends to be a more open marine fauna in the south-eastern part of Arabia in Al-Rub Al-Khali, UAE and Oman (Al-Jallal, 1995; Al-Dukhayyil, 2007; Koehrer et al., 2011). Because of its economic benefits and the commercial amount of the natural gas, Khuff Formation has been studied by several scientists and companies in the Middle East. In this study, digital outcrop modeling approach will be used, being the first time to be applied on Khuff Formation.

Khuff in the subsurface in Central Saudi Arabia is overlain by Sudair Shale and overlies Unayzah Formation. There is a markable unconformity between the siliciclastics which existed in the base of Khuff and the one at the top of Unayzah (Hughes, 2005). According to Hughes (2005) there is no direct relationship between Khuff Members in the outcrop and the one in subsurface. On the other hand, Al-Jallal in 1995 published a correlation between these members as following: Sudair Shale and Khartam Member are correlated to Khuff A, Midhnab Member is correlated to Khuff B, Duhayssan and Huqail Members are correlated to Khuff C, and Al-Shiqqah Member correlated to Khuff D and Khuff E in the subsurface.

STRATIGRAPHY			FORMATION	MEMBER	GENERALIZED LITHOLOGY	RESERVOIR
PERMIAN	TRIASSIC	LOWER	Sudair	Lower		
				Khuff A		Khuff A
	UPPER	Tatarian	Khuff	Khuff B		Khuff B
				Khuff C		Khuff C
				Khuff D		
				Khuff E		
		Kungurian		A		Unayzah A
	LOWER	Artinskian				
		Sakmarian				Unayzah B
CARBONIFEROUS	L	Tournasian-Asselian	Berwath	B		

Figure 2.8 Part of a generalized Paleozoic stratigraphic column for Saudi Arabia showing the stratigraphic position and the reservoir units of Unayzah and Khuff Formations (after Dasgupta et al., 2002)

The Upper Khartam Member is equivalent to Khuff-A and the upper parts of the Khuff-B reservoirs in eastern Saudi Arabia (Al-Dukhayil, 2007; Al-Dukhayil and Al-Tawil, 2007), and to the K1 and K2 Khuff reservoirs in Oman (Koehrer et al., 2010), Iran (Insalaco et al., 2006) and United Arab Emirates (Maurer et al., 2009) (Figure 2.4).

The reservoir properties of Khuff vary through the Arabian Plate and are primarily reliant on the stratigraphic position and the depositional and post-depositional controls on facies and their distribution through space and time. The Khuff rocks (dolomite, dolomitized – bioclastic limestone, and anhydrite) have high moldic, interparticle and intercrystalline porosities. The porosity of Khuff reservoir may exceed 30% and permeability may reach around 300 mD in the main gas reservoirs in the North and Dukhan Fields in Qatar (Alsharhan and Nairn, 2003). The reservoir units are of moderate to excellent reservoir quality (Koehrer et al., 2012; Lindsay et al., 2010).

In Saudi Arabia, Khuff Formation deposited in a cyclic pattern beginning with mainly subtidal carbonates and shallowed upward into a regressive phase of mainly intertidal and sabkha sediments deposited on a carbonate evaporite shelf (Al-Jallal, 1995; Alsharhan and Nairn, 2003). The reservoir units in Khuff Formation are present in Khuff-A, Khuff-B and Khuff-C. The reservoir quality in the Khuff is controlled by several factors such as; lateral continuity of facies, diagenesis, energy during deposition (deposition of grainstone under the high energy of the shelf break and open-marine condition such as in Oman and Iran resulted in higher porosity than the one deposited in restricted carbonate shelf like in Saudi Arabia and Kuwait). Another factor is the anhydrite percentage (increase in anhydrite content lead to decrease in the reservoir porosity and hence the quality and vice versa; see Al-Jallal, 1995).



The reservoir heterogeneity, generally, refers to the non-uniform phenomena and non-linear spatial distribution of a specific property within the same reservoir (Mohaghegh et al., 1994). In other words; the reservoir heterogeneity is defined as a variation in reservoir properties as a function of space. There are essentially two types of heterogeneity either vertical heterogeneity or areal heterogeneity. These properties may include permeability, porosity, thickness, saturation, faults and fractures, rock facies and rock characteristics.

Khuff-A is a naturally fractured gas carbonate reservoir and its quality varies according to the matrix porosity and permeability and also affected by the ratio of anhydrite to carbonate components. Also, the interpretation of the subsurface data revealed that there is vertical and areal pressure compartmentalization which in turn indicates some heterogeneity (Al-Anazi et al., 2010; Janson et al., 2013; Osman et al., 2014b).

For higher resolution and estimation of heterogeneity for the purpose of field development and reserves estimate, detailed reservoir characterization and modelling is required. Several methods might be used for determining and assessing the lateral variation in the petrophysical properties such as; basic statistical parameters (mean and standard variation), the variance along the distance, correlation coefficient between the porosity and permeability values and experimental semivariograms (Pranter et al., 2006).

Several studies have been conducted on the Khuff Formation in both outcrop analogs and subsurface reservoirs. Table 2.1 summarizes the most important work established on Khuff either in Saudi Arabia or any of the Middle East countries.

**Table 2.1 Some of the published studies about Khuff Formation in the Middle East**

<b>Authors</b>	<b>Study</b>
Al-Jallal, (1995)	Studied Khuff in subsurface and established the depositional environments and stratigraphic framework in Saudi Arabia and gulf countries.
Dasgupta et al., (2001)	Khuff-C reservoir characterization for the inter well heterogeneity (cemented dolomite layer) to minimize the drilling risk.
Vaslet et al., (2005)	Studied Khuff outcrops in central SA, in terms of lithology, age, depositional sequences and environments.
Vachard et al., (2005)	Studied the foraminifers and algae, indicated Late-Permian.
Alsharhan, (2006)	Studied Khuff in subsurface in UAE, a second-order composite sequence, ten facies units and four distinct depositional settings
Al-Dukhayyil, (2007)	Studied the Triassic Khuff A and B reservoirs in subsurface, and provided a sequence stratigraphic scheme based on detailed core description.
Maurer et al., (2009)	Geological investigation about Bih Formation (UAE, Khuff analog), they described a secondary dolomitization on the outcrop.
Zeller et al., (2011)	Used a combination of traditional and digital geological data to describe the heterogeneity on the outcrop scale in Oman.
Koehrer et al., (2011)	Described the lateral continuity and geometry of potential reservoir bodies and used them to build 3D facies static model.
Koehrer et al., (2012)	Described the distribution and textural variation of grainstones as potential reservoir facies on outcrop scale, Oman.
Bendias et al., (2013)	Studied the lower Khuff (KS6) in outcrop in Oman sedimentologically and how the paleorelief affects the thickness and composition of the sequence. Potential reservoir units been revealed.
Haase et al., (2013)	Made a high resolution sedimentological study on the grainstone bodies within the Khuff KS4 in Oman. Described the heterogeneity within these units in terms of deposited grains, porosities and textures vertically and laterally.

## 2.5 Terrestrial Laser Scanning

A New type of geological modelling can be done by utilizing a novel technique called LiDAR (Light Detection And Ranging), which is ever more widely used by the geological community. If the geological fieldwork is combined with digital modeling, this combination will lead to high – accuracy facies characterization and 3D outcrop-based geological computer models (Bellian et al., 2005).

In LiDAR (Figure 2.9), a laser ray is pulsed to the outcrop and then, by knowing the distance, a 3D point can be derived. The distance to the object is then estimated by computing the delay between the release of the pulse and its return. Also, the topography can be established by doing the scanning across the whole outcrop surface (White, 2010). Then, a virtual version for the outcrop can be constructed, analysed and interpreted in the office. This technique helps the petroleum geologists in many aspects beside the rapidness in data collection, such as; acquisition of data from inaccessible points in the outcrop, the collected data assist to examine the heterogeneity from small scale to large scale, ability to see the outcrop from different angles of view even in 3D, increase the sample size and so to enhance the fidelity of statistical analysis, large geological exposures or outcrops can be rapidly scanned (time saving), and finally it can be utilized to optimize the time spent in the field and the logistics (Hodgetts, 2013). In spite of LiDAR's many benefits it still has some technical limitations, such as its cost, the large weight of the instrument of the LiDAR system and its short battery life. As the collection of data is in high resolution, data from large outcrops might necessitate large storage capacity (millions or billions of points) (Hodgetts, 2013). LiDAR can be conducted either

terrestrially (on ground) or airborne, here the focus is on the terrestrial laser scanning. The final product from the terrestrial laser scanning after applying the processing and the interpretation is a 3D computerized virtual representation of the outcrop, called Virtual Outcrop (VO) (McCaffrey et al., 2005) or Digital Outcrop Model (DOM) (Bellian et al., 2005).



**Figure 2.9 The LiDAR system instrument Optech with an attached digital camera in front of the Upper Khartam outcrop**

The first time the term LiDAR appeared in geoscience literature was in the 1960s (Schuster 1970) in relation to atmospheric aerosol studies. Recently, LiDAR has been used in many geological tasks, including for digital outcrop modeling in petroleum industry. One of the first real applications of this approach in petroleum industry was done by Bryant et al., 2000. They described how digital high quality LiDAR data from outcrops in Rio Puerco in New Mexico could be utilized to assist the analysis and modeling of the Carboniferous Bend Conglomerate of the Boonsville Gas Field in North Texas (Bryant et al., 2000). Since then, there have been several petroleum-related approaches:

Pringle et al., (2004) used LiDAR to construct 3D high-resolution digital models of outcrop analog for reservoir models and also in architectural analysis and modeling of carbonates channel levees complex.

Bellian et al., (2005) and Enge et al., (2007) introduced the LiDAR technique as a tool in stratigraphical modeling and summarized the workflow from acquisition to the interpretation. Also, they gave an overview of the wide field of applications where LiDAR can be involved.

Pringle et al., (2006) reviewed the different kinds of models that can be generated for the reservoir analogs from different approaches. They listed the advantages and limitations for every method and the proposed solutions as well as the future expectations.

Labourdette and Jones (2007) integrated the classical field measurements and observations with the digital data and aerial photographs. This combination results in a

high resolution model which helps in the delineation of the stratigraphical horizons and the extraction of the 3D morphological data.

Al-Farhan et al., (2008) used laser rangefinder (Laser Gun) and ArcGIS software and combined the results with a photorealistic model and images. This combination resulted in a good platform for the analysis and interpretation to achieve the mapping for the outcrops in the Slick Hills, Oklahoma.

Al-Farhan et al., (2009) examined the LiDAR technique as a tool for improving the collection, processing and interpretation of the geological and geophysical data. Also, how it can contribute to provide better and more accurate fluid flow reservoir model. Their study revealed that the LiDAR is a powerful tool to construct more accurate reservoir models that can enhance the confidence in the drilling targets.

Fabuel-Perez et al., (2009) discussed the quantitative and qualitative workflow for the outcrop characterization and introduced a new technique to measure the dimensions of the geobodies in the outcrop. Also, they proved that the using of DOMs in combination with classical field data leads to substantial enhancements in effectiveness, precision, and value in outcrop characterization.

Buckley et al., (2010) combined terrestrial laser scanning and digital aerial photogrammetry to create a digital elevation model of the Castle Creek outcrop, British Columbia, Canada. This combination was very useful in capturing both the large outcrop surfaces and the near-vertical cliff sections in the 3D view.

Fabuel-Perez et al., (2010) provided a detailed workflow from acquisition to the construction of the DOMs and their interpretation in different approaches. The study-site

was the fluvial-dominated continental Oukaimeden Sandstone Formation, High Atlas in Morocco. Also, this study revealed the benefits from the integration between high resolution sedimentology and DOMs.

Pringle et al., (2010) integrated LiDAR and Ground Penetration Radar (GPR) to produce high resolution 3D model for the submarine channel complex outcrops in Karoo Basin, South Africa. Additional to that, the field data were also included (vertical sections and measurements) which resulted in a precise description for the channels and their distribution and lithologies.

Adams et al., (2011) discussed the importance of digital outcrop modeling as a tool for detecting, demonstrating, and upscaling the reservoir units and the internal heterogeneities which are generally below the accuracy of seismic data, and as also not simply detected and correlated between wells.

Lapponi et al., (2011) integrated the usual fieldwork data with precise petrographic and pore typing description and data delivered from digital outcrop models. This integration was applied on the data derived from a dolomitized carbonate reservoir, Zagros Mountains, Iran. The results show that the geological models constructed after the integration are more realistic and reflect petrophysical properties and trends that would have been difficult to obtained from the subsurface.

Wilson et al., (2011) utilized LiDAR to extract and model the 3D natural fracture sets on the outcrop by two methods, manual and semiautomated.

Other applications include outcrop modeling of clinoform barriers within deltaic outcrop analog (Howell et al., 2008); in reservoir characterization and flow models of lateral



petrophysical heterogeneity within dolomite facies (Pranter et al., 2006) and also in digital characterization of reef within carbonates ramp system (Adams et al., 2005).

All the previous studies reflect the wide contribution of LiDAR in different geological approaches and applications. Also, the studies revealed that it can be one of the important tools that must be utilized in the field geology before digging the outcrops for details.

## **CHAPTER 3**

### **METHODOLOGY**

#### **3.1 Introduction**

This research started by determining the location of the study area and the best exposures of the Khuff outcrops. More precisely, determining the best outcrops of Khartam Member by the aid of Saudi Geological Survey Maps, satellite images and Google Earth. Then, a reconnaissance field trip was organized to the study area at Qasim region in Central Saudi Arabia to examine the accessibility of the outcrop and select potential locations for detailed analysis.

The main methodologies for this study can be divided into two parts, and their integration will lead to the final result. The first part is the field investigations, which include sedimentological and stratigraphical studies along with the digital collection of the data. The second part is the laboratory and office investigations; which include sedimentological and petrophysical studies and the processing and interpretation of the LiDAR data.

### **3.2 Sedimentological and Stratigraphical Analysis**

Sedimentological studies have been conducted in the field and the laboratory. In the field, a total of four vertical stratigraphic sections and three horizontal sections were logged, sampled and drawn in a high resolution scale. For each vertical section, the description was bed by bed, and each bed was described precisely. The description includes; texture (based on Dunham 1962 classification), thickness, upper and lower bedding plane, lithology, colour, sedimentary structures, macro fossils, biogenic structures, diagenetic features, lateral continuity and any other remarks. Then, a sample from every bed and for each facies was taken for further investigations in the lab. Also, a detailed drawing and photos in the field for the sections were collected to enhance the interpretation. Approximately 200 samples were collected from four vertical stratigraphic sections and three lateral stratigraphic sections.

### **3.3 Spectrum Gamma Ray Analysis**

Spectrum Gamma Ray (SGR) is the measurement of the natural emissions from the radioactive elements within the sediments. In the field, there is a tool capable to measure the radioactivity of three elements (Figure 3.1) those are; K, U and Th. The tool is called Gamma Surveyor II (Gamma Surveyor model manufactured by Geofyzika, Czech Republic) equipped with a 3 x 3 inch NaI (TI) scintillation detector, it is small, handy and easy to carry and use. This tool takes the readings as counts per second for the concentrations of emitted uranium (U), thorium (Th) and potassium (K) and their total

counts (TC) within a discrete time window. A calibration experiment was conducted on the instrument by measuring the radioactivity on one bed on the outcrop in different time windows to decide about the perfect time window that would give most accurate result. After 30 readings with different times, 60 seconds (1 minute) has been chosen to be utilized in this study. There are three logs for the mentioned elements and another fourth log for the total counts for each vertical stratigraphic section in the outcrop.

The output of the spectrometer is elemental concentrations of radioactive elements K (%), Th (ppm) and U (ppm). Gamma-ray logs in API were calculated both for spectrometer and whole rock concentrations using the following formula (Maurer et al. 2009):

$$\text{API value} = K \times 13.078 + U \times 5.675 + \text{Th} \times 2.494$$

### **3.4 Laboratory and Petrophysical Analysis**

In the laboratory, the whole samples from all sections were slabbed and sedimentologically described again and also, thin sections for all samples were prepared for further microfacies analysis. The results from these slabs and thin sections description were compared with the field description and produced one accurate log for each section. Alizarin Red stain was added to some of the thin sections to differentiate between different carbonate minerals.

For all the samples collected from the outcrop, core plugs were prepared in the laboratory. All core plugs were examined in the saturation apparatus assembly and

benchtop liquid and TKA-209 gas permeameter systems to measure their porosity ( $\Phi$ ) and permeability (k) values respectively. Porosity and permeability measurements are important to characterize the geobodies or reservoir units which are relatively highly porous and permeable. In addition to the porosity and permeability measurements that have been carried out on the samples from the lateral stratigraphic sections, detailed analysis techniques were conducted on selected samples. These techniques include Scanning Electron Microscopy (SEM) and X-Ray Diffraction (XRD).

The integration between the microfacies analysis from the thin sections and the petrophysical analysis for the samples collected laterally; resulted in an interpretation for the heterogeneity within the potential reservoir units.



**Figure 3.1 Portable Spectral Gamma Ray SGRGamma GF Surveyor II logging tool**

### **3.5 Digital Outcrop Modeling (DOM)**

This part is the heart of this work because it represents the final product or result for the whole analysis after its integration with the previous investigations. The digital modeling applied here was achieved by using terrestrial laser scanning. Followings are the principals for this tool and how it can be used from acquisition to the interpretation.

The laser scanning or LiDAR approach has three stages starting by the collection of the digital data, then processing it and at last making interpretation and the final virtual model (Figure 3.2).

#### **3.5.1 Digital Data Collection**

In this part I used the terrestrial laser scanner to collect the data. The instrument is tripod mounted on the ground in front of the outcrop and the scanning arranged to target the area of interest in the outcrop and from different angles to avoid the gaps in the data. The preparation and setting of the instrument took most of the time, because in the selection of the perfect position several factors should be taken into account (Al-Farhan, 2010). To decide the resolution of the scanning, care should be taken for several factors such as; the purpose of the data collection, beam divergence (how the scanner laser beam widens with distance and the range of noise) and the accuracy of the scanner itself. Each scan position in the area of the outcrop has its own coordinate system and the data points are stored as 3D azimuth (horizontal), inclination (vertical) and range (Hodgetts, 2013).

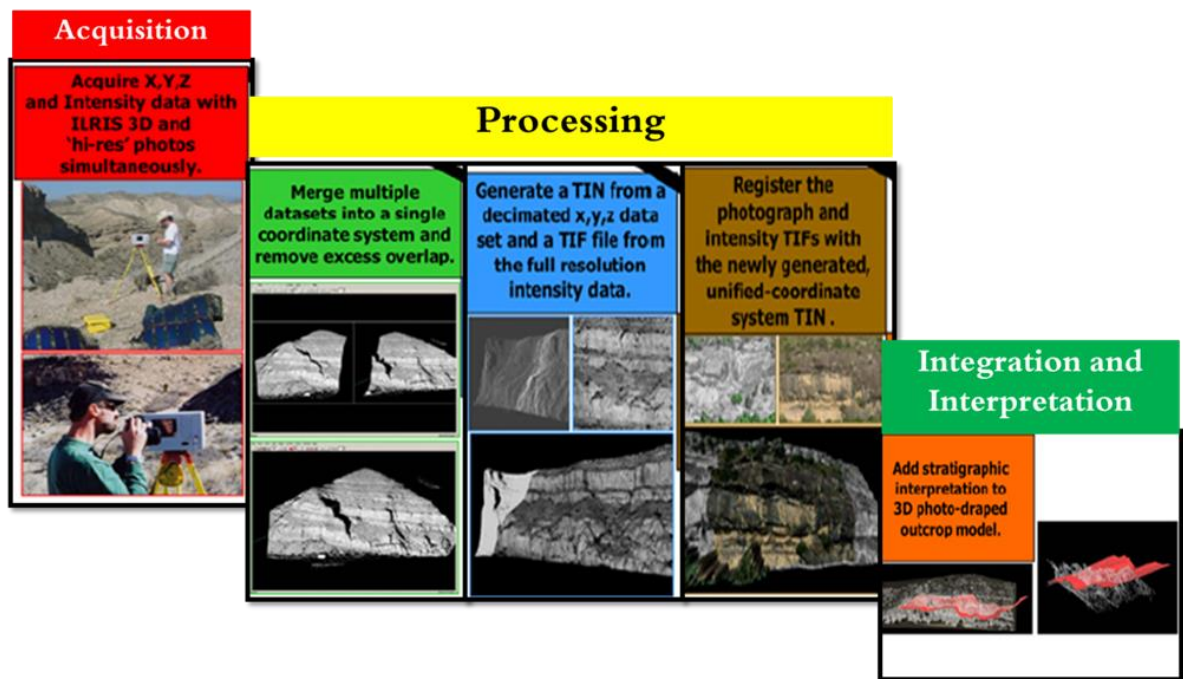


Figure 3.2 LiDAR workflow from the collection of the data to the interpretation for the final model (modified from Bellian et al., 2002)



The instrument used in this study was RIEGL VZ-4000 (Figure 3.3), this scanner is characterized by several features such as; it has very long range up to 4000 meters, 360° of rotation that cover wide area, very high speed data acquisition, very high accuracy and precision for the collected data, GPS and digital camera could be attached with it and capable to store the data internally. Also, it operates even in poor visibility and demanding multi target situations caused by dust, haze, rain, snow, etc. with high resolution and precision ranging based on the purpose of the scan.



**Figure 3.3 Tripod Riegl VZ-4000 laser scanner mounted on the ground in front of the Upper Khartam outcrop**

### 3.5.2 Processing of the Digital Data

When the scanning is finished, the obtained digital data is called point cloud and it is composed of millions of points. This point cloud needs some processing steps to make it ready for the interpretation and the construction of the virtual model. The processing steps in general aim to enhance the visualization of the digital model and to help its geologic interpretation (Enge et al., 2007). Usually, the processing starts with decreasing the number of points around the area of interest by removing the noise points such as; dust, trees, street, moving vehicles and anything which is not desirable. Then, register all the positions to each other in the scanner software in this case RiScan has been used. After that, the rest of the processing was carried out by using special software called Polyworks. The most important processes that have been done on the data are:

#### ***A- Merging:***

Usually, the scan for a single outcrop should be taken from different positions to cover the whole area of interest. Here, the outcrop was scanned from different four positions. All these individual scans have been merged into one coordinate system (Fabuel-Perez et al., 2009). The merging can be done by two methods, either by reflectors or directly by software.

The first method, reflectors should be put on the outcrop before the scanning starts and care should be taken on the positions of the reflectors, so as to make sure there will be an overlapping between the scans by at least four reflectors. In this study this method has

been used (Figure 3.4) and the reflectors used are called prismatic reflectors mounted in tripod.

The second method is to do the merging process by using software, by decreasing the error between the matched shapes on the overlapping point clouds. Relatively, this method saves time in the field because it does not need any reflectors but it is better just in the large outcrops and care must be taken regarding to the overlapping between the scans (Hodgetts, 2013).

#### ***B- Georeferencing:***

This step serves to define the position or the location of the area of interest by determining its location in terms of global coordinate system such as; UTM (Universal Transverse Mercator) or latitude/longitude coordinate system. UTM is the most common to be used because it is well known and easy to understand (Hodgetts, 2013). This step can be achieved by a variety of methods including:

- Global Navigation Satellite Systems (GNSS) surveying for the reflectors' positions that have been used in the merging process. In this case the readings will give the accurate position for the outcrop. This can be done by the well-known GNSS.
- GNSS surveying for every reflector position and then re-orienting the merged scan positions to match the GNSS positions.

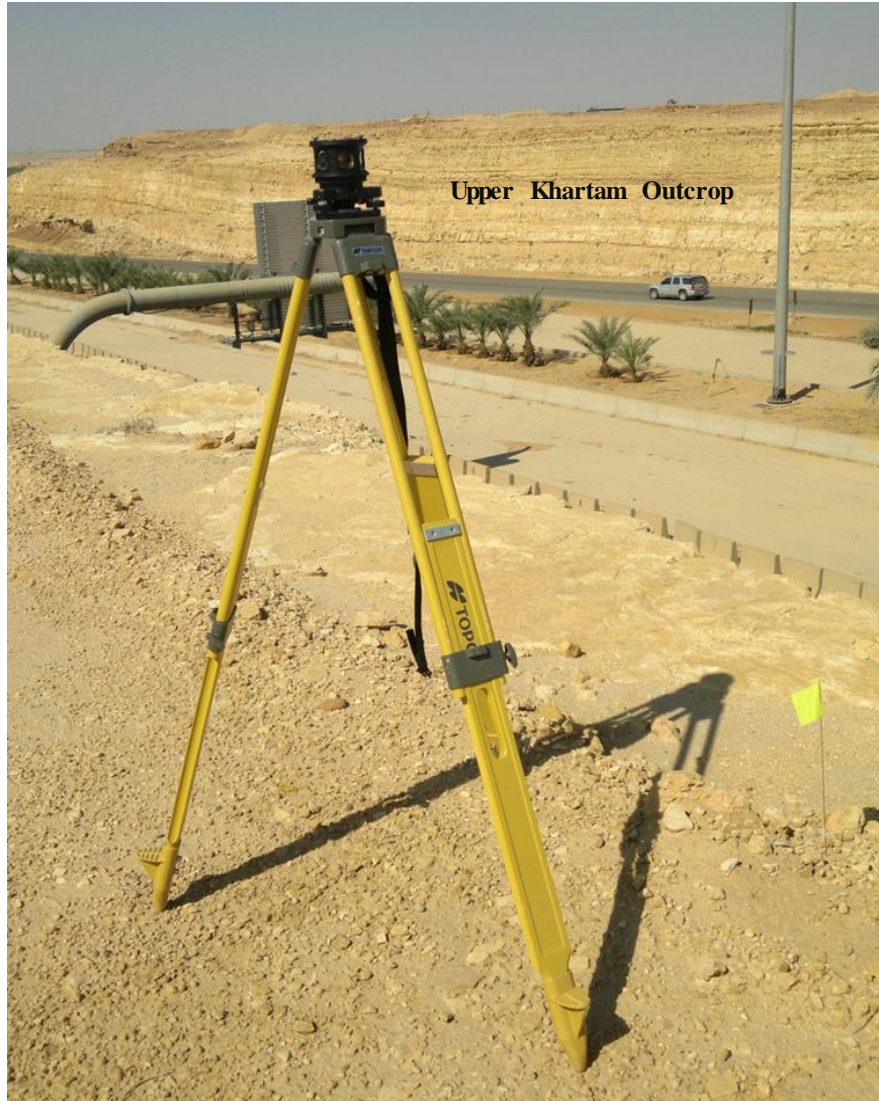


**Figure 3.4 Tripod prism reflectormounted in front of Upper Khartam outcrop**

### ***C- Visualizing the digital data:***

There are a variety of methods to visualize the LiDAR data or the digital data including point clouds, triangulated meshes and photorealistic models (Hodgetts, 2013). The following gives a brief account for each of them.

#### **I- Point clouds:**

In this visualization the data are presented in their basic form and each point has x, y and z position with one or more attributes such as; colour, intensity .... etc. The advantages of this type of data presentation are that it is the fastest type to be visualized; it needs the least amount of processing relative to other types, and allows a large amount of data to be visualized rapidly. The limitations for this type are that the interpretation is very difficult and when the data set is large it is very hard to deal with.

#### **II- Triangulated meshes:**

This method is defined by the linking of the points together by a series of triangles in the point clouds and this will produce the triangulated irregular network. When the mesh is created, we can utilize the orientation of the triangles to do the relief shading as well as detecting some of the basic attributes and surfaces. In structural geology, this is beneficial because when the orientation of the triangles indicates a common direction this will be interpreted as; bedding planes, faults or fractures.

Triangulation increases the number of data to be visualized and this will cause a problem in the processing and interpretation. To avoid this problem, point clouds and meshes decimation (decrease in the triangles) might be applied. The decimation will affect the accuracy of the data negatively, but it would produce solid surfaces which are easier to interpret than the raw data. The limitations for the triangulation method are that complex data with multiple scan positions are difficult to be triangulated, it is a very slow process and less accurate.

### **III- Photorealistic models:**

In this type of visualization digital photographs will be attached to the triangulated mesh to increase the accuracy of the model. The idea here is to fill the gaps that might be found between the point clouds by producing solid surfaces in false colors. Photographs can give meaning of these false colors by draping the actual photos on the solid surface accurately on position. This integration will increase the resolution of the model and hence leads to a better understanding and easier interpretation.

When the model is ready, many attributes can be generated such as; intensity, RGB (Red, Green and Blue) color channels, and the surface attributes (such as; curvature, roughness, and co-planarity) and others.

#### ***D- Integration with other data:***

When the processing steps are completed and the scans have been merged, georeferenced and clearly visualized, the environment now is suitable to visualize and integrate other types of data on the model. In this study a wide range of data has been integrated with the digital model and then, a final integrated and enhanced model was constructed. These data includes; sedimentological, stratigraphical and petrophysical results from the field and laboratory.

### **3.5.3 Interpretation of the Digital Model**

Once the final integrated digital model is constructed, all this huge amount of data and large area of the outcrop need to be interpreted. The final interpretation of the model is generally done manually, keeping in mind geological points of view. Very recent advancements are trying to make even the interpretation automatic (Hodgetts, 2013).

There are software tools which help a lot in the interpretation of the digital data such as; Polyworks, Virtual Reality Geological Studio (VRGS) and ArcGIS. Here, we used Polyworks for the initial states of processing until the construction of the polygonal model, and VRGS and ArcGIS for the geological analysis and interpretation.

All the sedimentological and stratigraphical data have been superimposed and integrated with the digital model. This combination has led to construct different models such as; facies model, stratigraphic model and heterogeneity model.



## **CHAPTER 4**

### **SEDIMENTOLOGY AND STRATIGRAPHY**

#### **4.1 Introduction**

Sedimentology and stratigraphy are a major part of this work because it will reveal the depositional environments and the vertical stacking pattern of the Upper Khartam Member. This part was based on field observations and laboratory analysis for more accurate result. Also, this part is considered to be the heart of the reservoir characterization and modelling.

In the study area along the road-cut, the strata of the Upper Khartam Member are dipping towards the east. The outcrop in this location is bounded at the bottom by the Permian\Triassic boundary and at the top by the Sudair Formation. The vertical sections covered part of the outcrop and not the whole Upper Khartam and the results were compared and integrated with previous studies. Each bed encountered in the four stratigraphic sections investigated has been sampled. About 120 samples were collected for further laboratory investigations. Thin sections were prepared from the collected samples and analyzed using optical microscopy for microfacies and biocomponents and the results were correlated with field observations.

The outcrops of Khuff Formation in the Middle East attracted many researchers to investigate it in different approaches. So, the previous studies by; Vaslet et al. (2005),

Insalaco et al. (2006), Koehrer et al. (2010, 2011, 2012), Janson et al. (2013)Osman et al., (2014a) and Eltom et al., (2014b) were utilized as a guide to infer lithofacies and stratigraphic succession. The vertical hierarchy of the Upper Khartam Member were analyzed and interpreted within a sequence stratigraphic framework. This stratigraphic framework included the characterization of beds and bed sets which are stacked into cycles to form cycle sets (High Frequency Sequence, HFS) that are arranged to form the Upper Khartam composite sequence. The depositional model was constructed also and the HFSs have been illustrated in it.

## **4.2 The Permian\Triassic Boundary Interval**

The delineation of this interval in this study was based in the previous work by Vaslet et al., 2005 and the analysis and interpretation of the field and lab data led to identify this zone (Figure 4.1A). There are some evidences which support this interval to be the Permian\Triassic boundary between the Lower and Upper Khartam Member. These evidences include:

- The dark-red colored claystone interval overlies the yellow dolomitic mudstone of the Lower Khartam Member.
- Samples from the Lower Khartam Member contain very few brachiopods bivalves, gastropods and ostracods.
- The lower interval of the Upper Khartam Member (about 20 m) is barren of microfossils including foraminifera with very few scattered serpulids, but it is

dominated by microbiolites, which are present in the forms of thrombolites and stromatolites.

- SGR logs in the studied outcrop show a major decrease in uranium, thorium and potassium contents throughout the Upper Khartam Member. In contrast, the Lower Khartam members exhibit higher concentrations of these elements (Figure 4.1B).

The precise location of the starting of uranium depletion is the first limestone bed of the Upper Khartam Member that overlies a highly cemented reddish fossiliferous oolitic grainstone of the Lower Khartam Member. The boundary between these two beds is an interval of reddish dark claystone and is suggested to be the Permian\Triassic boundary interval.

Calculated API values of GR from SGR logs were also compared to Upper Khuff Formation outcrop in UAE (Figure 4.2). The SGR logs of the study area shows similar pattern of uranium depletion and API decrease through the Lower Triassic Upper Khartam Member.

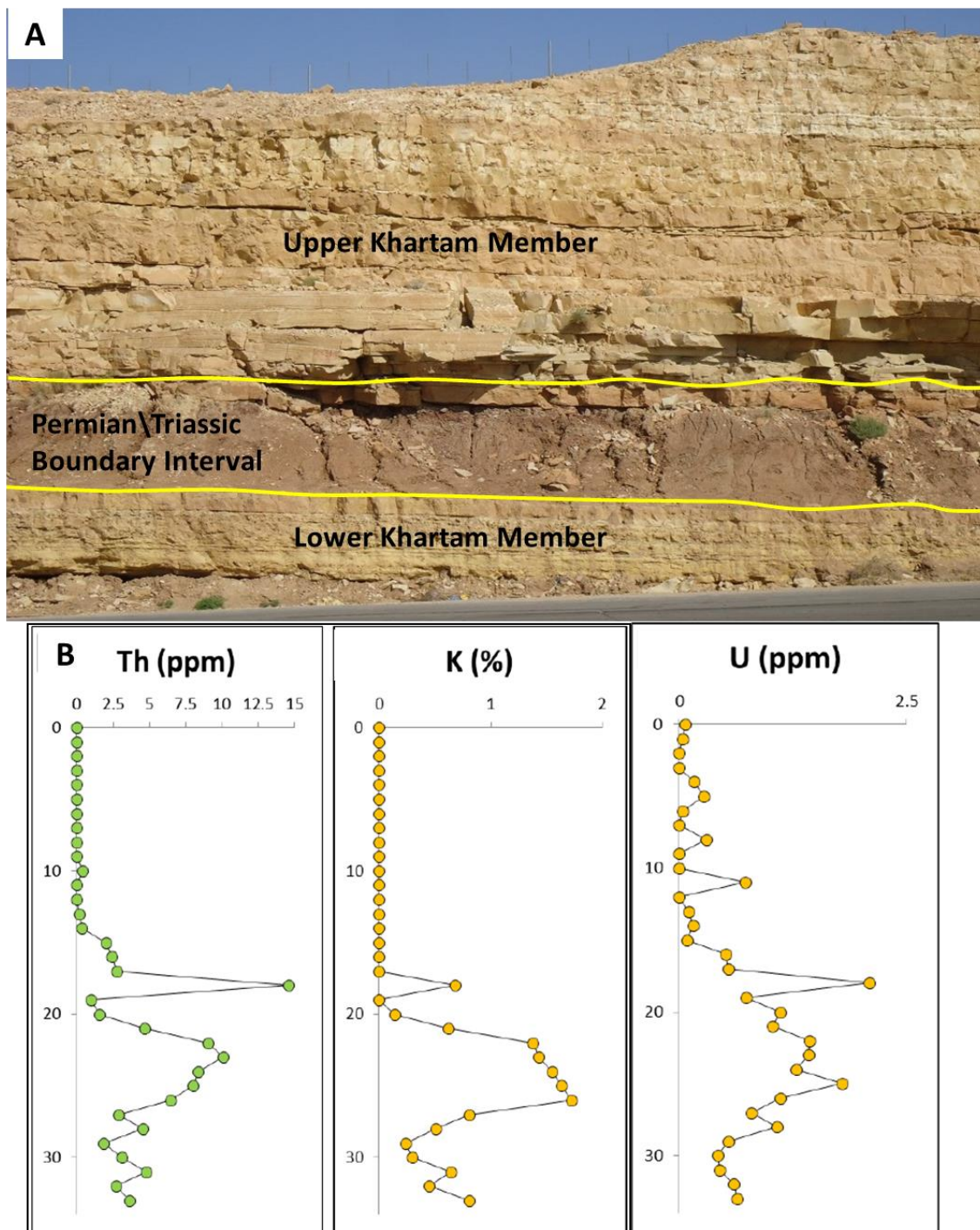


**Figure 4.1 A:** Outcrop photograph shows the carbonates of Upper Khartam and the yellow dolomitic mudstone of the Lower Khartam Member and the red claystone interval; **B:** spectral gamma-ray (SGR) logs for U, Th, K from the outcrop (after Eltom et al., 2014b)

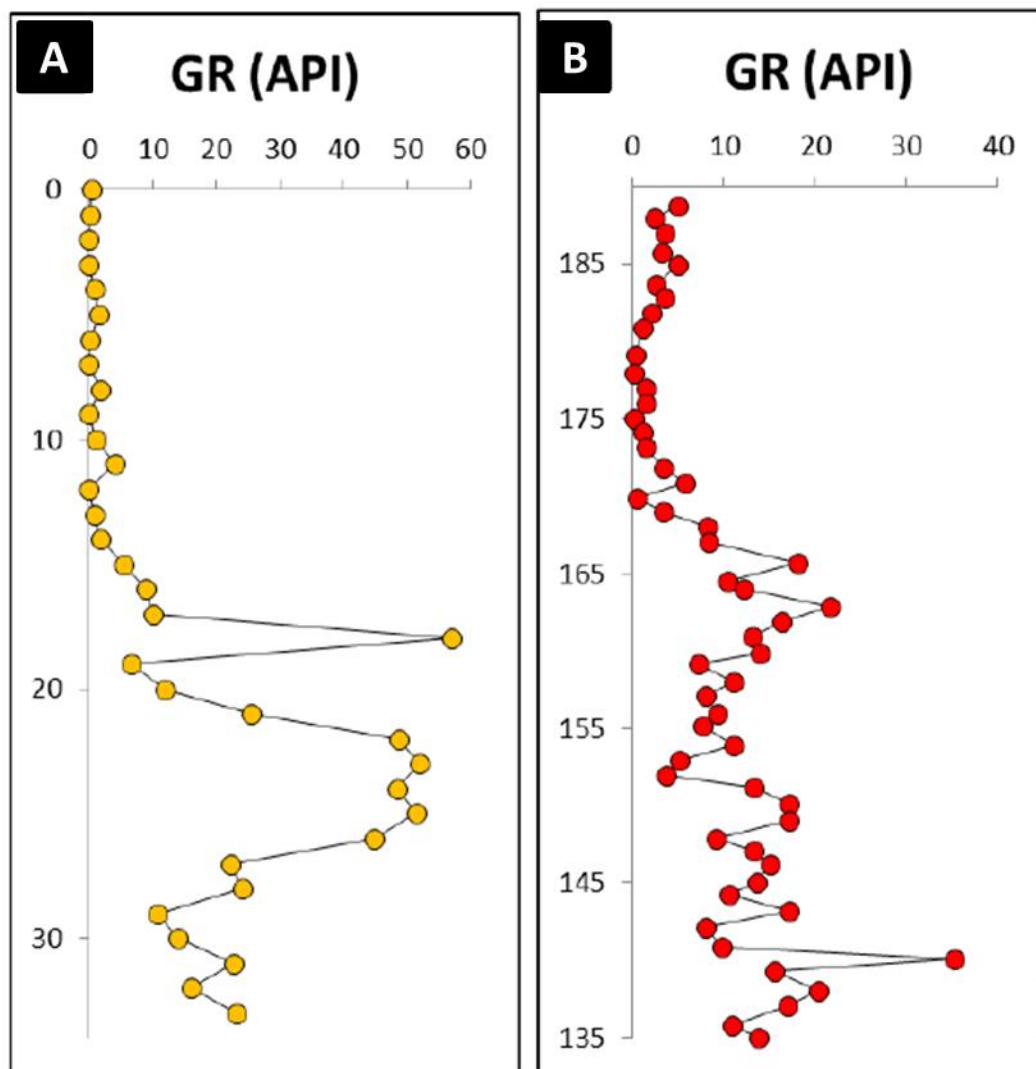


**Figure 4.2 A:** The total GR in API for SGR logs from the study area; **B:** digitized published GR in API logs of Upper Khuff equivalent outcrop in UAE (Maurer et al., 2009) (Eltom et al., 2014b)

### 4.3 Facies Analysis and Interpretation

The vertical stratigraphic sections are named KM-1 to KM-4 starting from the east to the west with a spacing of 100 m between them. Followings are brief description for them:

- **KM-1:** This section is 12 m thick and showing coarsening upward trend starting by mudstone to wackestone and then to grainstone. Also, there is a thickening in the coarser units. The section reflects the cyclicity which appears by the stacking of five vertical coarsening and thickening upward trend. The first cycle is 4.57 m thick and starts by massive mudstone and wackestone and ends with oolitic grainstone with the presence of wackestone lenses. The second cycle is 2 m thick and starts by fissile mudstone and ends with massive grainstone. The third, fourth and fifth cycles start by fissile mudstone and end with thick wackestone, the thickness of the wackestone beds increasing upward from 2, 2.5 to 3 m (Figure 4.3). The first cycle reflect the highest total API in the mudstone and wackestone in this cycle. The porosity and permeability data show that the grainstone units have high porosity reaching 33 % and permeability reaching 13 mD (Figure 4.4).
  
- **KM-2:** This section is about 9 m thick and its starting by thick and hard wackestone containing lenses of mudstone. Then thick bed of packstone starts to appear and it shows herring-bone cross bedding and gutter casts structures. A thick skeletal oolitic grainstone bed appears and overlies a wackestone bed and is overlain by the presence of microbial heads which have dolomitic base and

convex top. Intercalation between fine mud and grainstone starts to appear (Figure 4.5). The gamma ray API increases in the fine grain mudstone and sometime in the wackestone and decreases in the grainy units. The porosity-permeability cross plot revealed linear relationship between them (Figure 4.6). The grainy units have high porosity reaching to 34 % but the permeability is poor, it does not exceed 1 mD.

- **KM-3:** This section is 8.5 m thick and it reflects high cyclicity and interbedding between grainstone and wackestone. The section starts by thick grainstone and packstone about 2 m with gutter casts and boulders have the size from 50\*20 to 35\*15 cm. Then the section showed a cyclic deposition between grainstone and fine wackestone, the thickness of the grainstone increases upward while the thickness of the fine is decreases. The microbial heads are encountered here also and the dolomitized beds are also appearing. The section is topped by 1.5 m thick dolomitized oolitic grainstone bed. The total API for this section reflects the same cyclicity of the beds and produces highs and lows according to the texture variability (Figure 4.7). The porosity-permeability cross plot shows a linear relationship between them but with a lesser correlation coefficient than the one in KM-2 (Figure 4.8). The highest porosity value was 33 % while the highest permeability value was 0.8 mD.





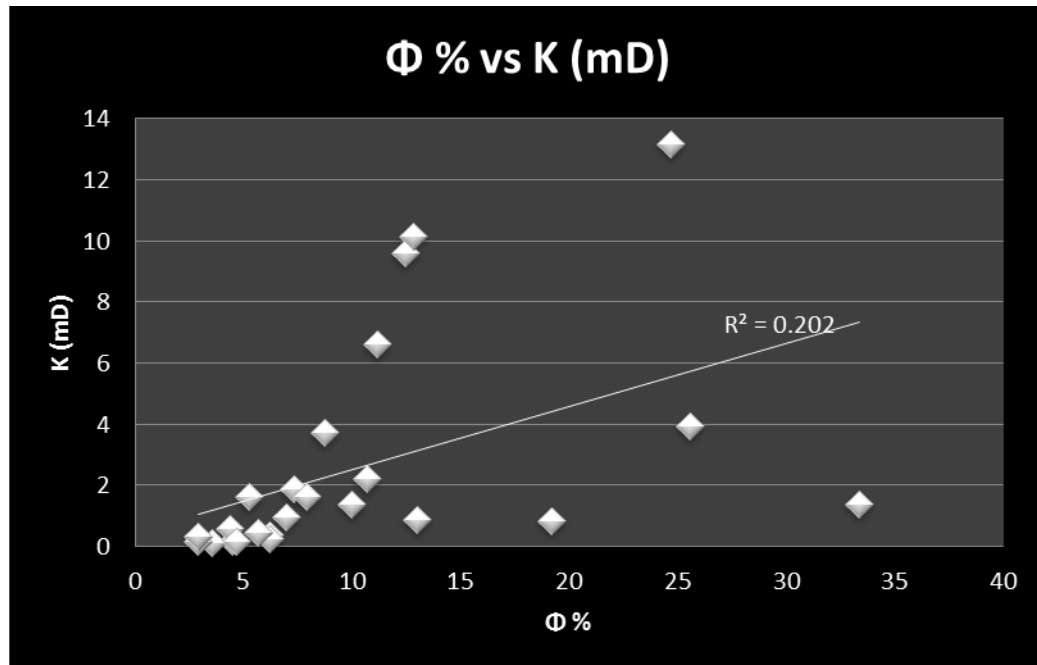


Figure 4.4 The porosity-permeability relationship within the strata in the vertical section KM-1

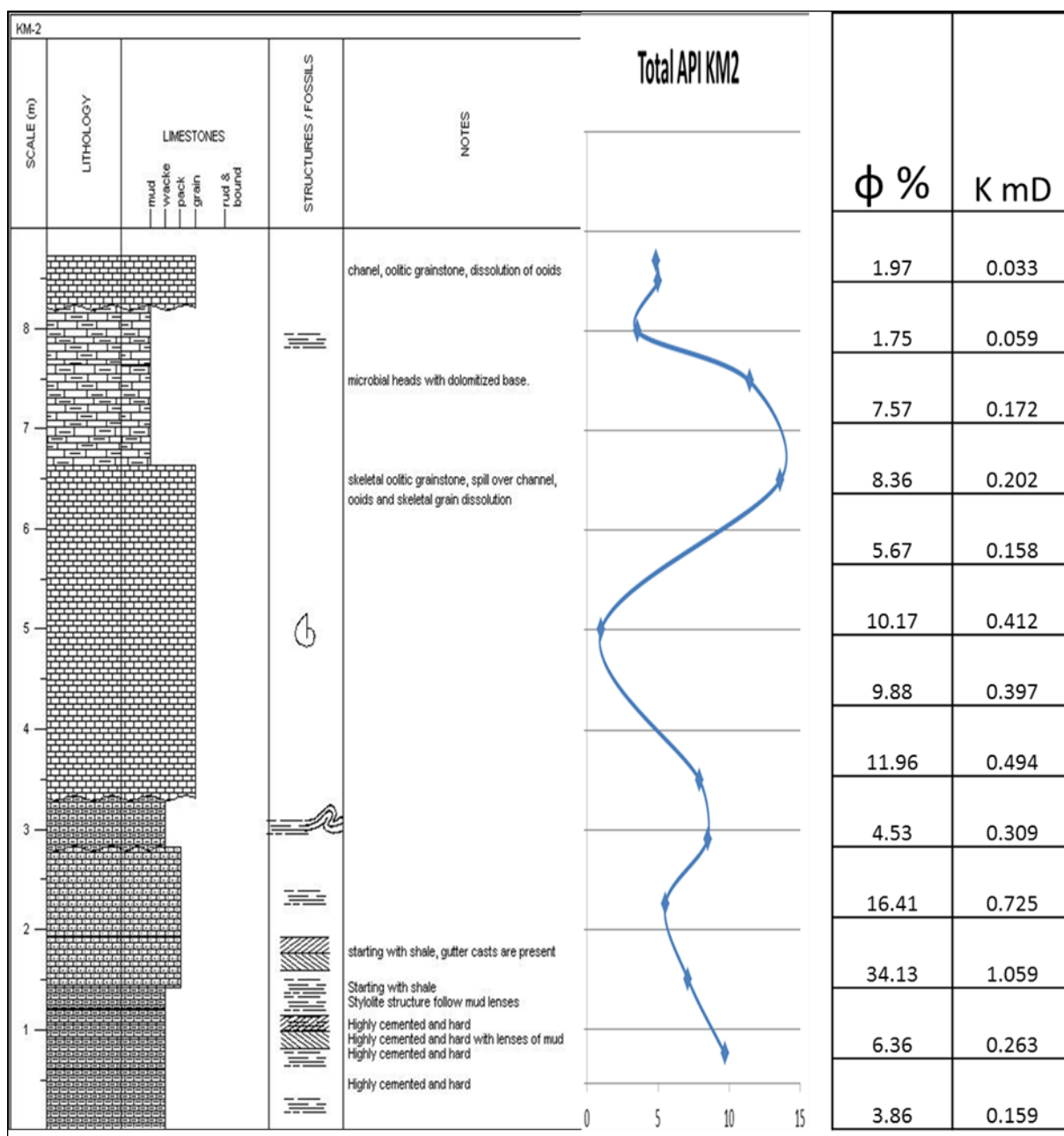


Figure 4.5 The field description of the vertical section KM-2 and the structures appearing on it along with the gamma ray data and porosity and permeability data

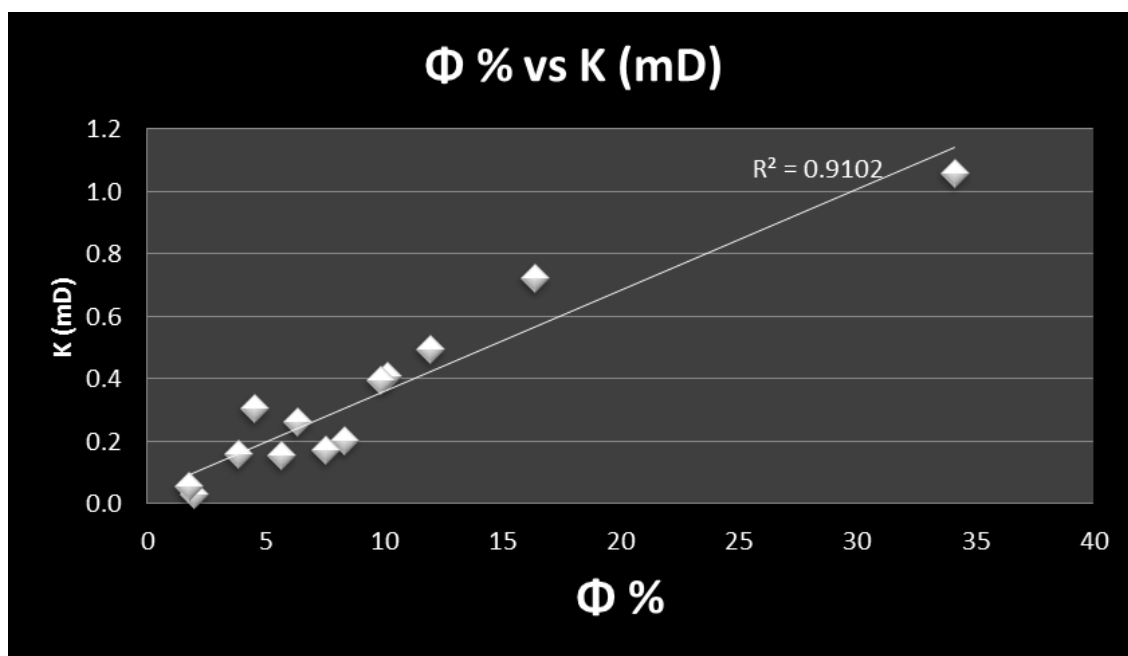


Figure 4.6 The porosity-permeability relationship within the strata in the vertical section KM-2

- **KM-4:** This section is about 5 m thick and it consists of two kind of cyclicity, the first one (2.5 m thick) is a continuation of the previous in KM-3 between grainstone and wackestone. The second one (2.5 m thick) is a cyclic deposition between grainstone and mudstone to the top of the section. The thickness of the grainy units increases upward in the first cycles and decreases in the second one. The thickness of the finer units decreases upward in the first cycles and increases in the second one (Figure 4.9). The grainstone units are highly cemented and dolomitic and contain mud lenses. The gamma ray pattern also shows some cyclicity which infers the cyclicity in the deposition. The porosity – permeability cross plot showed that the relationship between them is more or less linear but with correlation coefficient about 0.5 (Figure 4.10). In the dolomitized oolitic grainstone the highest porosity value was 32 % and the highest permeability value was 1.5 mD.

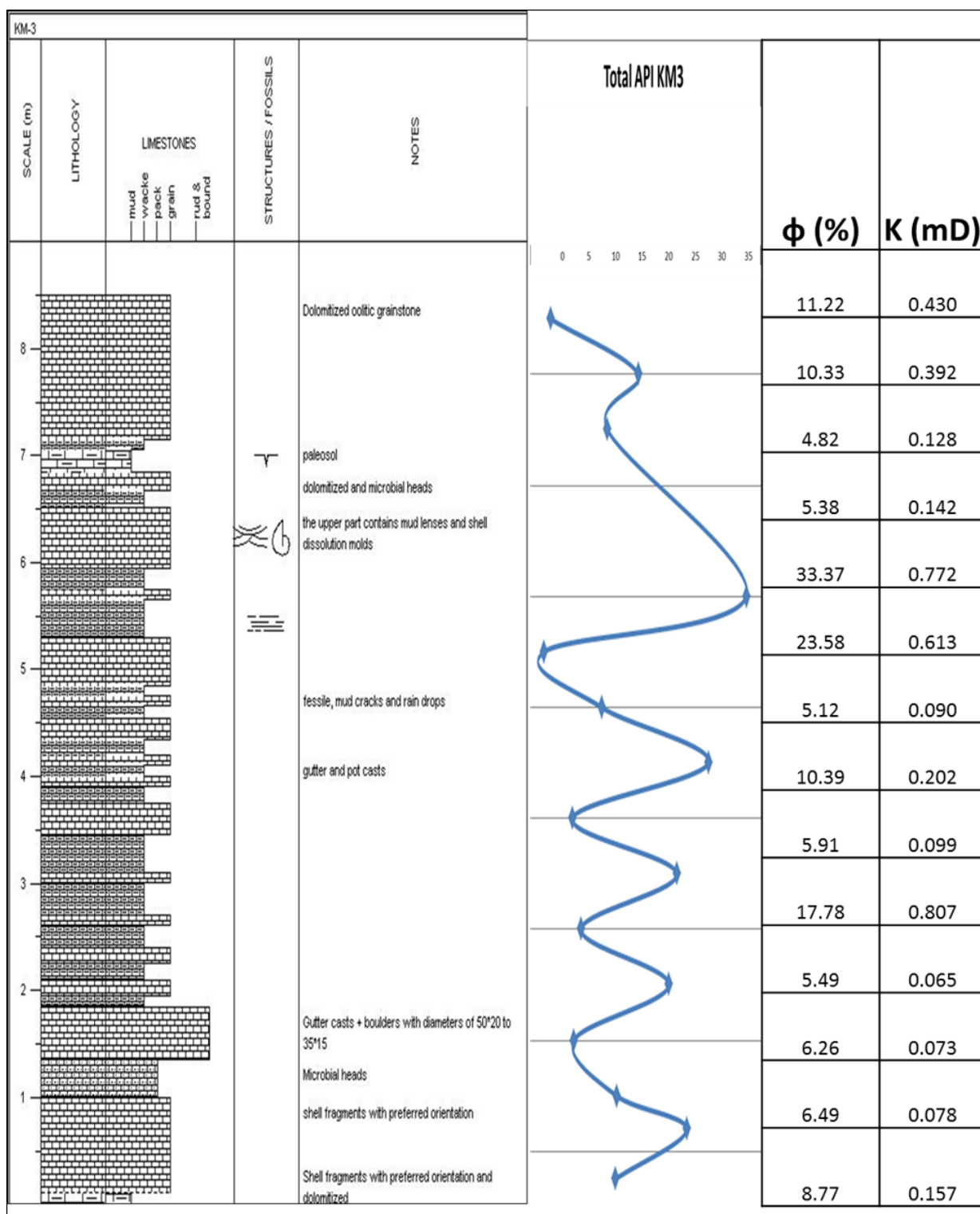


Figure 4.7 The field description of the vertical section KM-3 and the structures appearing on it along with the gamma ray data and porosity and permeability data

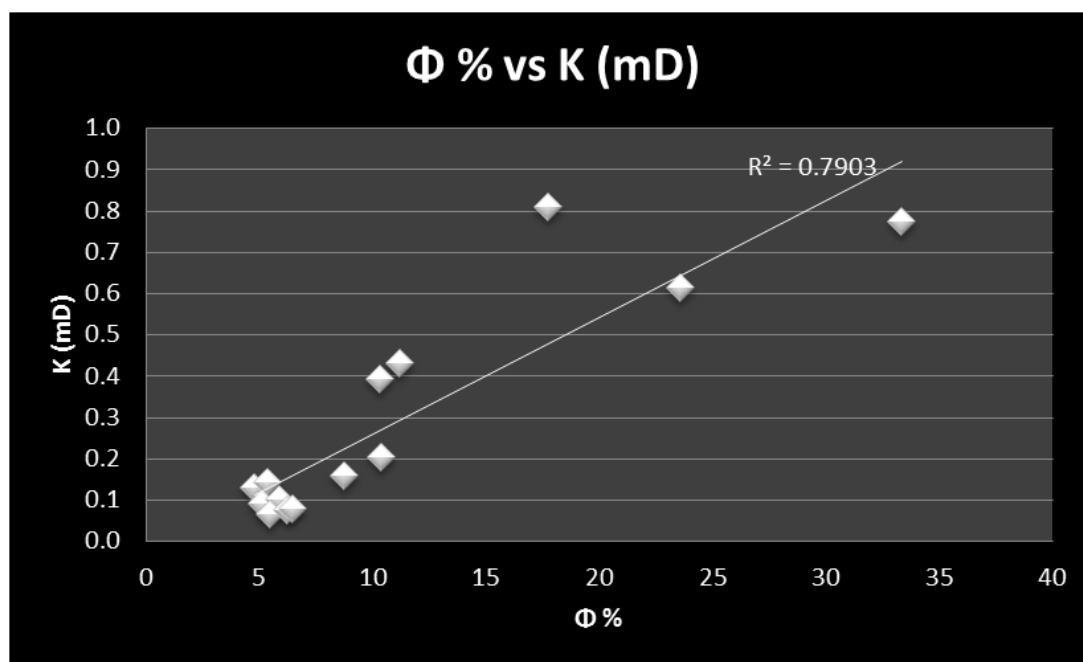


Figure 4.8 The porosity-permeability relationship within the strata in the vertical section KM-3

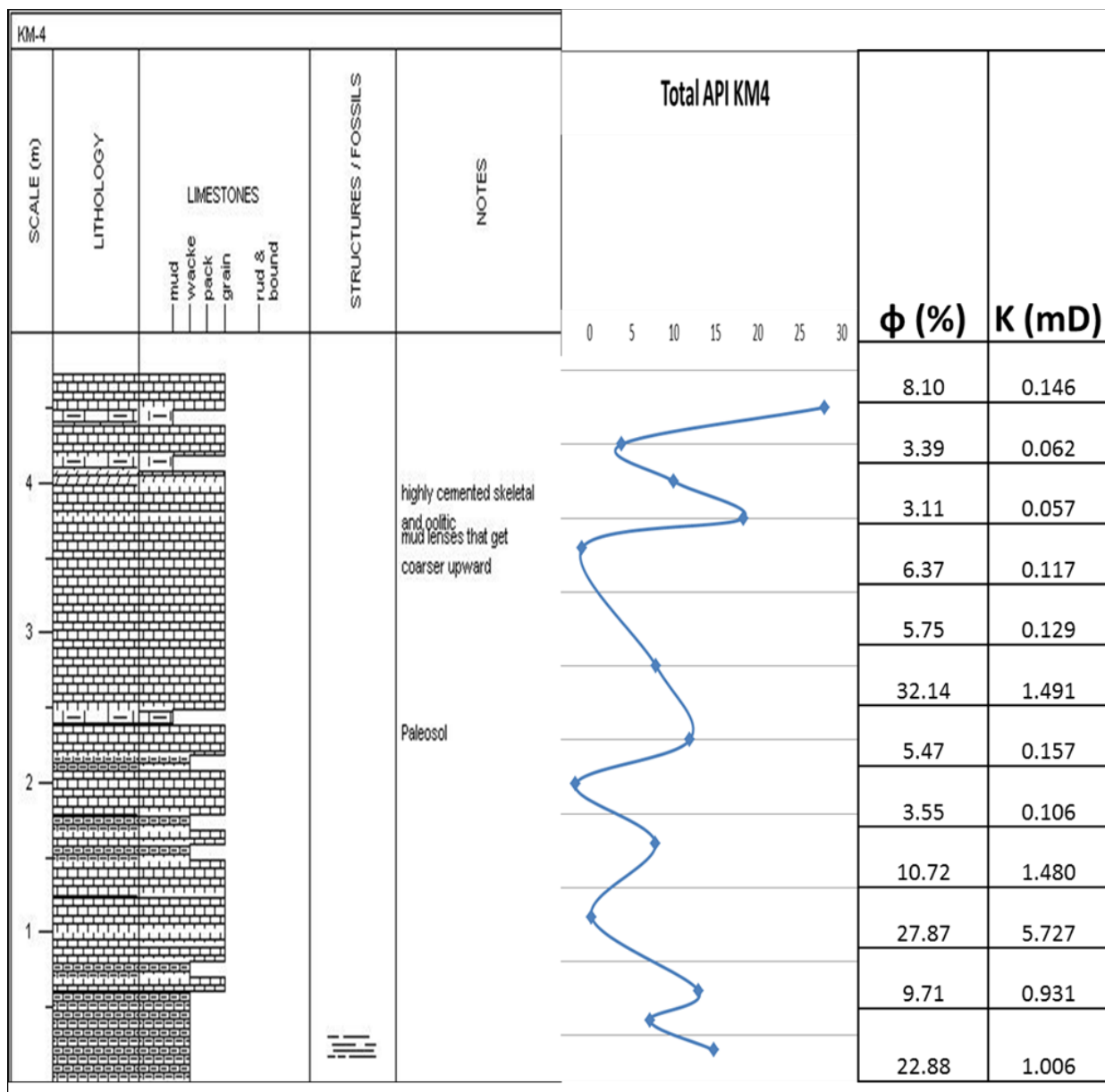
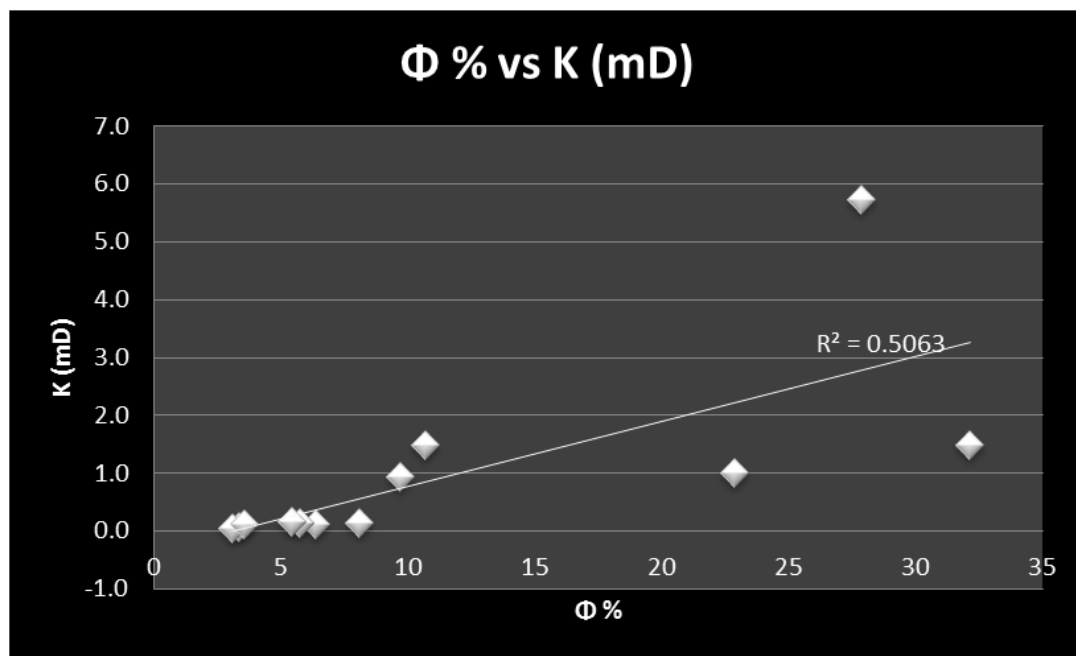


Figure 4.9 The field description of the vertical section KM-4 and the structures appearing on it along with the gamma ray data and porosity and permeability data



**Figure 4.10** The porosity-permeability relationship within the strata in the vertical section KM-4



The stratigraphic descriptions of the outcrop sections and the detailed analysis of thin sections revealed a total of 6 lithofacies. The four vertical sections studied revealed that these lithofacies are deposited within the depositional environments ranging from the offshore, foreshoal and to the shoal complex. These lithofacies are briefly described in the following subsections:

#### **4.3.1 Poorly sorted intraclasts packstone**

This lithofacies occurs above the dark brownish argillaceous shale of the Lower Khartam Member with erosive contact (Figure 4.11A). This lithofacies consists of a bed with 30 cm thick unit, and is composed of whitish to light beige-colored sediments with poorly sorted, angular anhydritic intraclasts (Figure 4.11B and 4.11C). This lithofacies has a massive matrix with scattered grains of very fine-grain quartz (Figure 4.11D). This lithofacies is interpreted as a transgressive lag deposit and ravinement surface of marine transgression inundation at the bottom of the Upper Khartam Member; it represents transition from continental argillaceous shale to marine carbonate rocks.

#### **4.3.2 Graded mudstones and wackestones to packstones**

Graded bed mudstones and wackestones to packstones lithofacies in the outcrop occur as whitish to light beige beds (Figure 4.12A and 4.12B). The bed thickness ranges from 25 to 65 cm and the stacked bed set thickness ranges from 1 to 1.2 m. The boundaries

between the beds are characterized by erosive marl and are horizontally amalgamated. The mudstone units are massive while the wackestone and packstone units are characterized by some sedimentary structures. These structures are; hummocky cross stratification, climbing lamination, horizontal lamination and low angle trough cross-bedding (Figures 4.12C to 4.12F). The thin sections revealed that the dominant grain types are very fine to fine ooids, detrital peloids and calcisiltites (Figures 4.12G to 4.12I). The depositional energy for this lithofacies is low to moderate and more precisely below a fair-weather wave base and above a storm wave weather base. This was inferred from the sedimentary structures and the grain size. This lithofacies is interpreted to have been deposited as offshore to foreshoal tempestites in a transitional zone between deep and middle ramps.

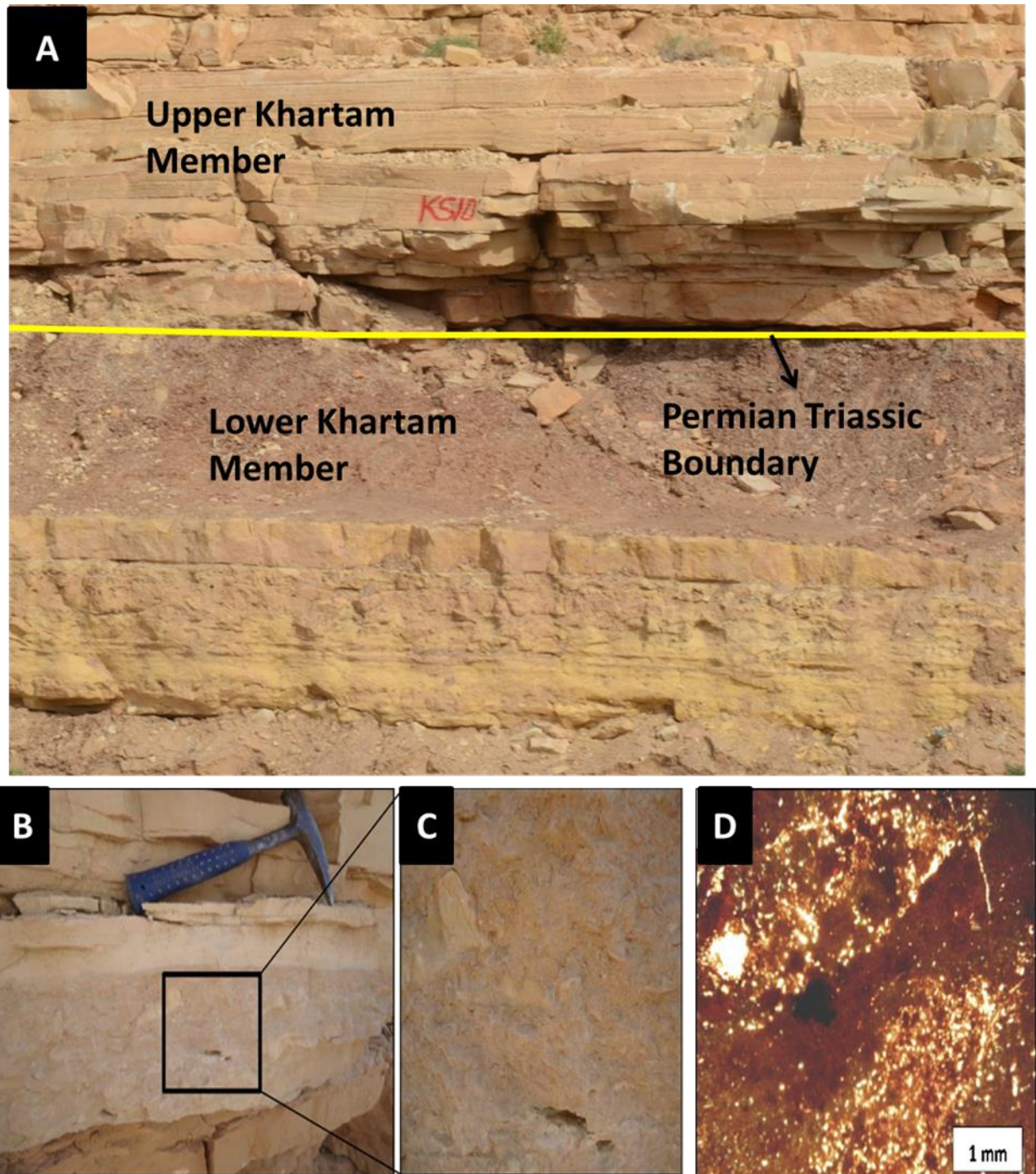


**Figure 4.11** A: The Permian/Triassic boundary interval, B and C: outcrop photographs for intraclasts bed (marine ravinements); (D) thin-section photomicrograph of a sample from this bed. Note the angular clasts in (B) and (C) and fine quartz in (D)



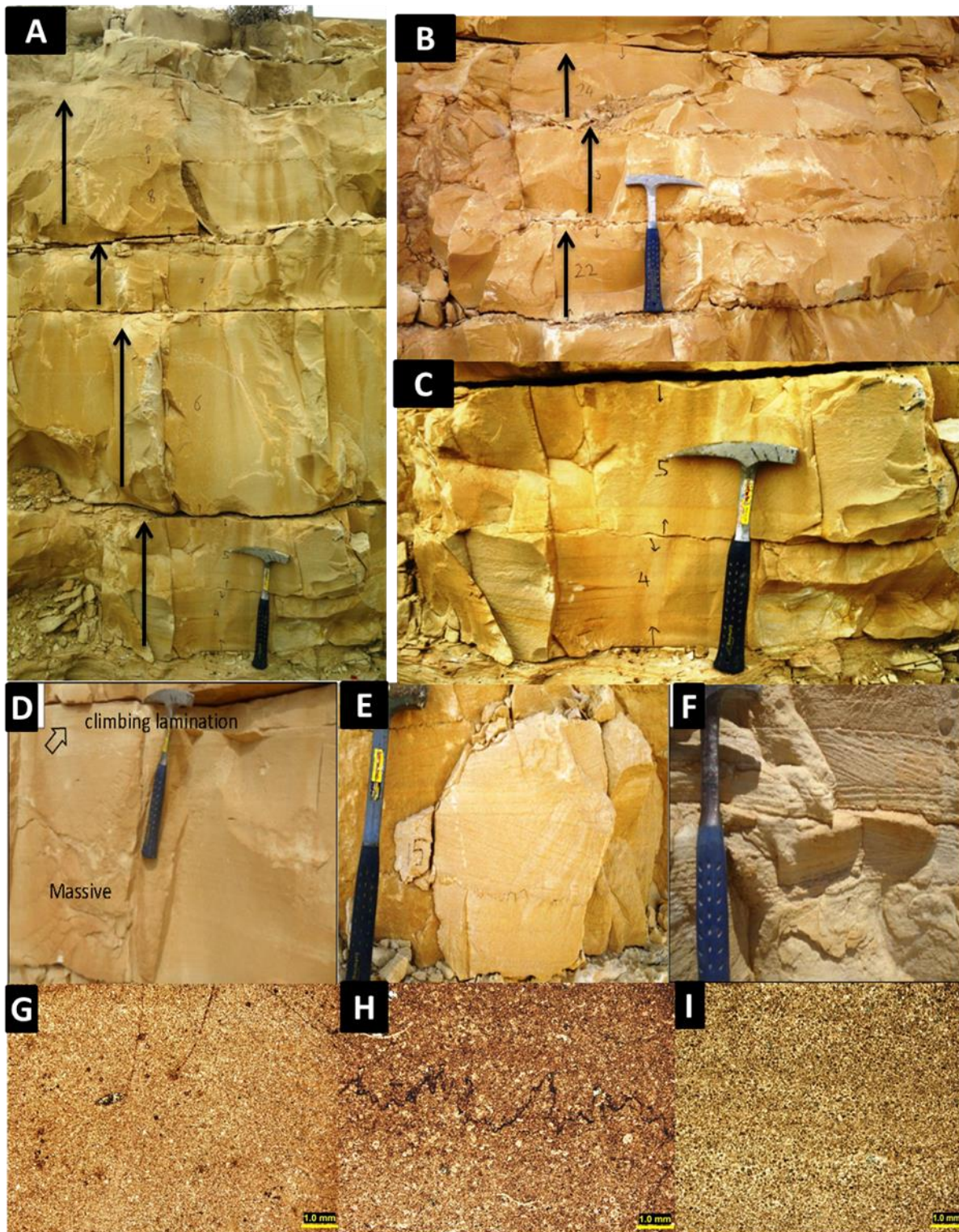


**Figure 4.12 (A) and (B) outcrop photographs for the stacked beds of graded mudstones to packstones lithofacies. The sedimentary structure in this lithofacies includes (C) horizontal lamination; (D) climbing lamination; (E) and (F) low angle trough crossbedding; (G) to (I) The dominant grain types are very fine to fine ooids, detrital peloids and calcisiltites**

### **4.3.3 Shoal complex association**

This part represents the association of grain-dominated oolitic lithofacies (Figure 4.13) and it mainly consists of peloids and oolite grains with varying degrees of sorting, and comprised of three lithofacies:

#### **4.3.3.1 Rippled oolitic peloidal grainstones**

This well-sorted, whitish to brownish peloidal oolitic grainstone to packstone is characterized by well-preserved rippled beds intercalated with fine to very fine marl (Figure 4.14A and 4.14B). The thickness of this lithofacies ranges from 10 to 20 cm, and 50 cm for the stacked bed sets. Grains are dominated by fine ooids and peloids (Figure 4.14C).

#### **4.3.3.2 Massive oolitic grainstones**

This well-sorted, brownish oolitic grainstones lithofacies is dominantly massively bedded at the base and are characterized by well-preserved crossbedding at the top (Figure 4.14D). The thickness of this lithofacies ranges from 10 to 50 cm, and 100 cm for the stacked bed sets. Grains are dominated by well-sorted; fine to medium ooids with scattered peloids (Figure 4.14E). Above this unit there are a lot of microbiolites, which are present in the forms of thrombolites (Figure 4.15A and 4.15B) and stromatolites (Figure 4.15C).

#### **4.3.3.3 Cross-bedded oolitic peloidal grainstones**

Lenticular, flat top and erosive base channels of peloidal oolitic grainstones cut into the sand bars of oolitic grainstone facies. The widths of these lenticular-shaped beds range from 10 to 100 m and thickness of 1 to 3 m. These channels are commonly filled by overlying sediments and show progressive thinning upward. The bars are characterized by horizontal lamination (Figure 4.14F), hummocky cross stratification (HCS) (Figure 4.14G), crossbedding to massive micritized oolitic sands. Grains are dominated by poorly-sorted; coarse to medium micritized ooids with certain amounts of composite grains (Figure 4.14H).

The best modern analog of this lithofacies association is found in the shoal complex of the isolated platforms in the Bahamas (Figure 4.16) (Rankey and Reeder, 2011; Rankey, 2013). According to these researches, the shoal complex was subdivided into outer shelf towards onshore, shoal channels and bars, stabilized shoal and rippled sand. Crossbedded, well-sorted oolitic grainstone beds at the top interval of shoal complex are interpreted to have been deposited in a high-energy bar environments at the concave side of the shoal complex facing the outer shelf. Sand bars are incised locally by channels with varying widths and thicknesses. Aigner (1982), Hughes (2004), and Lindsay et al. (2006) observed similar types of ancient channels in the Upper Jurassic carbonates and interpreted them as deposits of subtidal environments. The stratigraphic relationship and width-thickness ratio of these channels support shoal complex depositional environments interpretation and excludes tidal flat channels environment. The underlying pot and gutter casts and wavy beds suggest storm-triggered channels. The massive oolitic sediments at

the lowermost portion of this lithofacies are interpreted as low energy stabilized shoal. Towards the inner ramp are stabilized shoal followed by carbonate sand banks representing mega ripples deposited under shallow-water high-energy conditions. Aigner (1982), Koehrer et al. (2010) and Pérez-López (2001) have described similar ancient sedimentary features, as in this lithofacies.

#### **4.3.4 Thin marl limestone alternating with grainstones**

This lithofacies overlies the oolitic grain-dominated lithofacies and represents alternating beds of marl limestone and grainstones (Figure 4.17A). The marl beds are soft, fissile and are composed of very fine peloids and calcisiltite. These marl beds are relatively thick, laterally amalgamated and interbedded with very thin beds of brownish, wavy-laminated oolitic grainstones. The thickness of the marl beds decreases vertically while the thickness of the grainstone beds increases vertically until the interval changes to predominantly thick amalgamated peloidal oolitic grainstones.

The marl beds are characterized by cut and fill structures in the forms of gutter casts (Figures 4.17B and 4.17C). These gutter casts, which occur in different shapes and range in size from a few cm to several tens of cm, represent lenticular isolated scoured grain-dominated bodies surrounded by hummocky cross stratified (HCS) fine limestone. The massive in-filling material contains coarse component grains of peloidal intraclastic lithofacies. These gutter casts are massive internally but have wave-rippled top and erosive bottoms. Other different shapes of bodies are observed in the mudstone beds

(Figures 4.17D). These isolated grain-dominated bodies are similar to those described by (Pérez-López, 2001) (Aigner, 1982) as pot casts. These pot casts are also filled with grain-dominated materials.

This lithofacies is interpreted as having been deposited by alternations of fair-weather wave base (grains) and storm weather base (fines) bathymetry (shoal to foreshoal). The presence of gutter and pot casts, hummocky cross stratification (HCS) and wavy ripples indicates high-energy storm waves. The interbedded fine grained limestone was produced by wave oscillations of low energy and suspension loads. Pérez-López (2001) indicated that pot cast deposits require vertical rotary motion by high-energy storms moving in two different directions, with the deposits possibly forming below the weather wave base and just above the tempestites deposits.



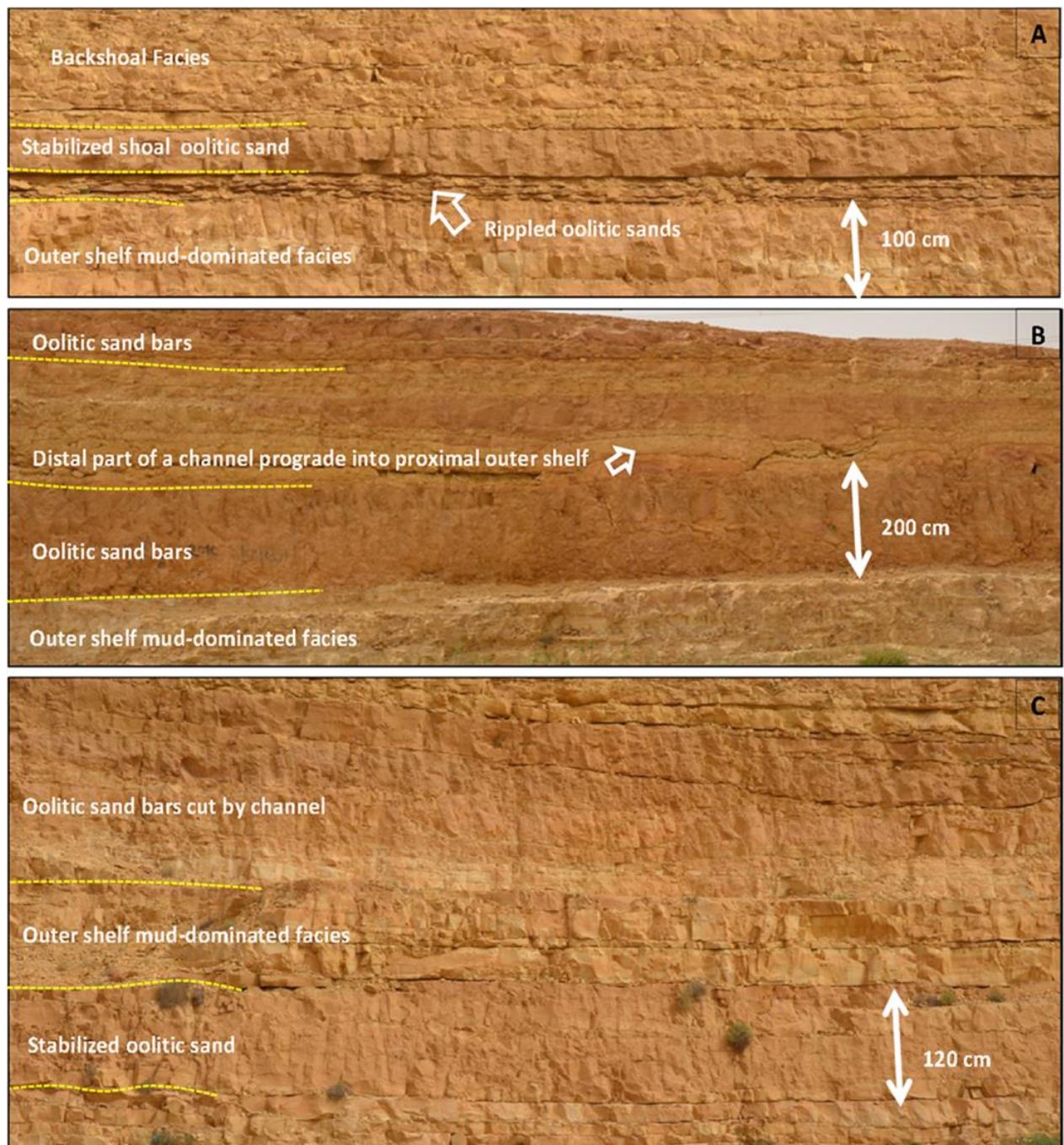


**Figure 4.13** Outcrop photographs show the architectures of the shoal complex facies. The top of these photographs A: show intercalated grain-dominated and mud-dominated beds. The middle of this photograph shows rippled oolitic sand overlain by relatively thick massive oolitic sand which is interpreted as stabilized shoal; The middle part of the photograph B: shows a channel cut into mud-dominated facies this was interpreted as a distal part of a channel prograding into a proximal outer shelf; The bottom part C: shows photograph of oolitic sand bars cut by channel overlain by the stabilized shoal oolitic sand (Eltom et al., 2014b)



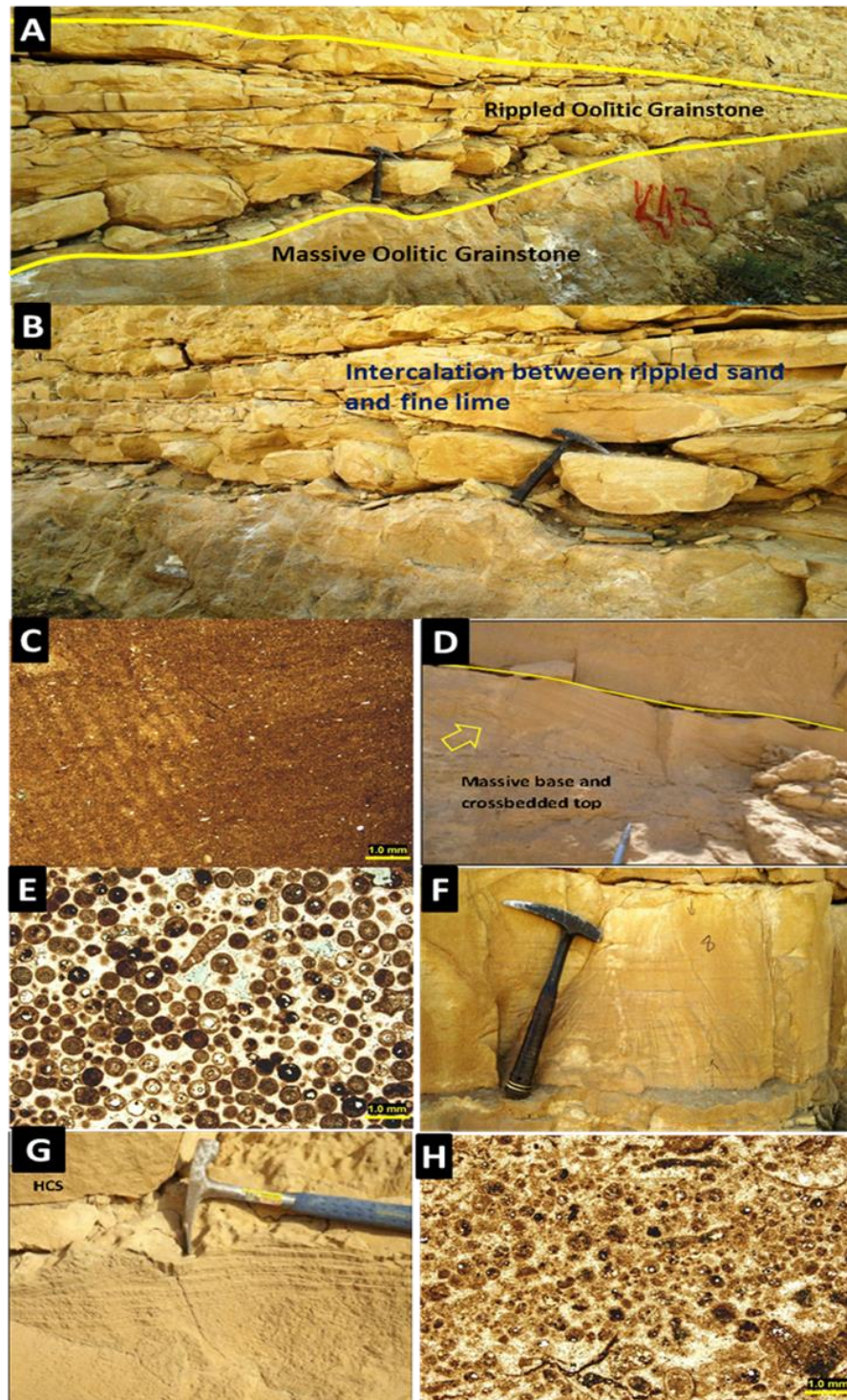
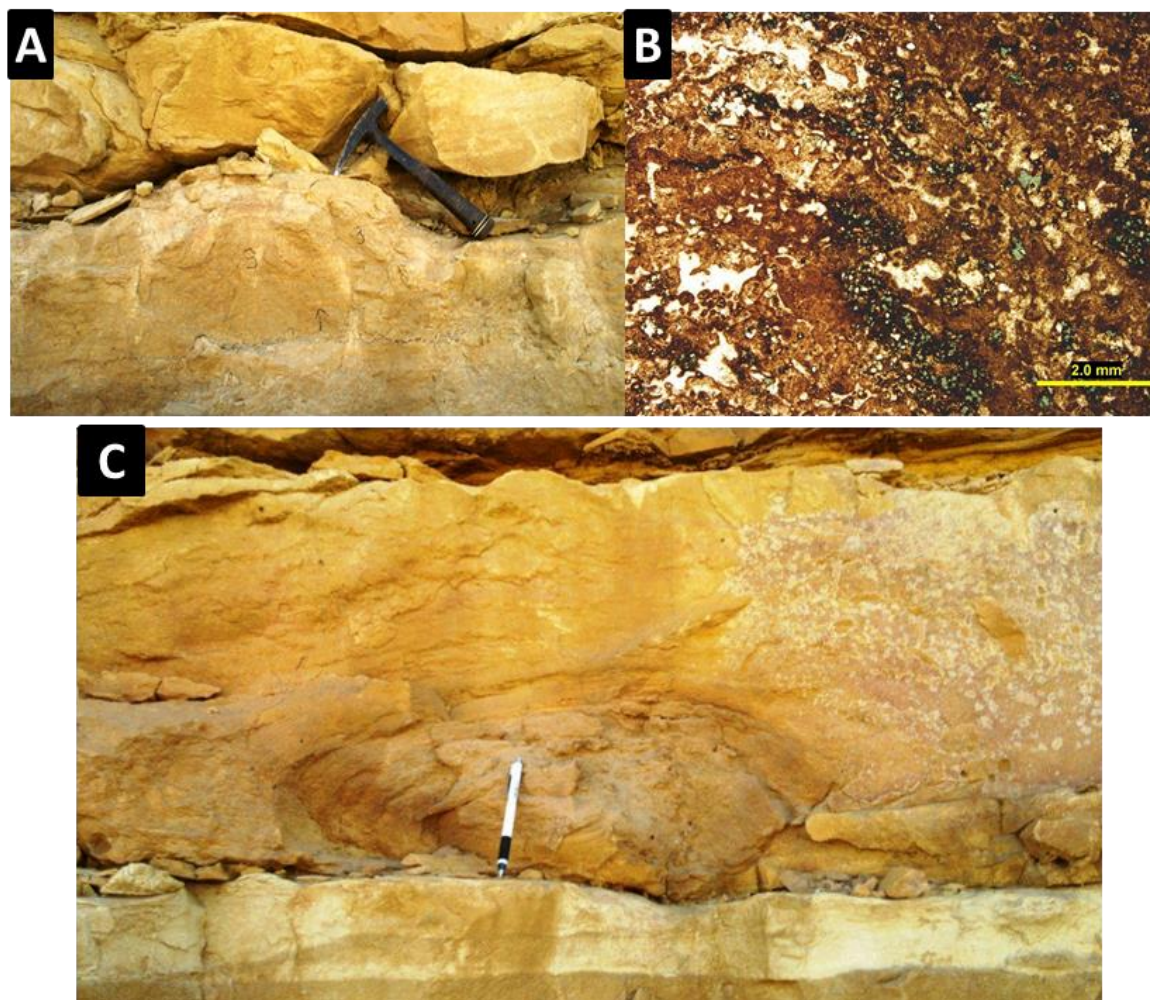


Figure 4.14 Shoal complex lithofacies association. (A) and (B) well-preserved rippled beds intercalated with fine to very fine marl; (C) thin-section photomicrographs of fine ooids and peloids; (D) oolitic grainstone with massively bedded at the base well-preserved crossbedding at the top; (E) thin-section photomicrograph of moderately to well-sorted oolitic grainstone; (G) horizontally laminated bed; (F) HCS; (I) thin-section photomicrographs of poorly sorted micritized oolitic grainstone



**Figure 4.15 Microbiolites in the Upper Khartam Member. (A) plain view of thrombolites in the outcrop; (B) photomicrographs of thrombolites sample showing lamination and clotted fabric; (C) plain view of stromatolite in the outcrop**



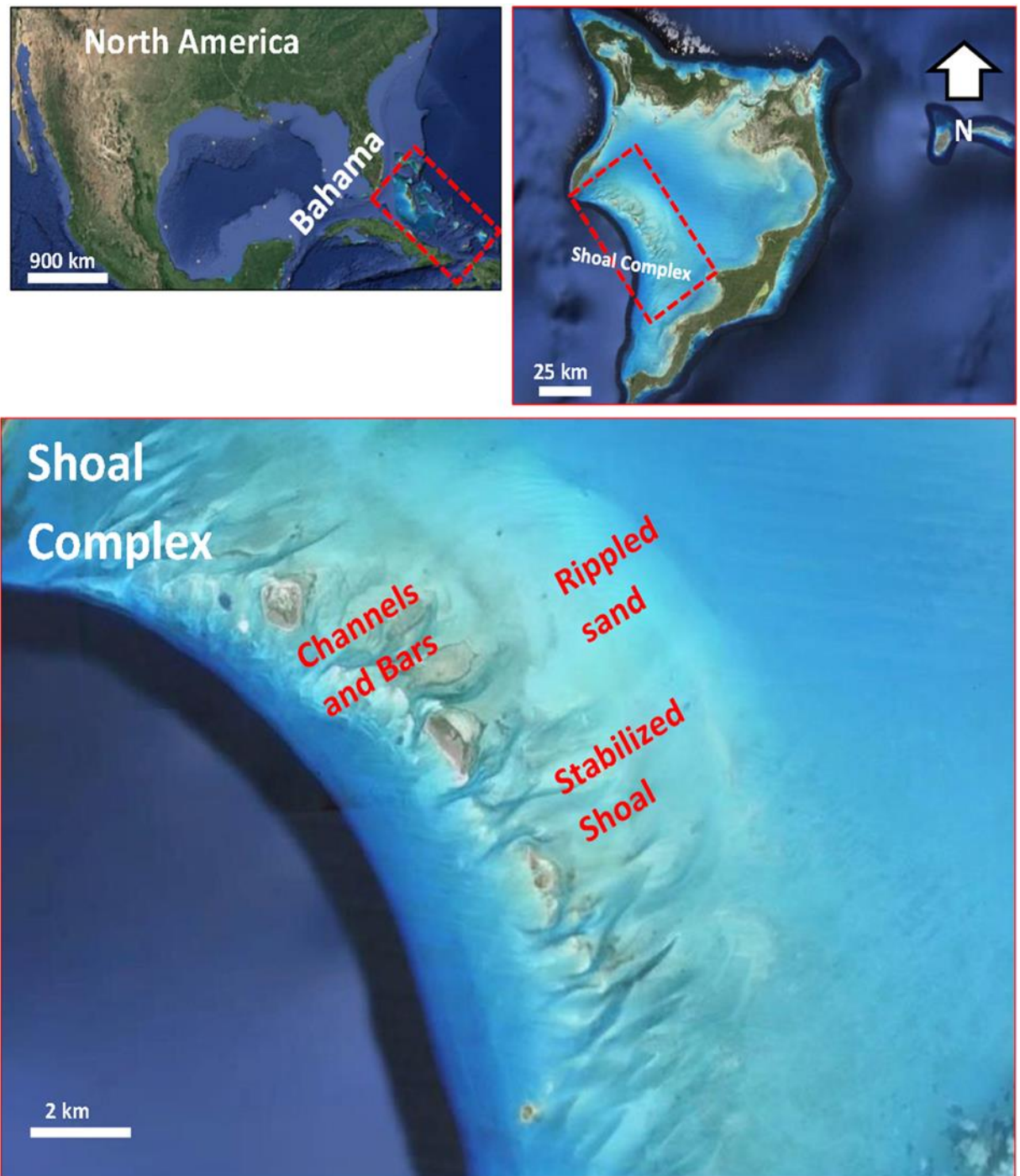
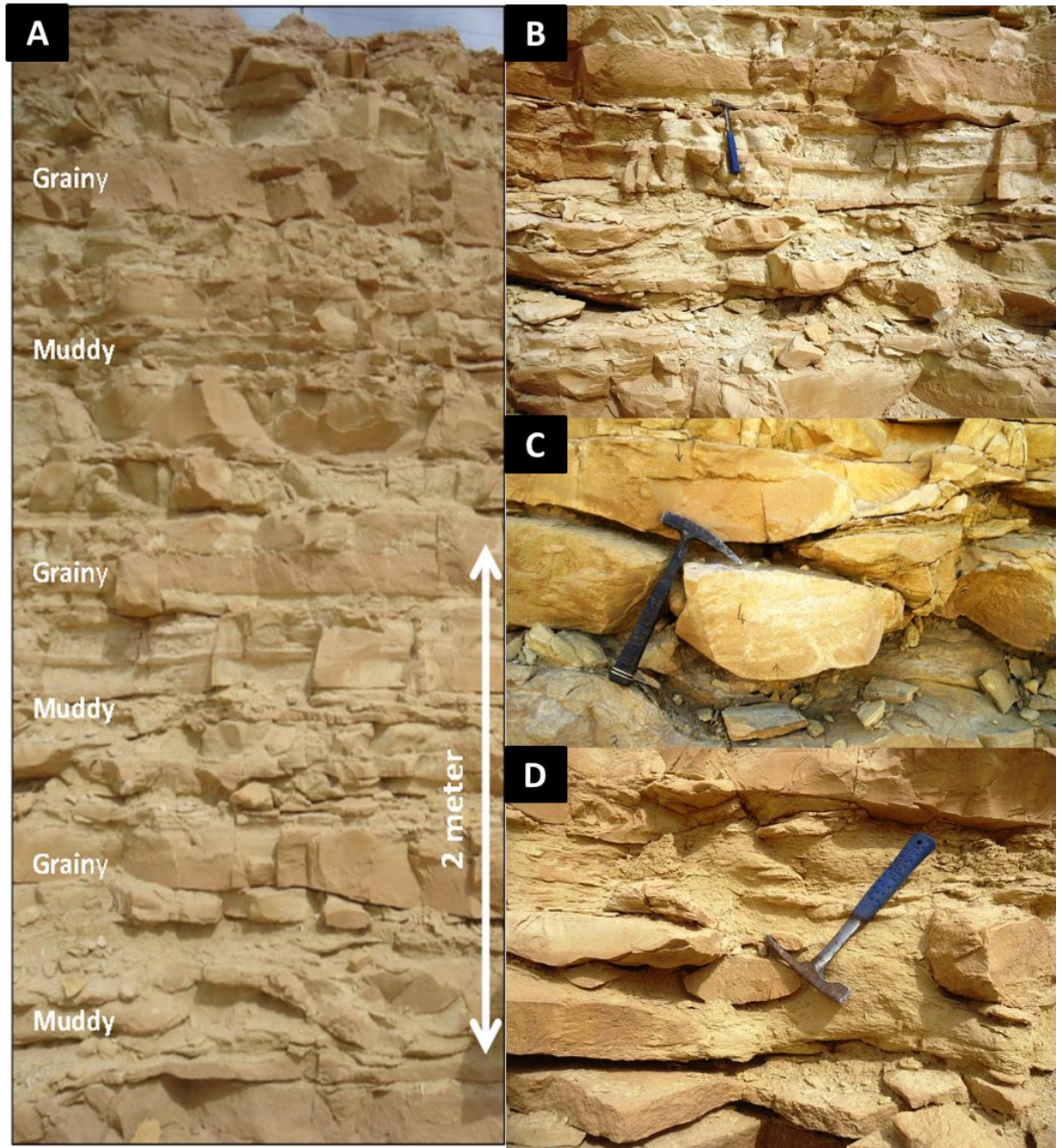


Figure 4.16 Landsat image showing general morphology of different parts of the shoal complex in Crooked-Acklins Island, Bahamas . After Rankey and Peeder (2001) and Rankey (2013)



**Figure 4.17 Thin bed fine limestones alternating with grainstones. (A) alternating beds of fine grained limestone and grainstones; (B) and (C) cut and fill structures in the forms of gutter casts; (D) cut and fill structures in the forms of pot casts (Eltom et al., 2014b)**

#### 4.4 High Resolution Stratigraphy

The part of the Upper Khartam Member in the investigated outcrop consists of three high-frequency sequences (HFSs) (Figure 4.18). Each HFS (cycle set) is composed of cycles that consist of bed sets of genetically related beds. The underlying and overlying boundaries of each HFS are distinctive and traceable surfaces marked by pedogenic and marl deposits. The results in this section were integrated and compared with previous studies of Eltom et al., 2014b in the same study area and with Koehrer et al., 2010 in Oman. The general arrangement of these HFSs, from bottom to top, is briefly defined as follows:

- **HFS-1:** This sequence is about 6.5 m thick. The lower boundary is the Permian\Triassic boundary defined at the base of the Upper Khartam Member and the upper boundary is marked by erosive contact with HFS-2, which is filled by argillaceous marls and overlies the thick beds of oolitic grainstones. The transgressive facies of this HFS consists of beds of poorly sorted intraclasts packstone (marine transgression ravinement) overlain by two beds of offshore to foreshoal mudstone, indicating a very rapid transgression. The regressive part of this HFS shallows-up from foreshoal tempestites graded beds to oolitic grainstones of the shoal complex.
- **HFS-2:** This sequence is about 6 m thick and has similar stacking pattern as the HFS-1. The upper contact with HFS-3 is marked by erosive beds associated with cut-and-fill structures (pot and gutter casts). Marine ravinement was not well



recognized as in HFS-1 and the transgressive part is made-up of offshore to foreshoal mudstones to graded beds mudstones to packstones. The maximum flooding surfaces of the third order Upper Khartam composite sequence were picked at the top of these graded beds. The regressive facies of this sequence consists of wackestones to packstones tempestites of the foreshoal deposits overlain by thick beds of oolitic sand bars and channels and capped by rippled oolitic sand of the shoal complex.

- **HFS-3:** This sequence is about 5 m thick. The upper contact is placed at the top of the burrowed skeletal-peloidal-oolitic grainstones beds that appear on top of the KM-4 section. The transgressive part of this HFS consists of thin beds of mudstone alternating with grainstones of the highly intercalated foreshoal and shoal deposits. The regressive part of this HFS is made-up of the poorly sorted skeletal peloidal oolitic grainstones and packstones of backshoal to shoreface deposits.

These HFSs were compared to the one documented in the previous studies and good match was noticed between them and that reported in the same study area by Eltom et al., 2014b. But in that study a wider area were examined and therefore an additional two HFSs were added to the above discussed three. The upper boundary of the last HFS-5 was the boundary between the Upper Khartam Member and the overlying Sudair Formation. So, these HFSs are stacked vertically to form the Upper Khartam composite sequence. This composite sequence is bounded by unconformities both at the basal contact with the Lower Khartam Member and at its top contact with the Sudair Formation. The stacking pattern of the HFSs within the Upper Khartam composite

sequence exhibits a long-term, shallowing-upward sequence after a short period of marine transgression. HFS-1 and HFS-2 at the bottom of the succession represent seaward foreshoal and shoal deposits and were highly influenced by sediment deposited above the storm wave base. The maximum flooding surface of the Upper Khartam composite sequence is placed at the top of the last tempestites bed in HFS-2. The HFS-3 and HFS-4 are beneath and within the weather wave base and represent shoal and backshoal deposits. Finally, HFS-5 at the top represents tidal to supra-tidal flats that were landward of the weather wave base. The depositional model and the distribution of the HFSs within this model are shown in (Figure 4.19).



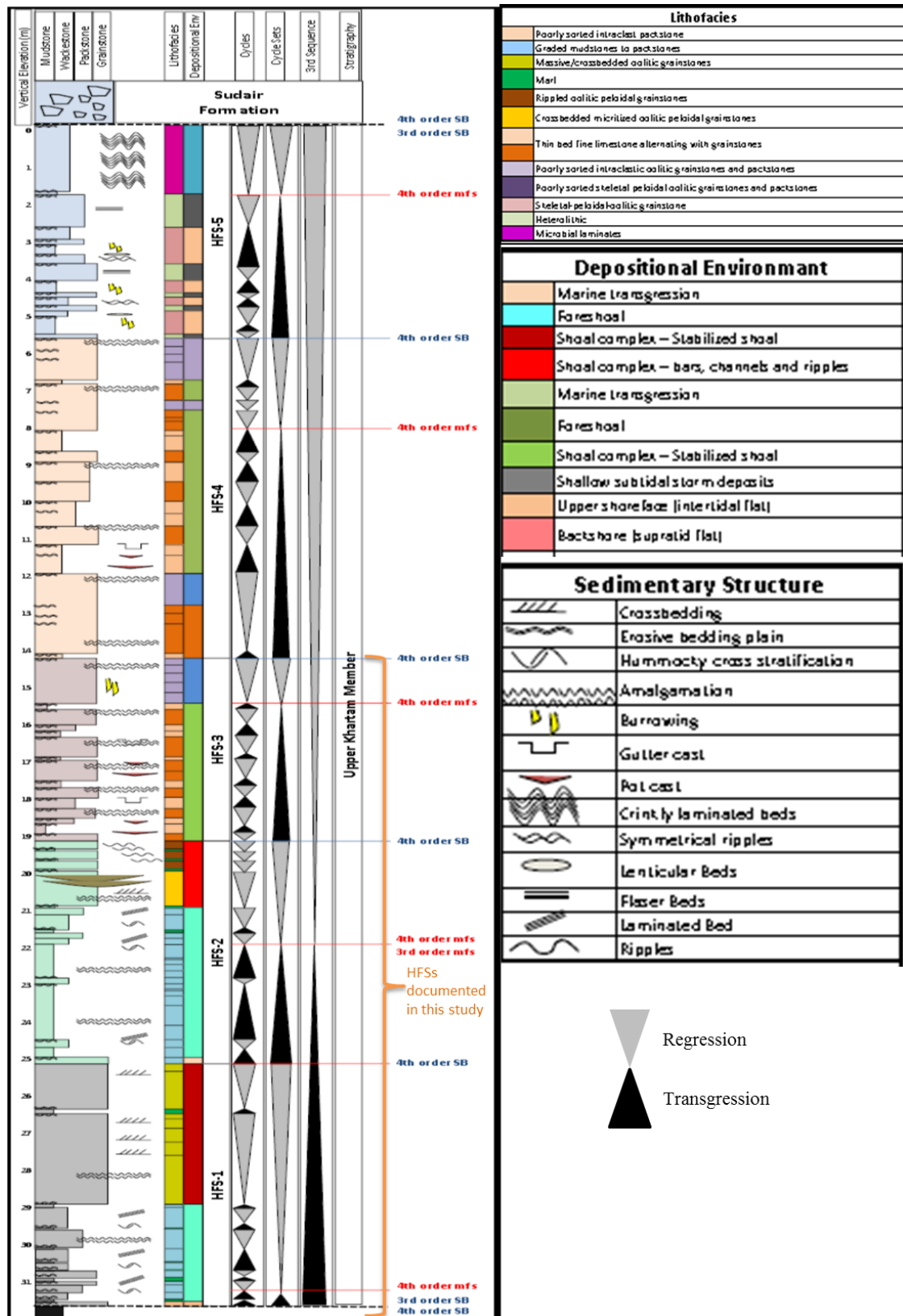


Figure 4.18 High Frequency Sequences and the stacking pattern of Upper Khartam Member (after Eltom et al., 2014b)

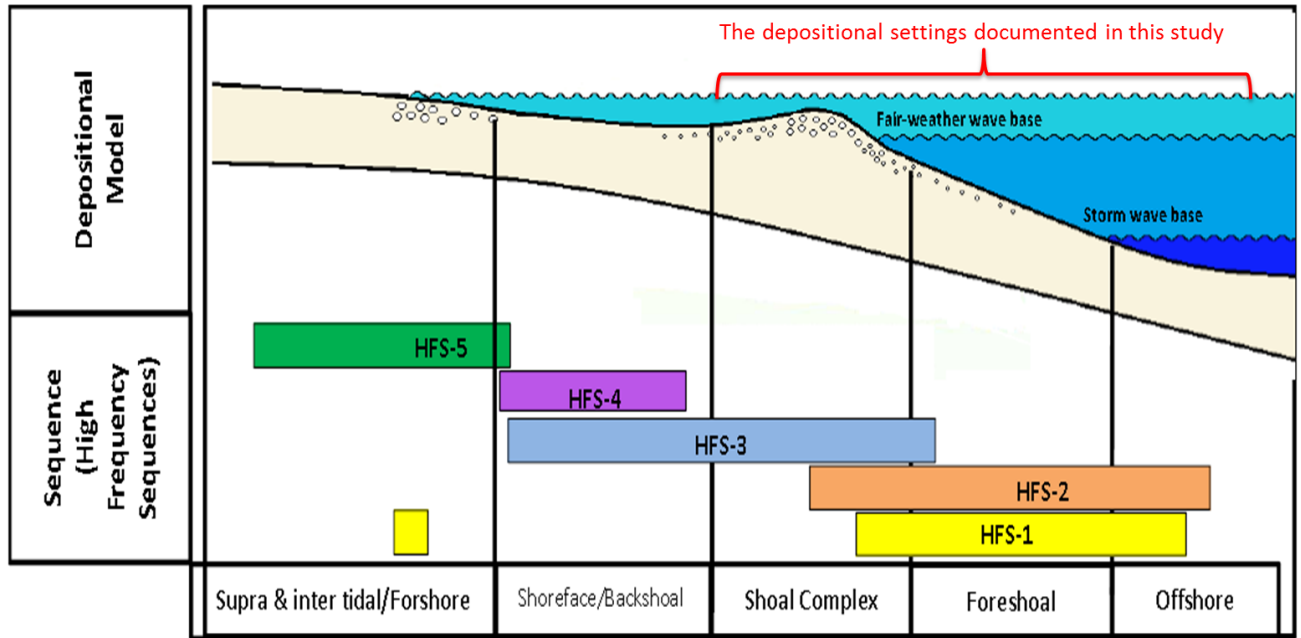


Figure 4.19 Depositional model (ramp complex) showing stratigraphic distribution of lithofacies along the outcrop sections of the Upper Khartam Member. Note that although HFS -1 and -2 represent the deepest part of the model, the lowermost interval of HFS-1 is interpreted as very shallow water (first transgression) (after Eltom et al., 2014b)

## 4.5 Interpretation and Discussion

In the previous study by Vaslet et al. (2005) on the Khuff outcrops, they recognized stromatolite mats, coquina and oolitic grainstone lithofacies in the Upper Khartam Member, and interpreted them to be deposited in an intertidal flat that inter-fingers with infra- and mid-littoral (foreshore to backshore) depositional environments. The lithofacies recognized in this study (Table 4.1) suggest the occurrence of deeper depositional environments including basin-ward from the littoral and backshoal depositional environments (Figure 4.13). The transition from mudstone to packstone tempestites observed in the lower interval of the Upper Khartam Member is interpreted as proximal to distal foreshoal environment. The overlying oolitic crossbedded grainstones are interpreted as shoal complex and shoal bar deposits.

There are some channels having flat tops and erosive bases and they are cutting the tempestites. These channels are interpreted as spill over channels passing from the shoal through the proximal foreshoal to the distal foreshoal. The relationship between thickness and width for these channels indicates that they are not tidal flat channels. Hughes (2004, 2009) and Lindsay et al. (2006) observed a similar channel type cutting through basinal lithofacies in the Upper Jubaila Member (lower Arab-D reservoir composite sequence). Hughes (2009) indicated that the progressive upward narrowing and deepening of the channels might indicate a progradation of the channel complex, and therefore a shallow-water environment. Conversely, in the locality of this study, the channels have higher width and lower thickness signatures, which may indicate more offshore facies succession.

**Table 4.1 Summary of the lithofacies reported in this study and their description and interpretation**

<b>Lithofacies</b>	<b>Description</b>	<b>Interpretation</b>
Poorly sorted intraclasts grainstones	Poorly sorted angular possibly anhydritic intraclasts, massive matrix with scattered very fine grain quartz.	The transgressive lag and revainment surface of the inundation marine transgression.
Graded mudstones and wackestones to packstones	The mudstones are massive but the wackestone and packstone have different sedimentary structures and the dominant grain types are very fine to fine ooids and detrital peloids and calacsilitites.	Deposited below a fair-weather wave base and above a storm wave weather base. Represent offshore to foreshoal tempestites.
Rippled oolitic peloidal grainstones	Well-preserved rippled beds intercalated with fine to very fine marl. Grains are dominated by fine ooids and peloids.	Carbonate sand banks representing mega ripples deposited under shallow-water high-energy conditions.
Massive oolitic grainstones	Massively bedded at the base and are characterized by well-preserved crossbedding at the top. Grains are dominated by well-sorted; fine to medium ooids with scattered peloids.	Deposited in a low energy stabilized shoal.
Cross-bedded oolitic peloidal grainstones	Lenticular, flat top and erosive base channels of peloidal oolitic grainstones cut into the sand bars of oolitic grainstone facies. Grains are dominated by poorly sorted; coarse to medium micritized ooids with certain amounts of composite grains.	Deposited in a high-energy bar environments at the concave side of the shoal complex facing the outer shelf.
Thin marl limestone alternating with grainstones	The marl beds are very fine, soft, fissile and compose of very fine grains ooids and calacsilitite. Interbedded with brownish, wave laminated skeletal oolitic grainstone, thick laterally amalgamated, characterized by cut and fill structures in the forms of gutter casts and pot casts.	Deposited by alternations of fair-weather wave base (grains) and storm weather base (marls) bathymetry (shoal to foreshoal) with high-energy storm waves.

The presence of thrombolites heads within the graded tempestites mudstones to packstones foreshoal and above the shoal complex facies cannot be used as shallow-water indicator. These thrombolites heads are scattered and are locally found associated with relatively thick muddy facies beds, which suggests deep water conditions. These deep-water conditions (subtidal) were likely similar to those of the Devonian reef complexes of the Canning Basin, Western Australia, where colloform thrombolites types were recorded (George, 1999). According to George (1999), the occurrences of thrombolites in stratigraphic records are not restricted to shallow waters, and therefore, they are not strictly diagnostic evidence for very shallow water environments alone.

There is an impact of storms on the depositional environments of Upper Khartam Member and that was inferred by the sedimentological model with the following evidences:

- Intensive bed amalgamation.
- The presence of tempestites graded mudstone to packstone beds.
- Gutter and pot casts.
- Spill over channel deposits.
- Chips of large intraclasts and the presence of medium to coarse grained sub-angular quartz grains.

Recently, detailed studies were conducted in outcrop analogs for the Khuff Formation in Oman (e.g. Koehrer et al., 2010, 2012). These studies showed almost similar lithofacies to the one documented in this study. So, the next Table 4.2 shows a comparison between the lithofacies documented in Oman outcrop and the one reported in this study and the study by Eltom et al., 2014b in the same area in Saudi Arabia.

The Upper Khartam Member in the study area consists of five cycle sets (HFSs). Similar number of cycle sets was observed in the Upper Khuff carbonate above the Permian\Triassic boundary and below Khuff – Sudair unconformity in Oman by Koehrer et al. (2010) and were grouped into KS2 and KS1. There are no evidences of pronounced exposure in intra – Upper Khartam to group these five HFSs into two composite sequences and this can be refined by investigation. The total thickness of these five HFSs is about 31.5 m while the thickness of KS1 and KS2 in Oman ranges between 101 m to 134 m (around one third of the Upper Khartam Outcrop section in this study).

**Table 4.2 A comparison between lithofacies associations for Upper Khartam Member in Saudi Arabia and its equivalent in Oman**

<b>Lithofacies Association</b>	<b>This study and Eltom et al., 2014b (Saudi Arabia)</b>	<b>Koehrer et al. (2010) (Oman)</b>
Offshoal to basinal (low-energy, below storm wave base)	Not documented	Documented LFA 8
Marine transgression (very high energy)	Documented	Not documented
Foreshoal (low- to moderate-energy, between fair-weather wave base and storm wave base)	Documented	Documented LFA 7
Beach / Barrier island (high-energy subaerial setting)	Not documented	Documented LFA 6
Shoal complex (moderate- to high-energy, above fair-weather wave base)	Documented	Documented LFA 5
Backshoal and shoreface (low- to high- energy)	Documented	Documented LFA 4
Tidal to supratidal (intertidal supratidal setting)	Documented	Documented LFA3, LFA2 and LFA 1

## **CHAPTER 5**

# **DIGITAL OUTCROP MODEL**

### **5.1 Introduction**

The recently widely used LiDAR technique in the geological modeling was conducted here to produce a digital outcrop model for the Upper Khartam Member. The digital model did not cover the whole outcrops of Upper Khartam in the area but only one road cut has been selected to be modeled. The selected outcrop covers the upper part of HFS-1 and the whole HFS-2 and HFS-3 and the lower part of HFS-4.

In this part the workflow from the planning in the field to the interpretation of the digital model will be illustrated. Generally, the construction of the digital model passes through three major steps those are; acquisition, processing and interpretation.

### **5.2 Field Planning**

Usually, the first step before starting the laser scanning is to make a reconnaissance for the outcrop location and to decide about the scan positions and reflectors also. The positions should be determined according to several factors such as; accessibility, noise percentage, possible objects might come across the laser ray, sun light and shadow, the



orientation of the outcrop and the desired resolution of the model. The consideration of all these factors combined together will result in the best and accurate digital model.

Here, there is an outcrop facing the target outcrop and the distance was 100 m between them and the length of the studied outcrop is 400 m. In the planning (Figure 5.1) the scan positions were set to be four scans and from the top of the facing outcrop with a spacing of 100 m between each position and the other. The reflectors were put at the top of the facing outcrop also and the spacing about 100 m starting in the midpoint between the first two scan positions, another two reflectors were put on the ground between the two outcrops. Also, the GPS and the external digital camera were operated from each scan position at the same time.

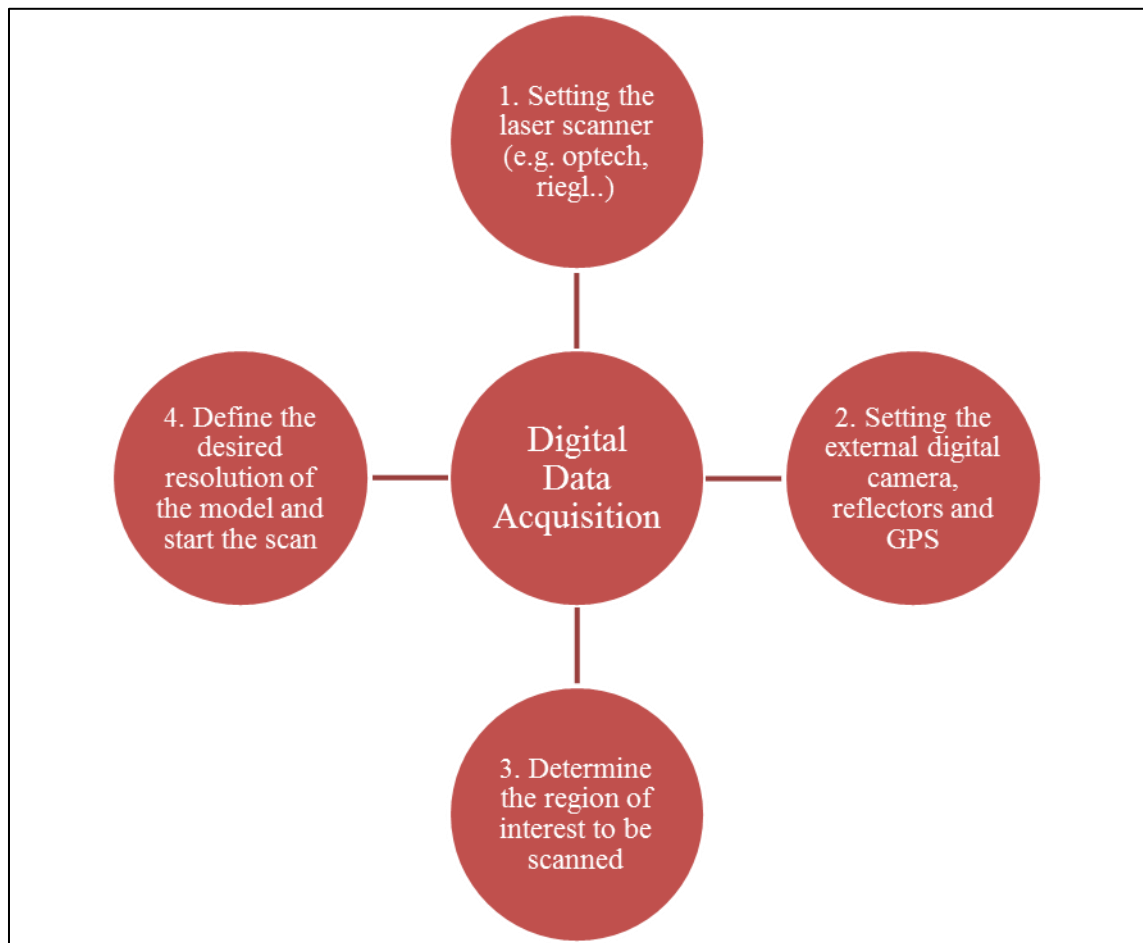


Figure 5.1 The planning for the LiDAR scanning in the field

### 5.3 Digital Data Acquisition

The workflow for the acquisition is summarized in (Figure 5.2). After determining the scan positions and the reflectors positions, the next step is to setting the required equipment to start the laser scanning procedure. The equipment that used in this study are: a terrestrial laser scanner called RIEGL VZ-4000 which has a range reach 4 Km, external high resolution digital camera, prismatic reflectors and differential GNSS. The scans have been done in the previously determined four positions from different angle of view. Each scan position has yielded three to four digital files acquired from the outcrop. All these scans from a single position will be combined later time but they were aligned since they were scanned from same position. Data from other scan positions were not aligned and need to be aligned together using reflectors. The purpose of different scan positions and angles is to avoid any gaps or shadow areas in the final digital model. So, the more scan positions and angles are done the more clean and accurate digital model will be produced.

This version of the laser scanner is vertical line technology and its measure in a field of view of these angles  $60^{\circ}$  to  $360^{\circ}$ . So, the first thing the instrument will do when mounted on the tripod is to rapidly scan the whole area with  $360^{\circ}$  of view at low resolution to be used for fine scan the reflectors. This first scan will be integrated with the next scans. There are some parameters that should be determined in the field laptop before starting the scan which are: the area of interest (referred to the part of the outcrop to be scanned), the desired resolution (here we used 5 mm) and the precision percentage (Figure5.3).



**Figure 5.2 Summary of the workflow for the acquisition of the digital data**



**Figure5.3 The acquisition of the digital data**

The reflectors are placed on the target outcrop and on the one that face it “where the scan positions are located” and also on the ground between the two outcrops. These reflectors are geo-referenced by the differential GNSS and will help in the alignment of all scans and in the geo-referencing of the final digital model. Also, all the scan positions will be geo-referenced by the differential GNSS.

Now when everything is ready, the laser scan starts to emit the ray to the outcrop in a vertical sense. The average time for each scan is about 30 minutes in this study but usually it depends on the determined resolution and the precision degree. The photographs by the attached camera are also taken automatically by the instrument. Higher resolution photos were also taken by another external digital camera.

## **5.4 Digital Data Processing**

The workflow for the processing steps is summarized in (Figure 5.4). The raw data collected in the field are displayed in the office as so called “point clouds”. These point clouds can be displayed either as grey colored or Red Green Blue (RGB) colored photos. So, the first step is to display the final point clouds model for the whole area around the outcrop and captured by the instrument. The laser scanner captures anything that comes across its ray, so in the final result there will be some undesirable points. The point clouds need to be cleaned from all these undesired objects until the best view is achieved (Figure 5.5). The first visualization and the cleaning of the point clouds are achieved by using the RiSCAN Pro software. Also, each scan position has its own point cloud file with the scanner format but the same software was used to convert each file to an ASCII file.

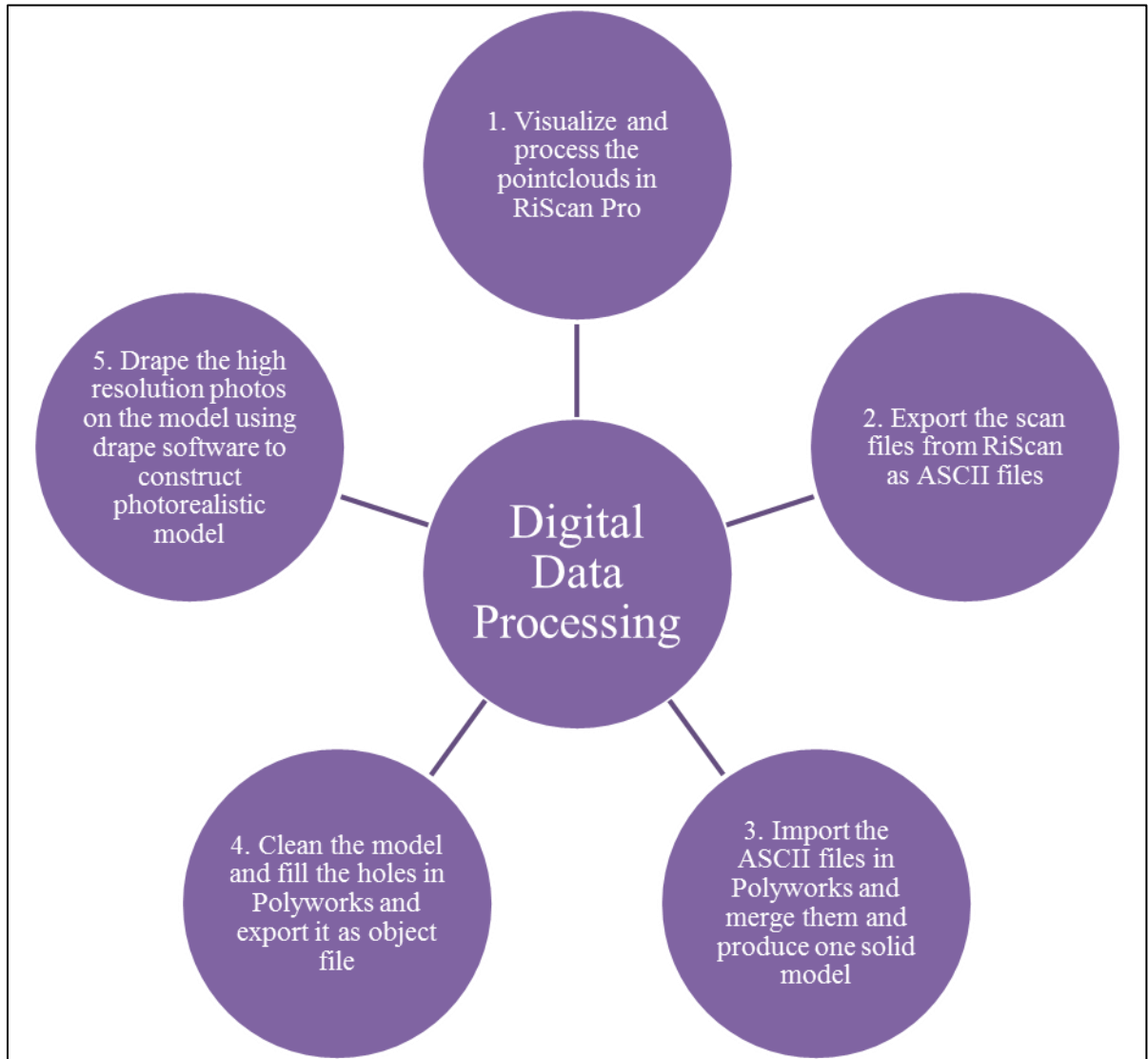


**Figure 5.4 Summary of the workflow for the processing of the digital data**

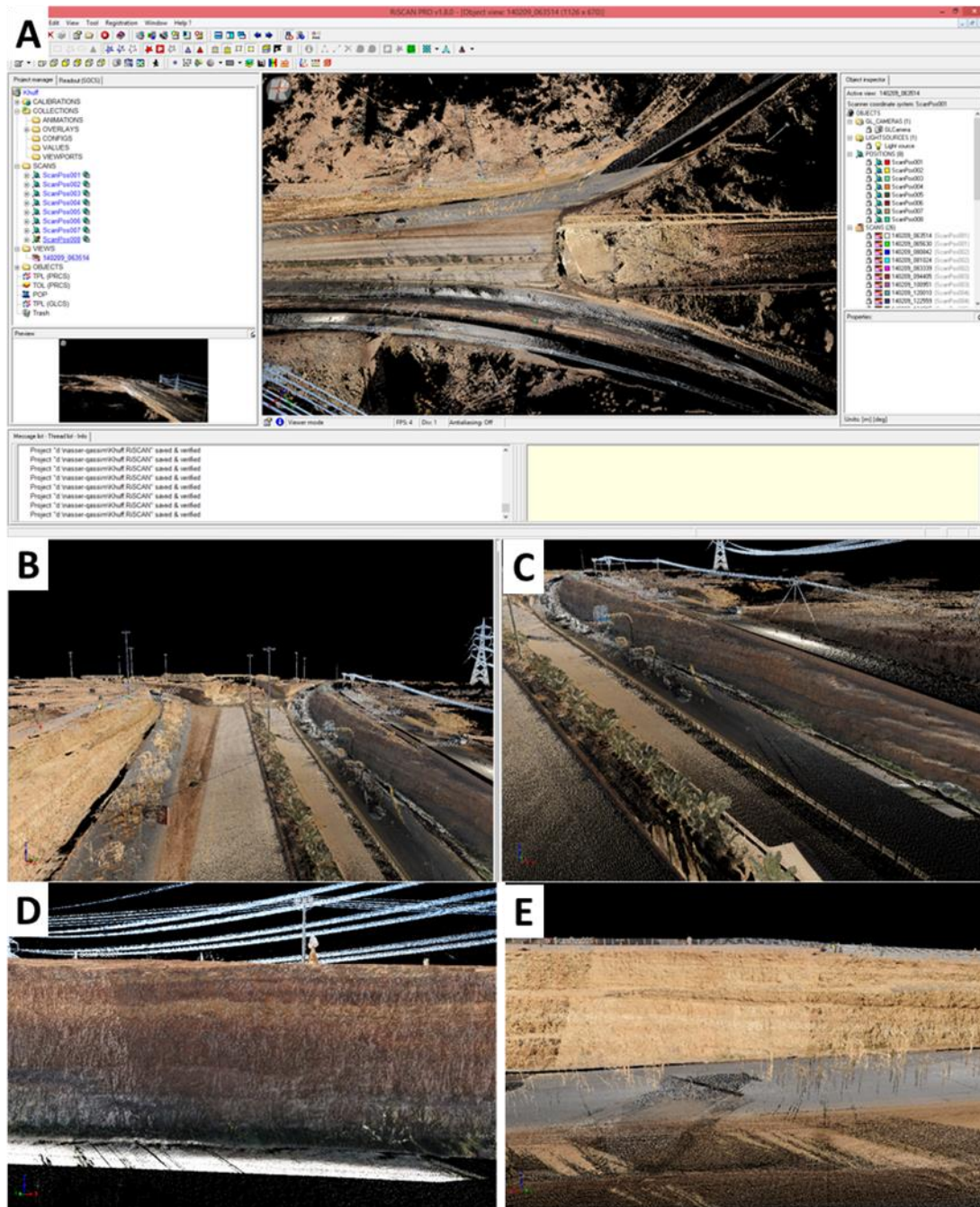


**Figure 5.5** Visualizing of the colored point clouds using RiSCAN Pro software; **A:** the interface of the software and the map view from the point clouds; **B and C:** zoom out display from the target outcrop; **D and E:** zoom in to the face of the target outcrop of the Upper Khartam Member



The next step of the processing was done by the Polyworks software and its toolbox from the aligning of the scans to the construction of the polygonal model. After the four scan files have been converted to ASCII files, they are imported to the IMAlign tool in Polyworks software. The files are imported as grey not RGB colored point clouds to do the rest of the processing steps (Figure 5.6). The imported files are displayed clearly in black background which allows differentiating between the desired point clouds from the undesired points around the outcrop. So, this is a good opportunity to clean the point clouds and minimize the size of the file (Figure 5.7). Then, the model displayed on the purple clipping plane to select the part of the point cloud to be interpolated and hide the rest (Figure 5.8). This step is done to reduce the size of the file and to enhance the accuracy of the final triangulated model.

The triangulation or decimation is a process that produces a solid mesh surface by connecting the points as triangles and the final model is called the polygonal model. This process minimizes the size of the point cloud file and makes it easy to interpret. After selecting the first part of the model to be triangulated, some parameters should be determined for the triangulation. These parameters are: max edge length, interpolation step and max angle and these parameters depend on the desired resolution. Here, these parameters were set to 0.05 m, 0.5 m and  $89^{\circ}$  respectively, after that the triangulation process started for the first part (Figure 5.9) and (Figure 5.10).

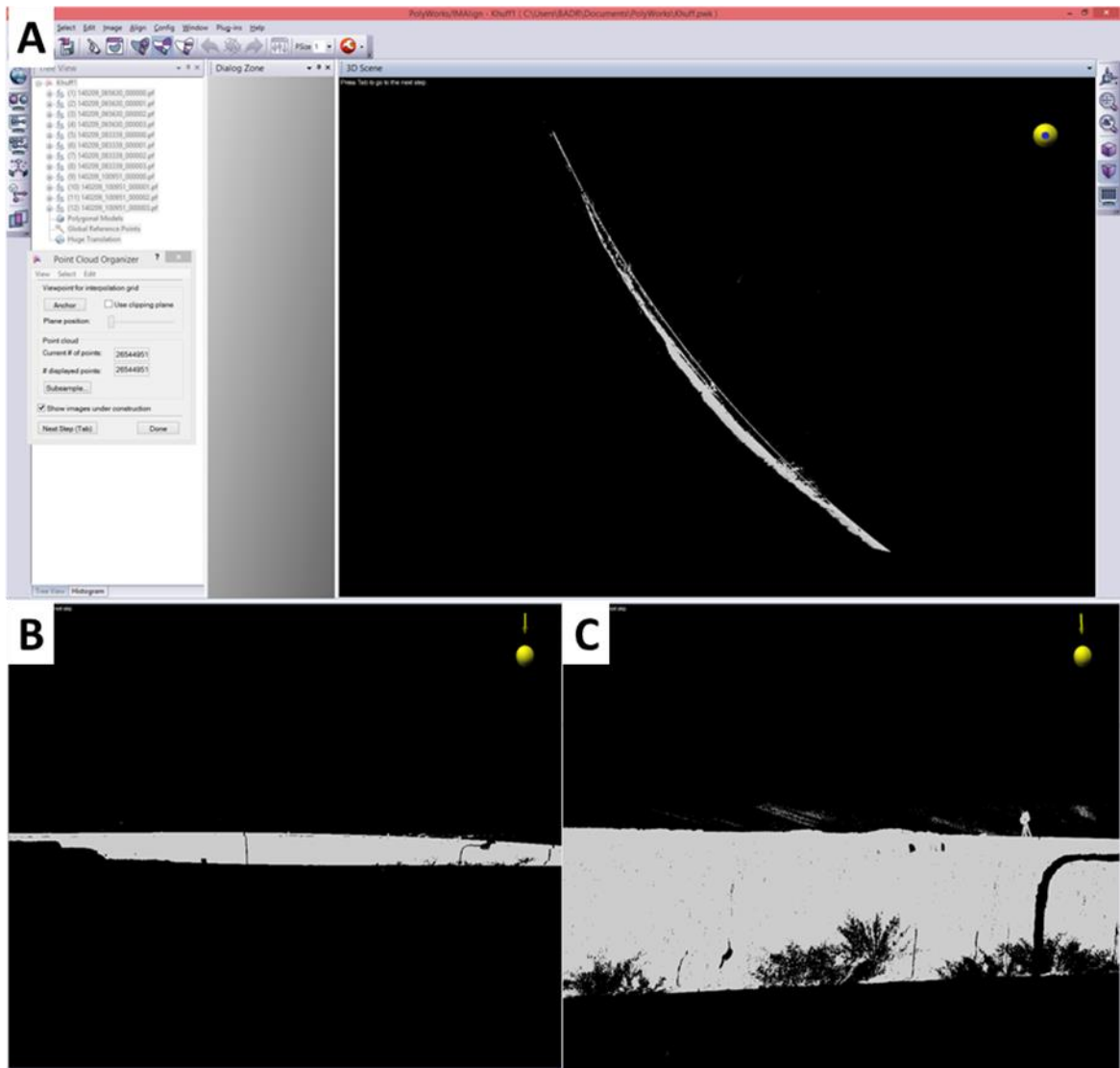


**Figure 5.6 Importing the ASCII files in IMAlign; A: the interface of the software and one file has been imported and displayed; B and C: different views and zoom in to the point cloud data**

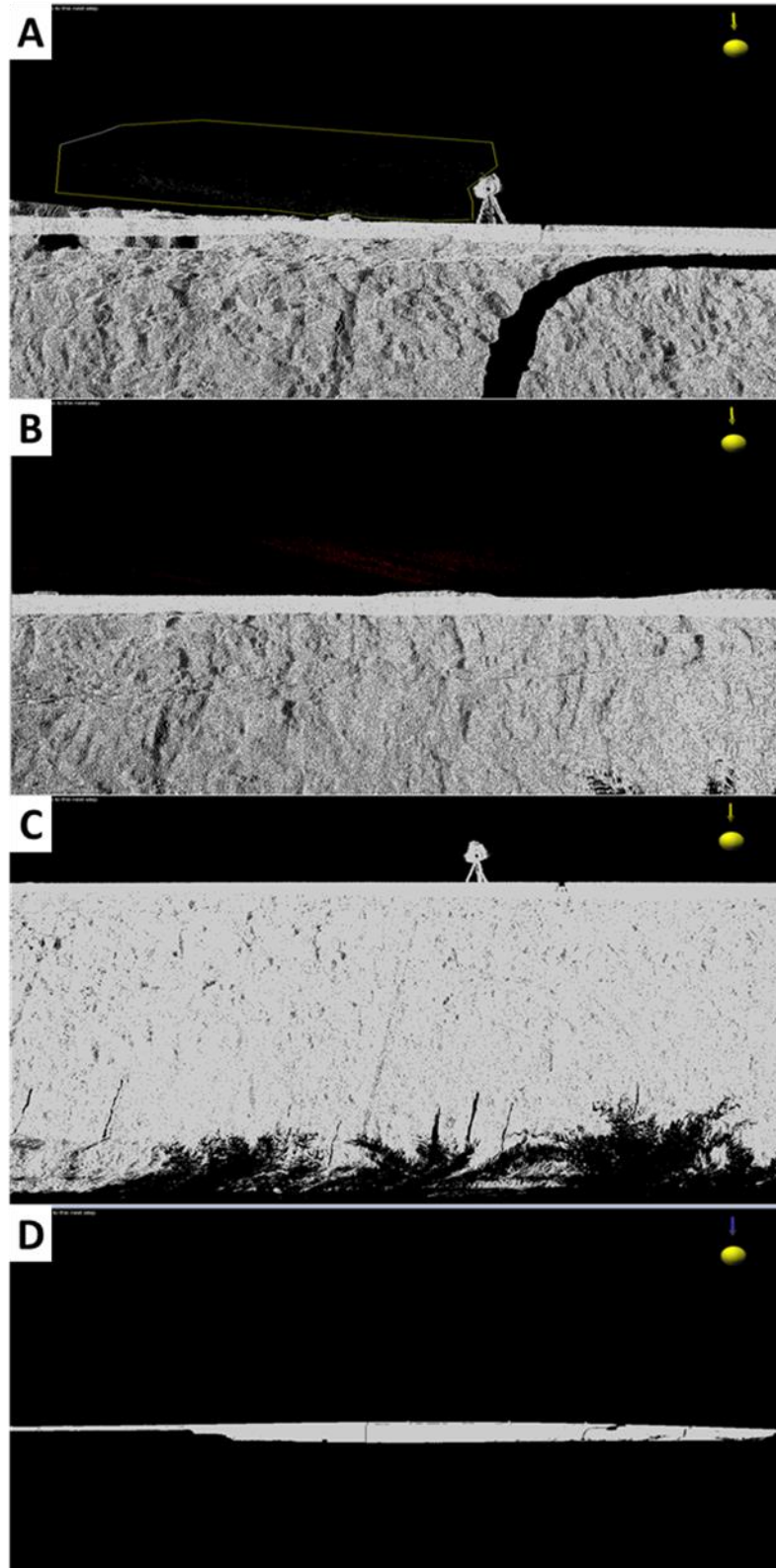


**Figure 5.7** Cleaning the point cloud; A: selecting the undesired points; B: The selected points marked by red color; C and D: the point cloud after cleaning the point cloud

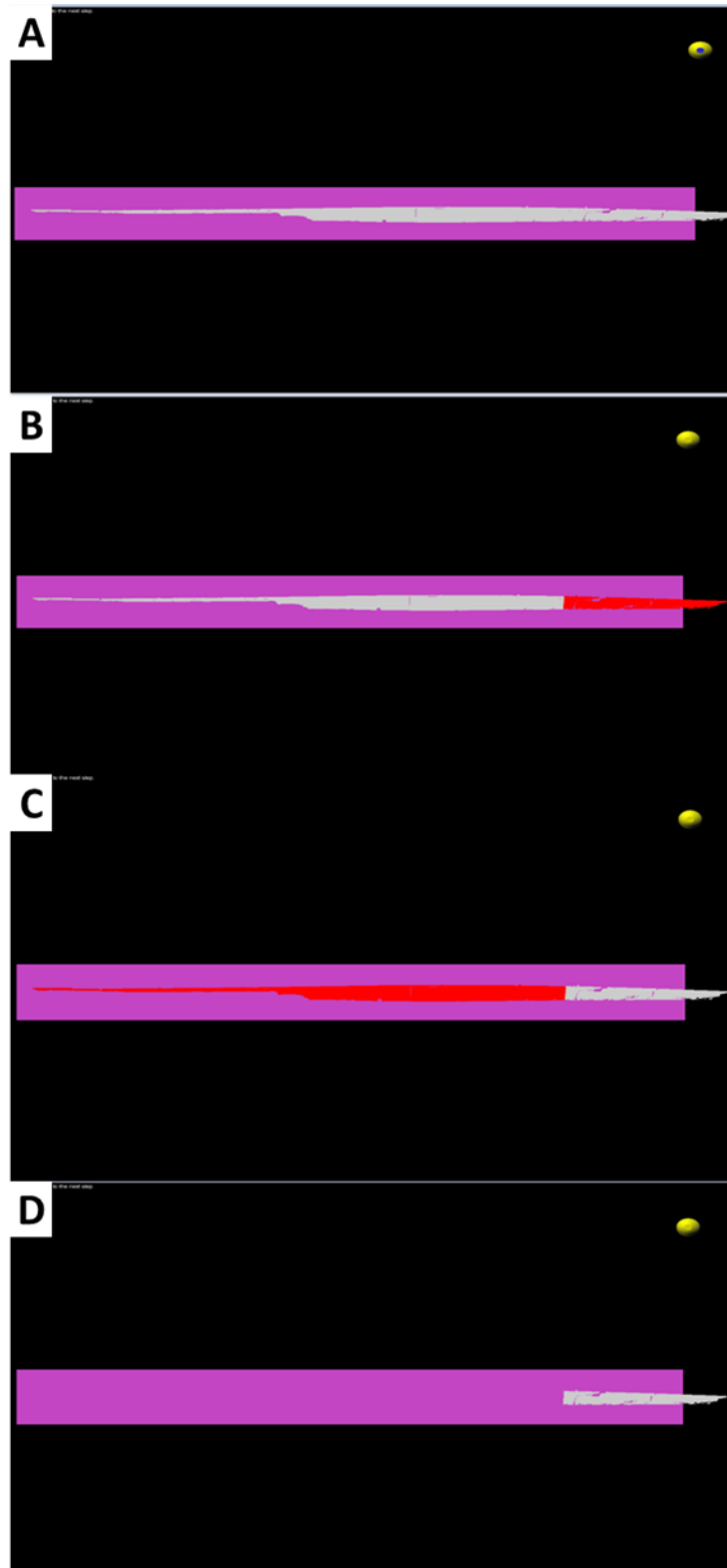


**Figure 5.8** A: displaying the model on the clipping plane; B: selecting the first part to be triangulated; C: inverting the selection; D: hide the rest of the model

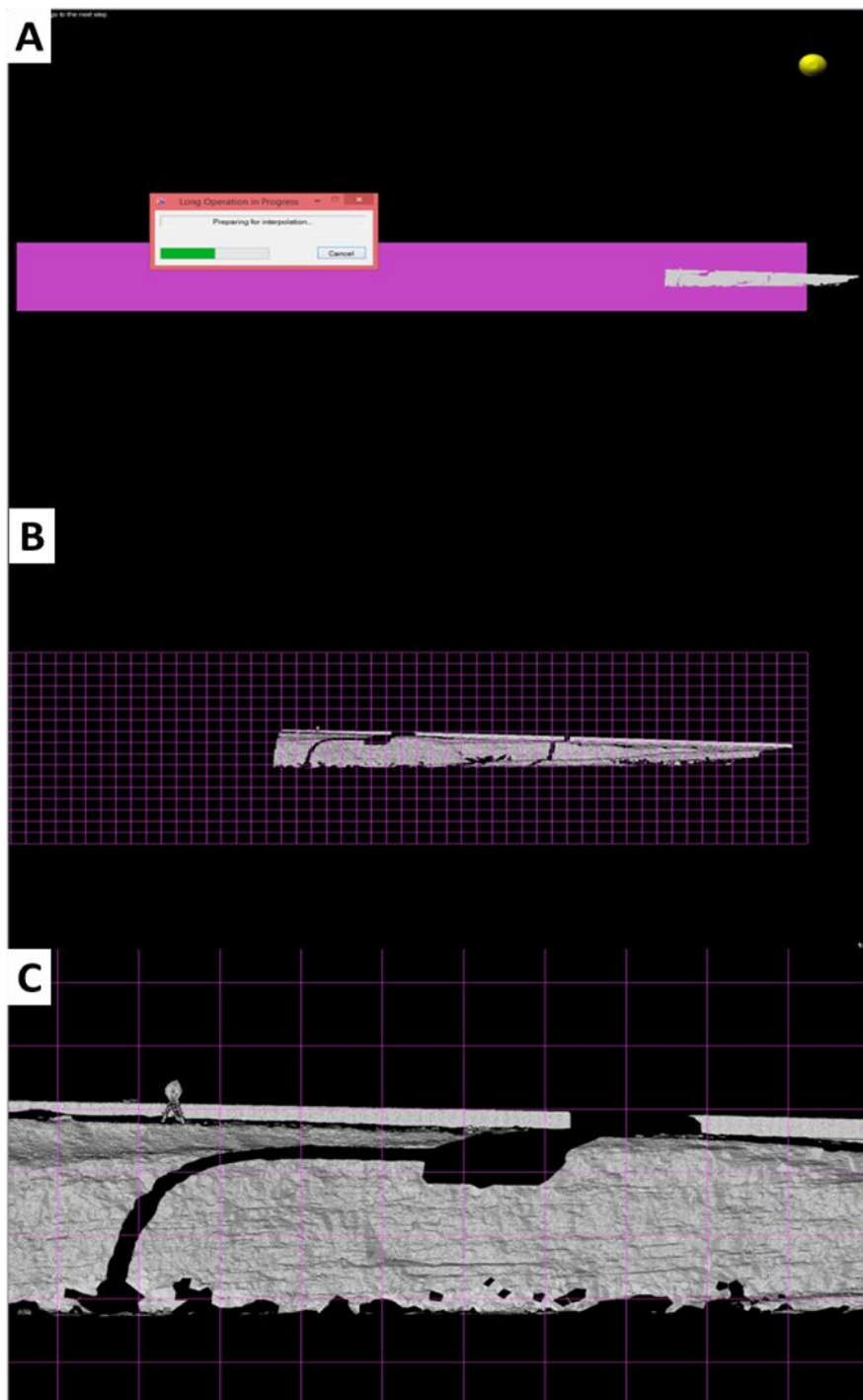
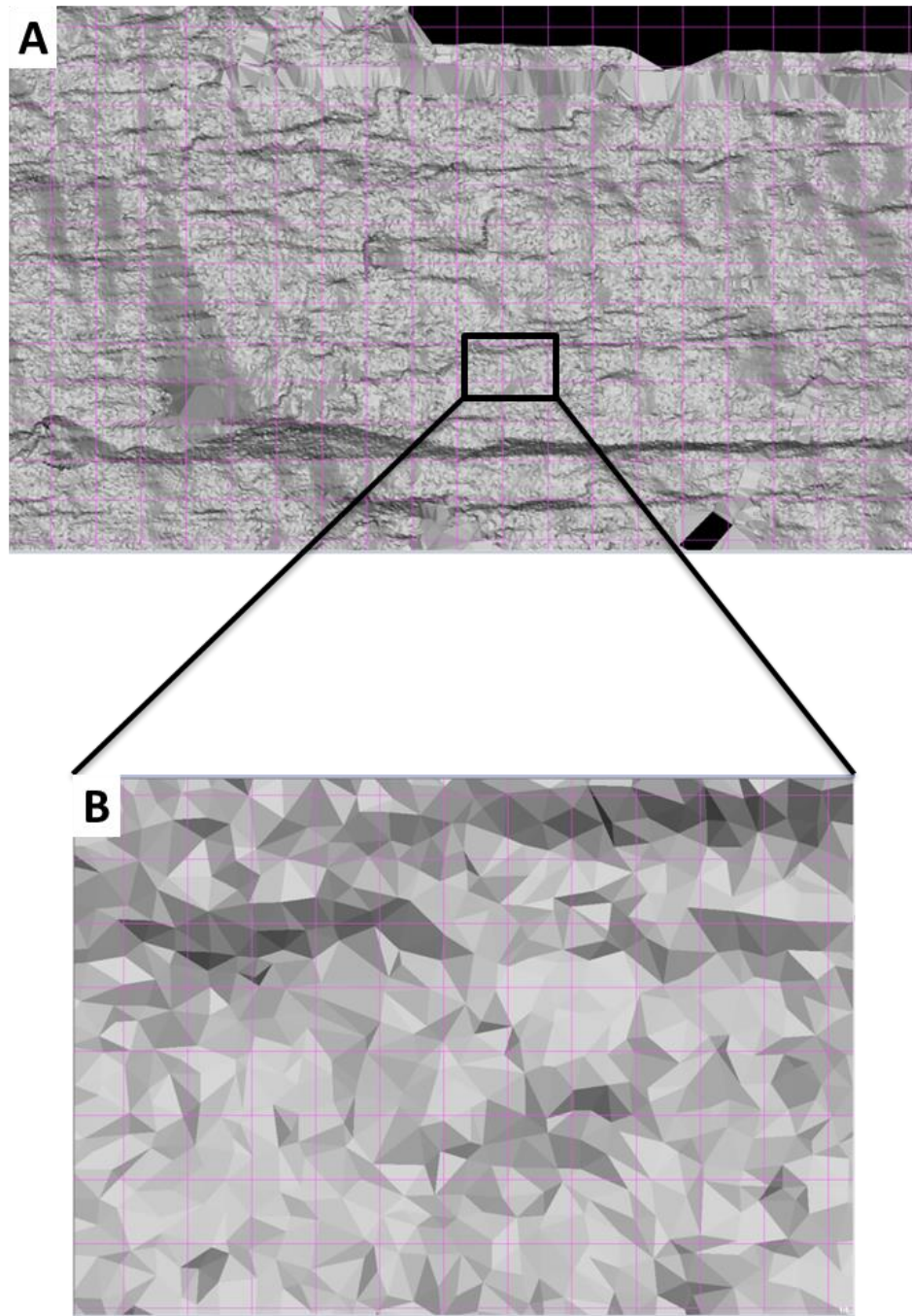


Figure 5.9 Triangulation process; A: starting the interpolation for the previously selected part; B: the triangulated model for the same part; C: zoom in to the triangulated part, note the holes which appear in this part



**Figure 5.10 A: the triangulated part of the model; B: zoom in to the rectangular part in A and it shows the triangles created by the interpolation process**

Then, the same steps are repeated for the rest of the first point cloud file from the first scan until the whole point cloud data from the first scan position will have been triangulated and decimated (Figure 5.11).

The triangulated model resulting from the first scan position contains some holes and empty areas, this can be solved by importing the other three scan files and integrate them with the first one. The same steps were implemented for each of the three other scan files and all have been used to produce one final model. This model has overlaps between four point clouds data, so next reducing of the overlapping should be implemented for the whole model (Figure 5.12). It is clear from the final triangulated model how the combination of the four scan files into one has led to the filling of the gaps that appear in each one separately (Figure 5.13).

Now, the final triangulated model merged everything together using the IMMerge tool within the polyworks tool box. Also, to enable the editing and enhancing of the model, we import it to the IMEdit tool (Figure 5.14). The model shows some small holes still remaining after the merging which can be filled either manually or automatically by the “click and fill” option (Figure 5.15). After that, the final polygonal model is extracted from the IMEdit tool as object file (.obj extension) (Figure 5.16A). The photos of the target outcrop have been selected and ordered in sequence panorama and by using draping software (Draping scanner-mounted Riegl photos provided by Geological and Historical Virtual Models LLC,(GHVM)) they were superimposed on the polygonal model (Figure 5.16B). Finally, the draped polygonal model is imported to the IMEdit tool again to visualize it from different angles of view and to make sure the model is ready for the interpretation (Figure 5.17).



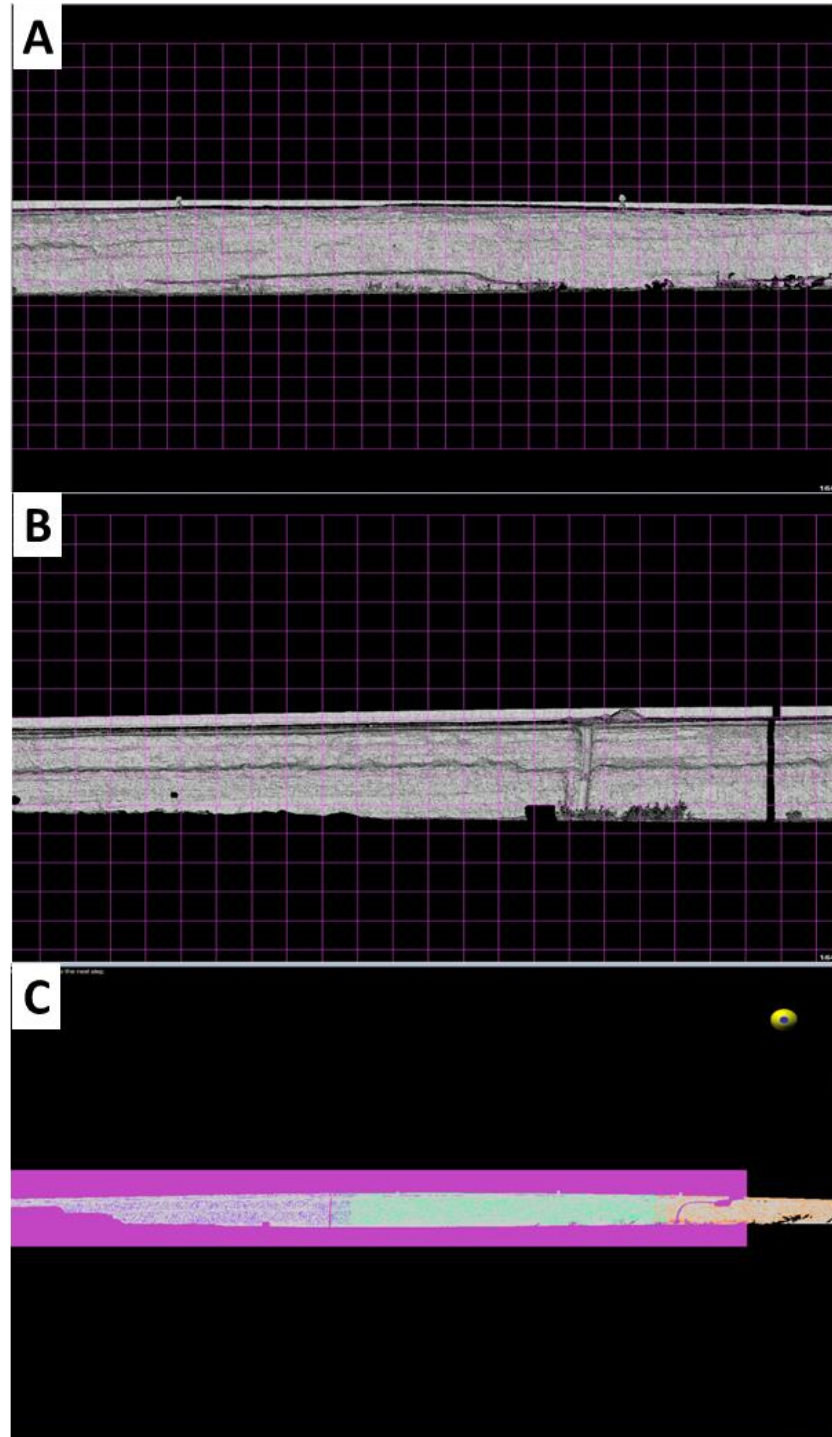


**Figure 5.11** A and B: triangulation for the second and the third parts of the same first point cloud file; C: the final triangulated model after combining the whole triangulated parts of the file



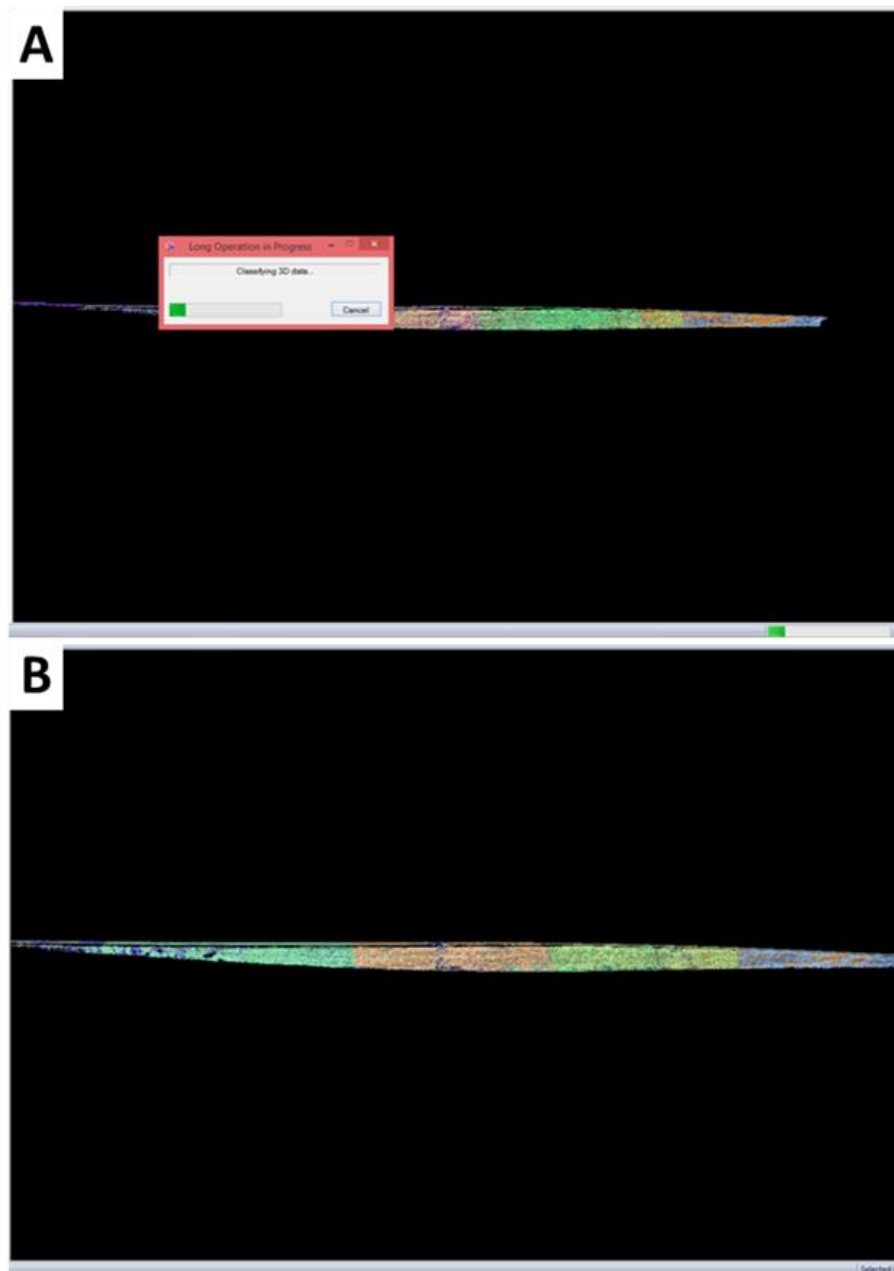


**Figure 5.12 A: reduce the overlapping between the four triangulated scan files; B: display of the whole triangulated model**

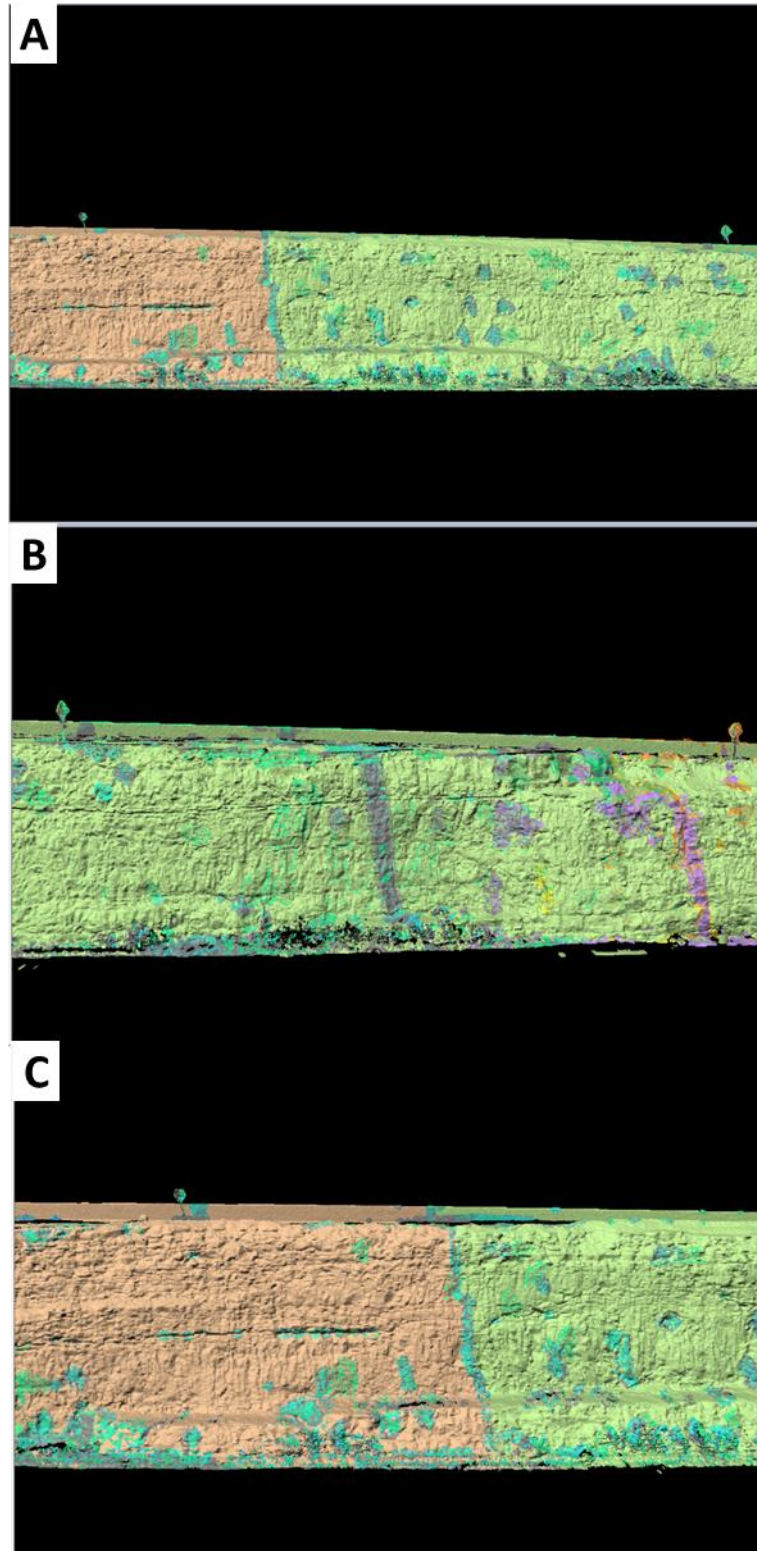


**Figure 5.13 A, B and C: different views for the triangulated model showing how integrating between the four scans assist to fill in the gaps between them**

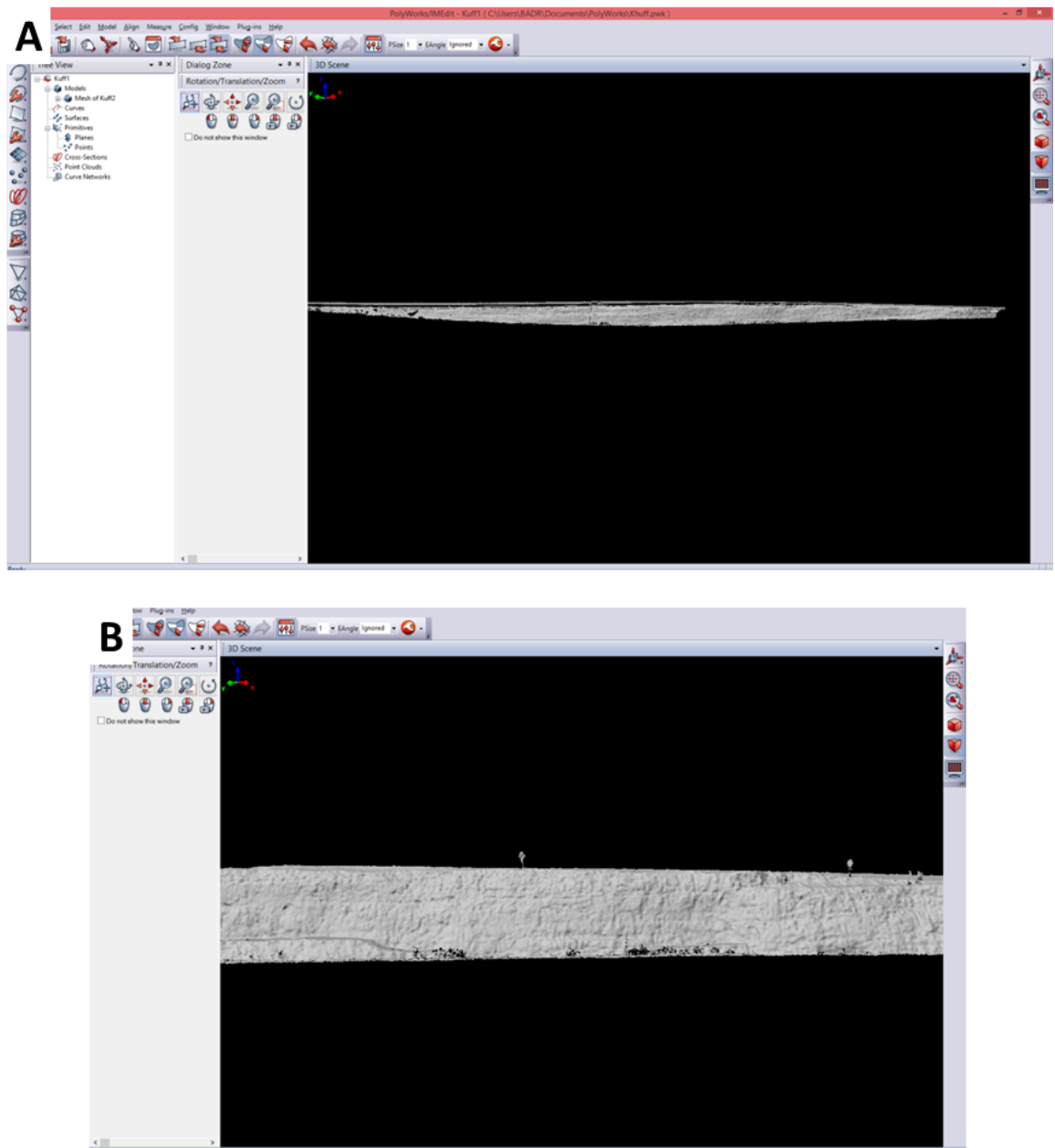


**Figure 5.14** IMEdit interface; A: visualize the model in IMEdit; B: zoom in to the final triangulated model in IMEdit

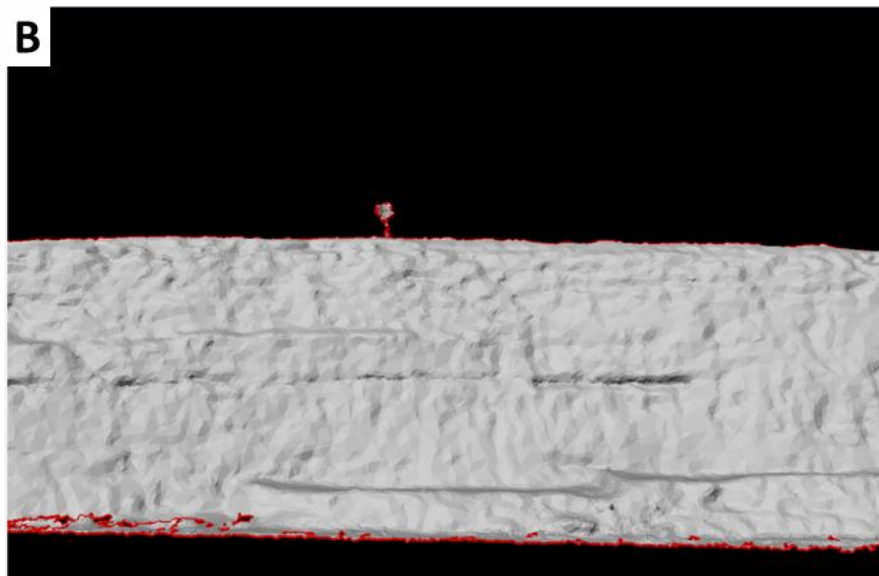
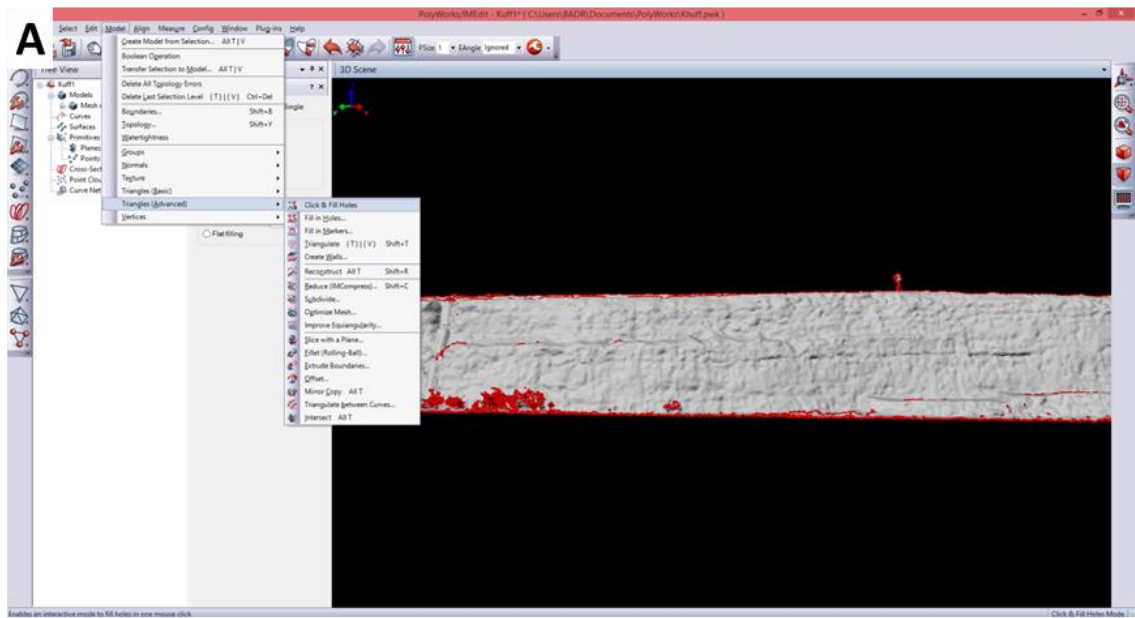


**Figure 5.15** Editing the model; A: click on and select the holes appearing in the model; B: the model after filling the holes

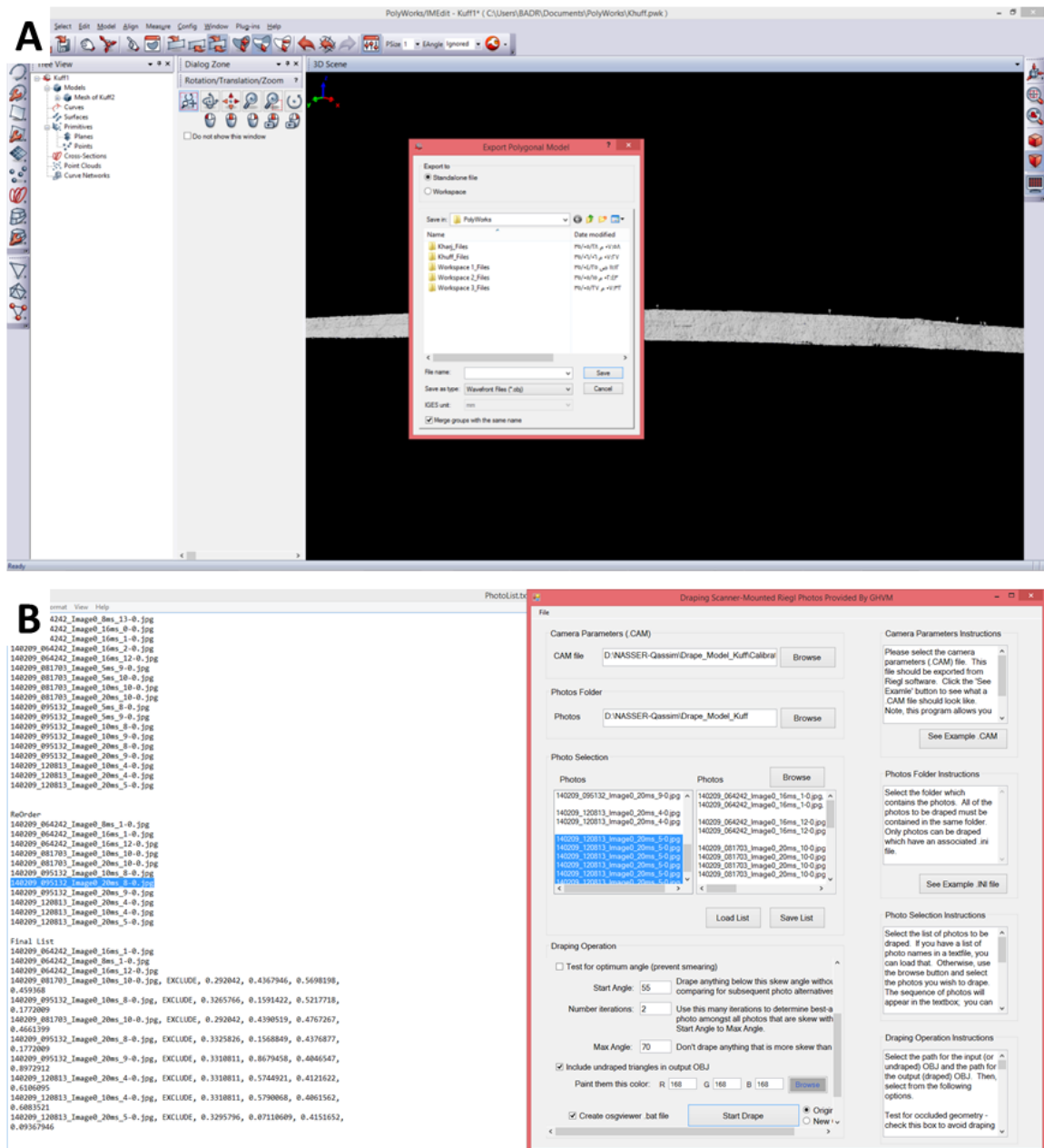


Figure 5.16 A: exporting the polygonal model as object file; B: the draping software used to superimpose the photos of the outcrop on the model



**Figure 5.17** Part of the final draped polygonal model displayed in IMEdit tool

## **5.5 Interpretation of the Digital Model**

The steps for the interpretation of the photorealistic model can be summarized in (Figure 5.18). The digital model (the draped polygonal model) is now ready for the interpretation and integration with the traditional geological data from the field. This step is done by using ArcGIS software and its toolbox. The first step is to create the geological database that the ArcGIS can deal with because it cannot use the front wave object file .obj directly. When the files were ready, the model was imported to the ArcScene tool to start the interpretation (Figure 5.19). The normal ArcScene provides the appropriate environment for visualizing the outcrop and doing some geostatistics on it but it cannot do the integration between the digital model and the traditional sedimentological and stratigraphical results from the field. In order to solve this issue, an extra tool provided by GHVM, called Geo Analysis Tool (GAT) was installed and added to the options available in ArcScene.

The first step in the interpretation is making and tracing the bed surfaces according to the data from the field. The tracing starts by picking points along the surface continuously from the beginning to the end of the bed (Figure 5.20). When all points along the single horizon are picked then the trace will be drawn and saved in a new shape file in the ArcScene and the rest of the traces will be saved in the same file. In each bed surface two lines were drawn, the first is following the picked points (original points line) and the second follows the protrusions and projections along the bed (projected line) (Figure 5.21).

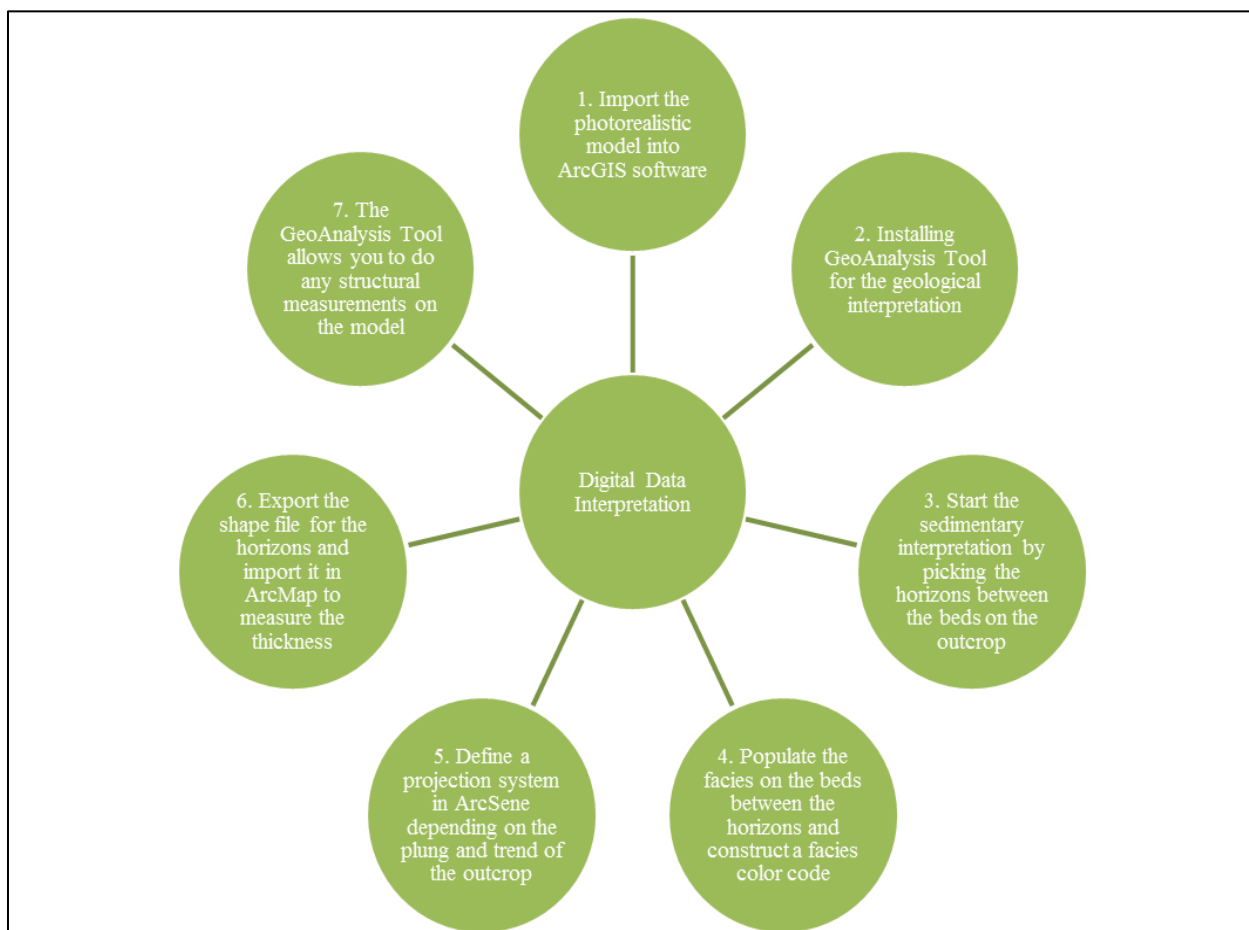


**Figure 5.18 Summary of the workflow for the interpretation of the digital data**



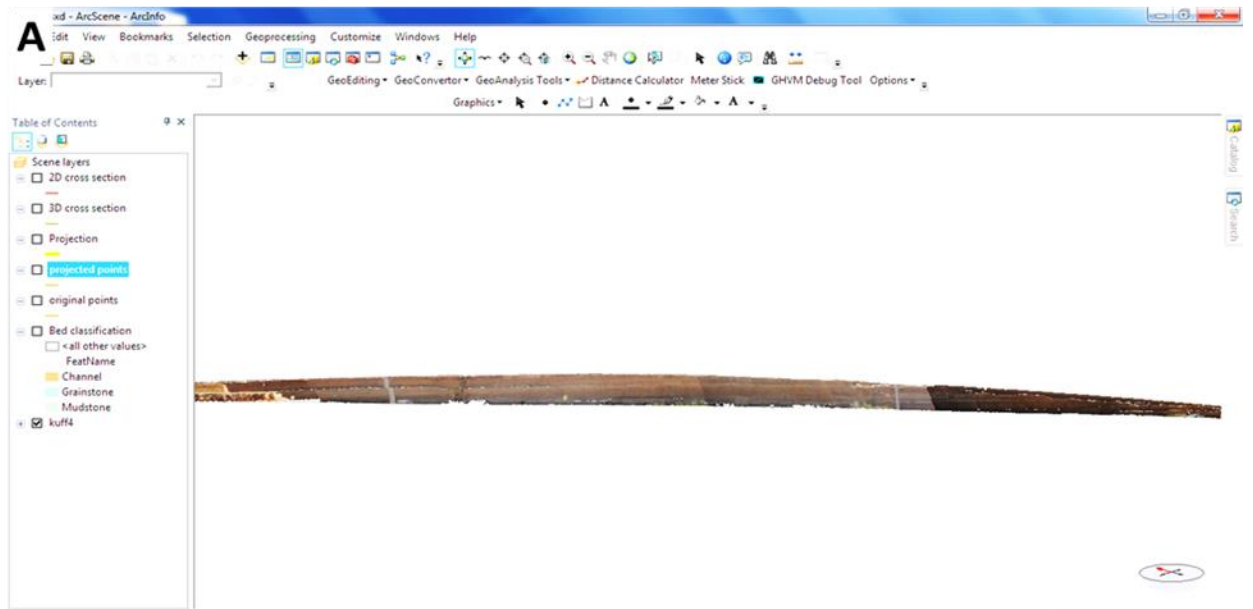


**Figure 5.19 Importing the draped polygonal model to ArcGIS; A: the interface of ArcScene tool with the model displayed on it; B and C: zoom in to the model in ArcScene**

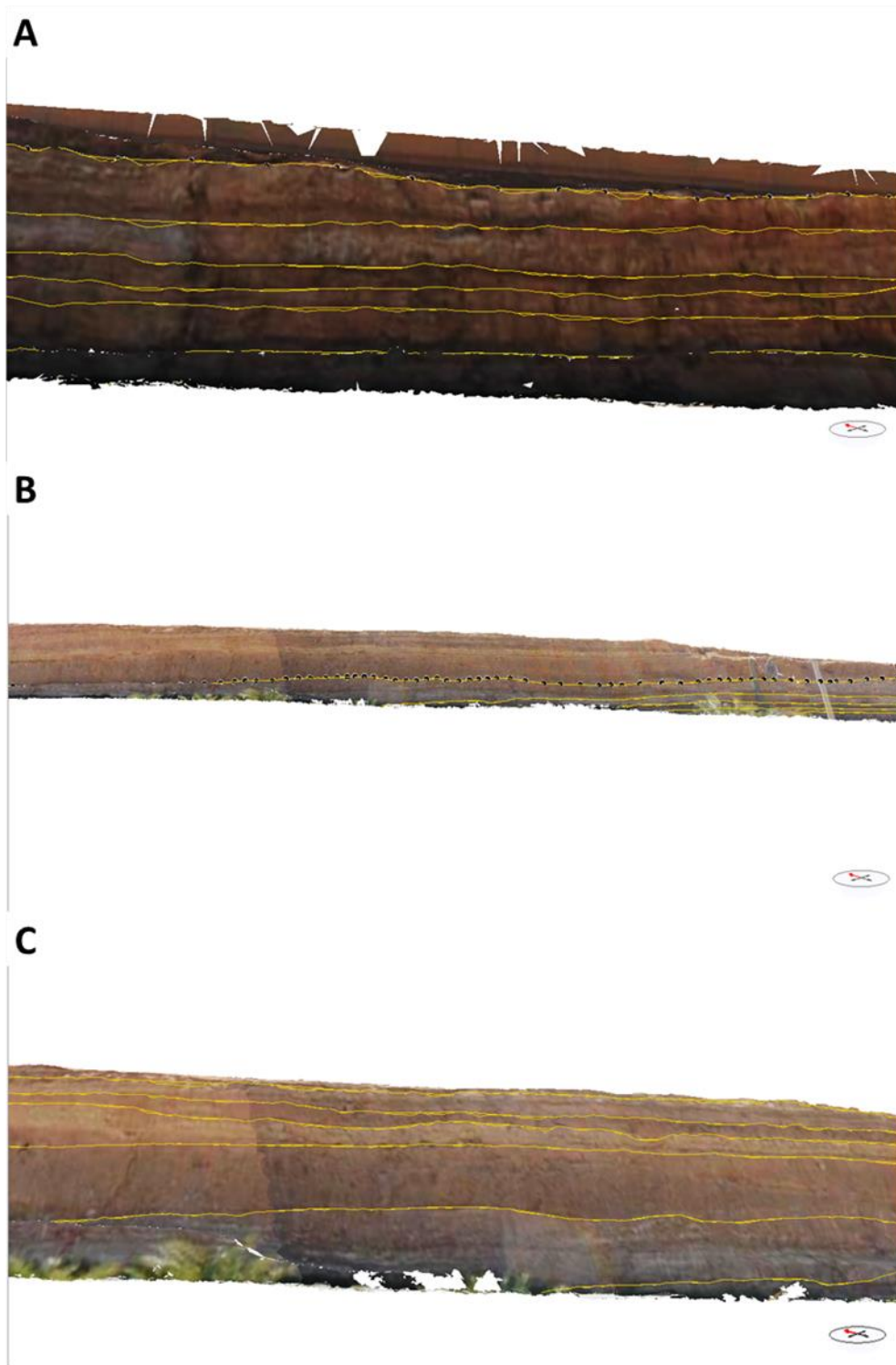


**Figure 5.20 Bed surfaces delineation; A and B: the black dots point to the tracing of the surface from the beginning to the end of the bed; C: The top and bottom horizons for each bed have been traced laterally and drawn**

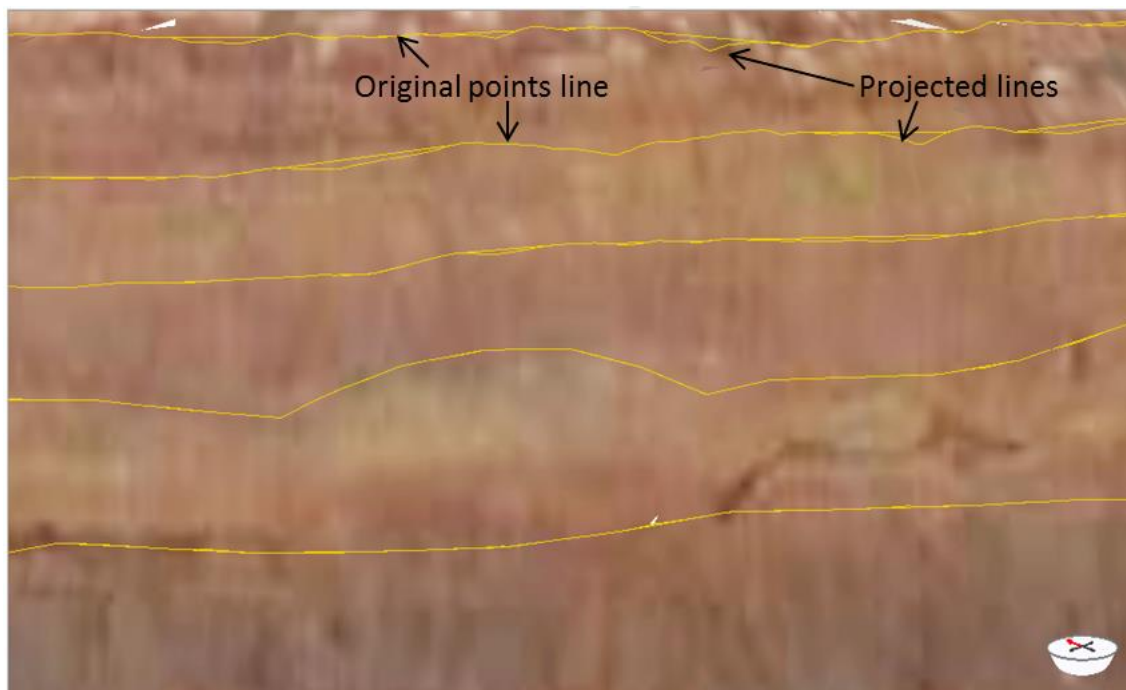


**Figure 5.21** The projected lines and the original point's line displayed clearly in this part of the model

When the top and bottom for every bed in the outcrop are traced and drawn, the model will be ready to populate the facies on it. Based on the geological data from the field and the laboratory, the facies for every bed will be superimposed on the model and marked with a specific color. The first step is to select the traces that correspond to the top and bottom horizons for each bed (Figure 5.22). After selecting the top and bottom horizons of the bed, the rock name and texture were assigned to it with special color characterizing it. The same procedures repeated for the rest of the beds appear on the outcrop. The final resulting model after populating the facies for all the beds is called the digital facies model (Figure 5.23). The model provides good opportunity to examine the spatial continuity of the beds from different angles of view. The model infers also the layer cake type of carbonate deposition of the Upper Khartam Member because of the good continuity of each bed on the model. The facies model was saved as a separate shape file in the ArcScene for the whole set of beds, not for each bed by itself.

The stratigraphic data also have been displayed and superimposed on the model using the same previous steps for constructing the facies model. I started by picking the surfaces between the depositional sequences and assigned the name for every surface. Then, each High Frequency Sequence (HFS) was delineated and populated between the sequence surfaces and characterized by a special color. The results after populating and coloring all the HFSs are displayed in what is called the digital stratigraphic model (Figure 5.24).

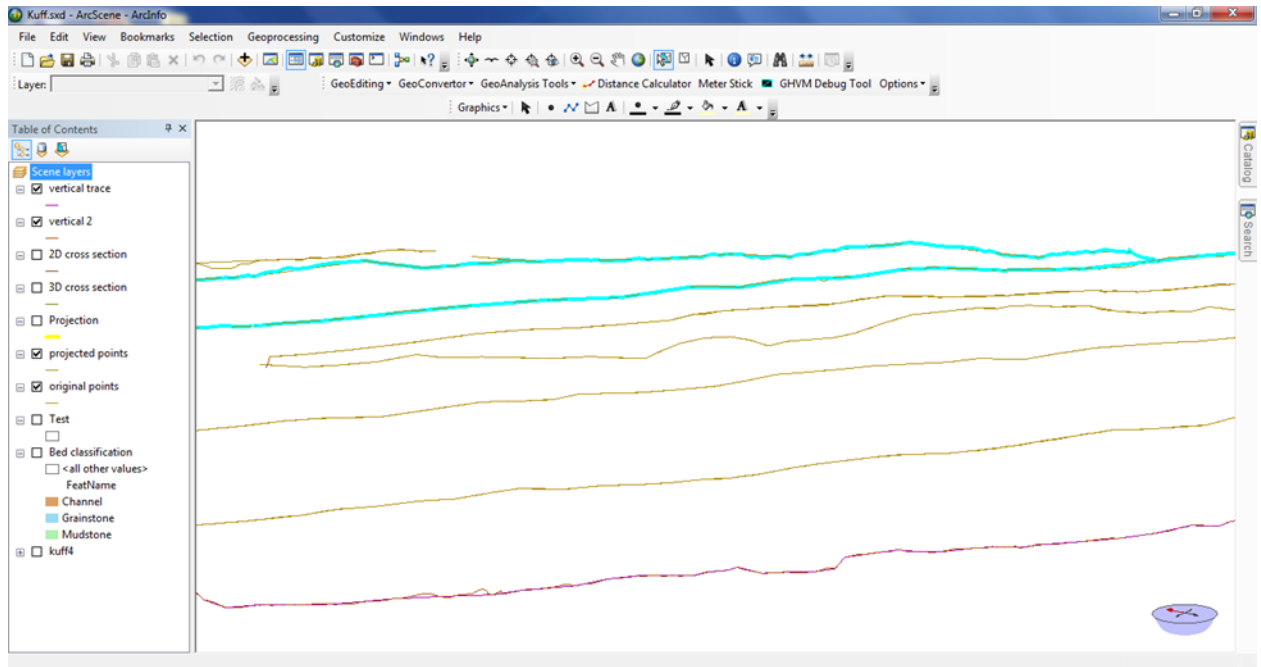


**Figure 5.22** The bed horizons on the outcrop, the highlighted aqua horizons point to the top and bottom of specific bed were selected to populate the facies code of this bed

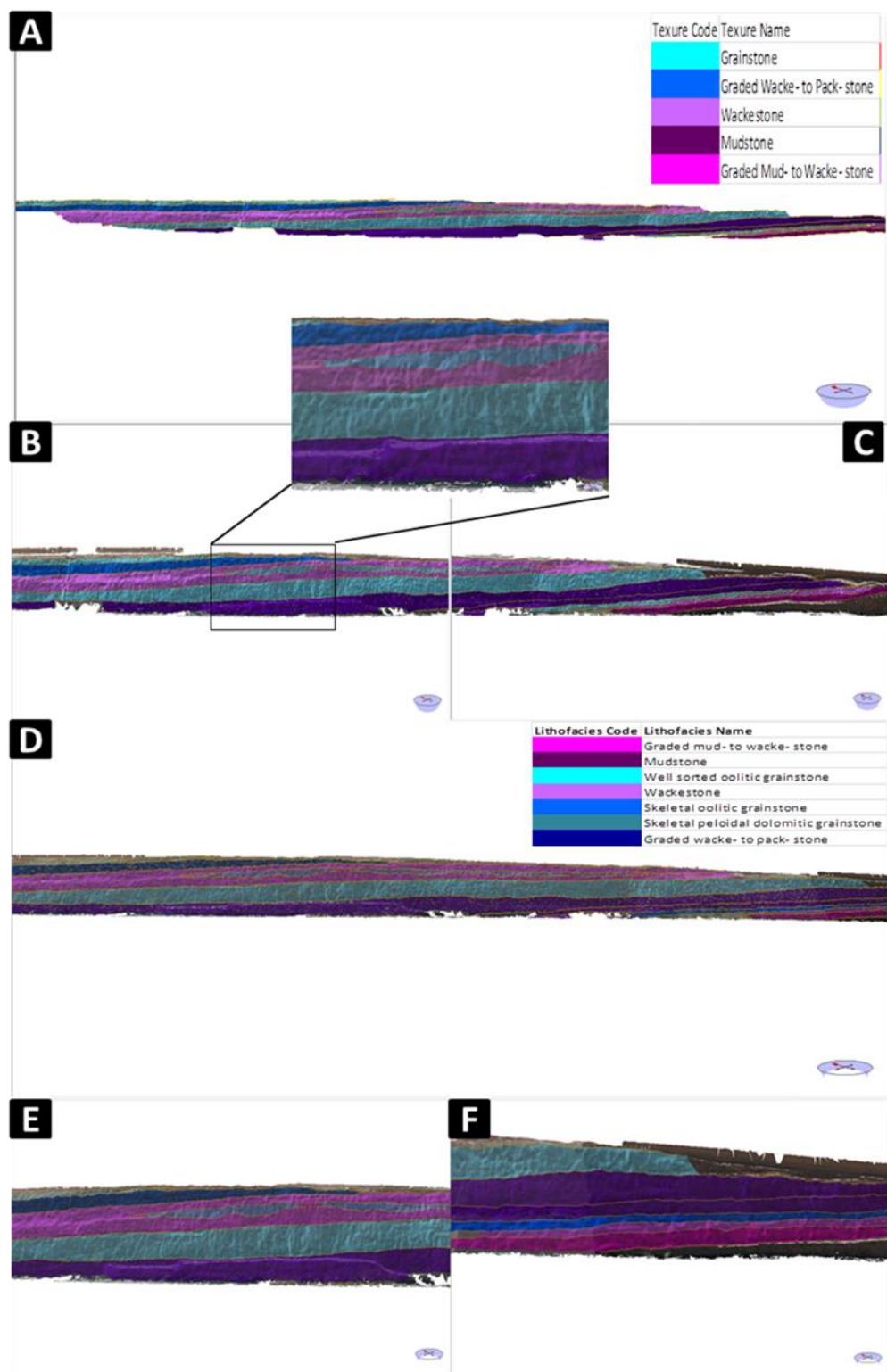


**Figure 5.23 Texture and facies digital model; A: digital model shows the texture distribution along the outcrop according to the shown legend; B and C: zoom in to the texture model using the same legend as in A; D: the lithofacies distribution along the outcrop according to the attached legend; E and F: zoom in to the same lithofacies model using the same legend as in D**

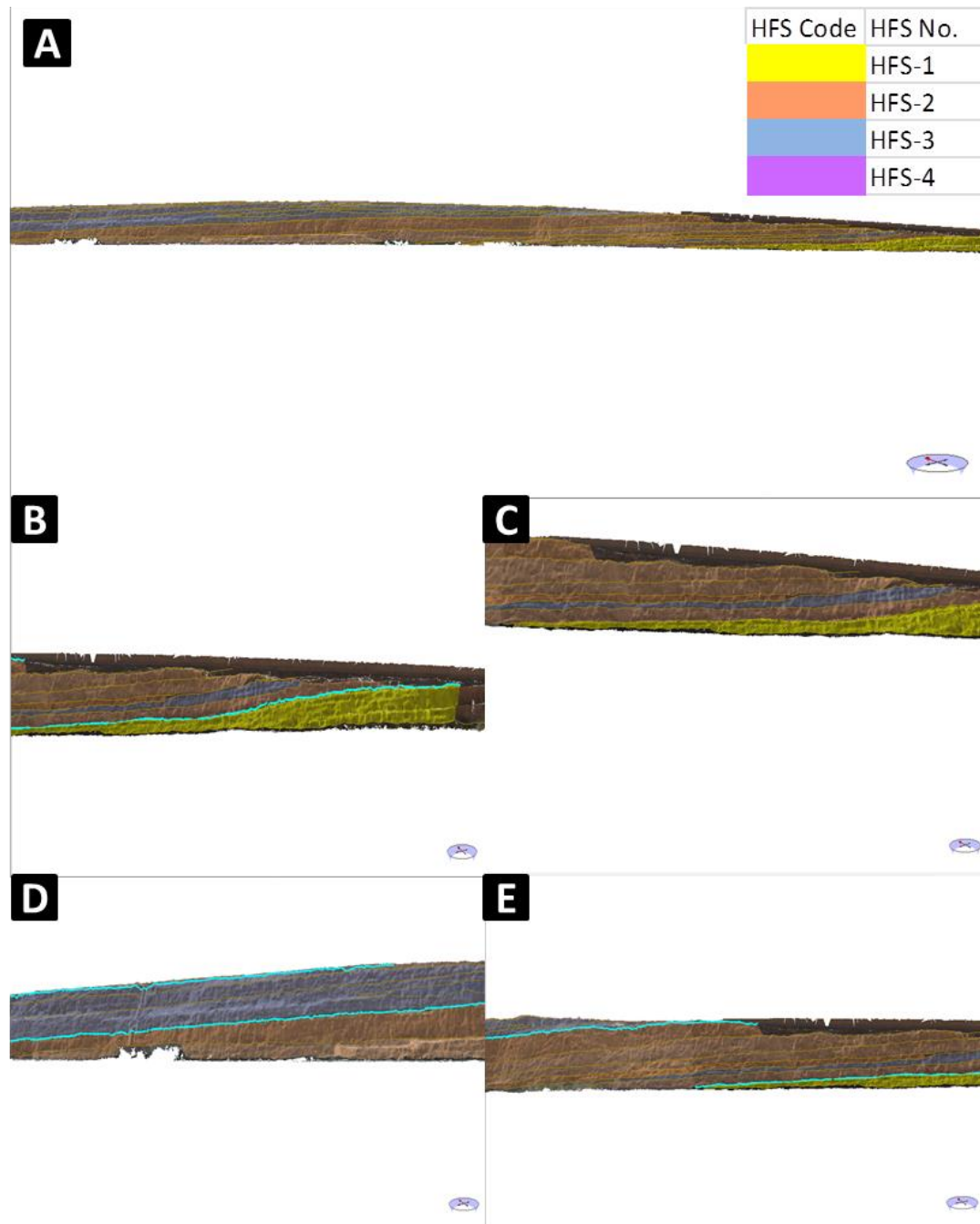


**Figure 5.24 The stratigraphic digital model; A: stratigraphy showing the depositional sequences and their surfaces according to the legend; B, C, D and E: show the same stratigraphy model but from different angle of views using the same legend and the highlighted surfaces are the sequences surfaces**

Some measurements can also be done on the model. The first step is to define the axial projection system within the coordinate system of the model. The model oriented according to the best fit with real orientation of the outcrop in the field and the dipping of it. The outcrop of Upper Khartam here is oriented East – West and because it is a road cut it tilted in the western part. Because of this tilting of the outcrop two projections systems were created (Figure 5.25). The purpose of creating the projection systems is to extract the traces or the horizons of the beds on a separate plane from the model. For each projection system the software automatically calculates the trend and plunge degrees and they can also be imported manually. The trend degree depends on the orientation of the model when the automatic calculation took place and the plunge was set to  $0^{\circ}$  because the outcrop is a road cut and assumed to have no plunge. The trend values for the two projection systems were  $40.1^{\circ}$  and  $49^{\circ}$  for the eastern and the western one respectively. Also, each system has its own origin point calculated automatically and displayed. The lengths of the x, y and z axis controllable and can be viewed from different angles. The second step is to divide the traces into two groups following the orientation and the tilting of the outcrop and coinciding with the two projection systems created previously (Figure 5.26). Then, the traces are extracted to 2D shape file and saved and imported to ArcMap tool to do the thickness measurements (Figure 5.27). In ArcMap, the measurement of the thickness is done bed by bed by selecting the two traces (top and bottom) of the bed. The measurement tool provides reading for the thickness laterally with a spacing of 2 cm between each measurement and the other. So, it gave tens of measurements for each bed from the beginning of the bed to the end of it (Figure 5.28).





**Figure 5.25** The digital model displayed in ArcScene and the yellow axis are the two axial projection systems used to extract the traces

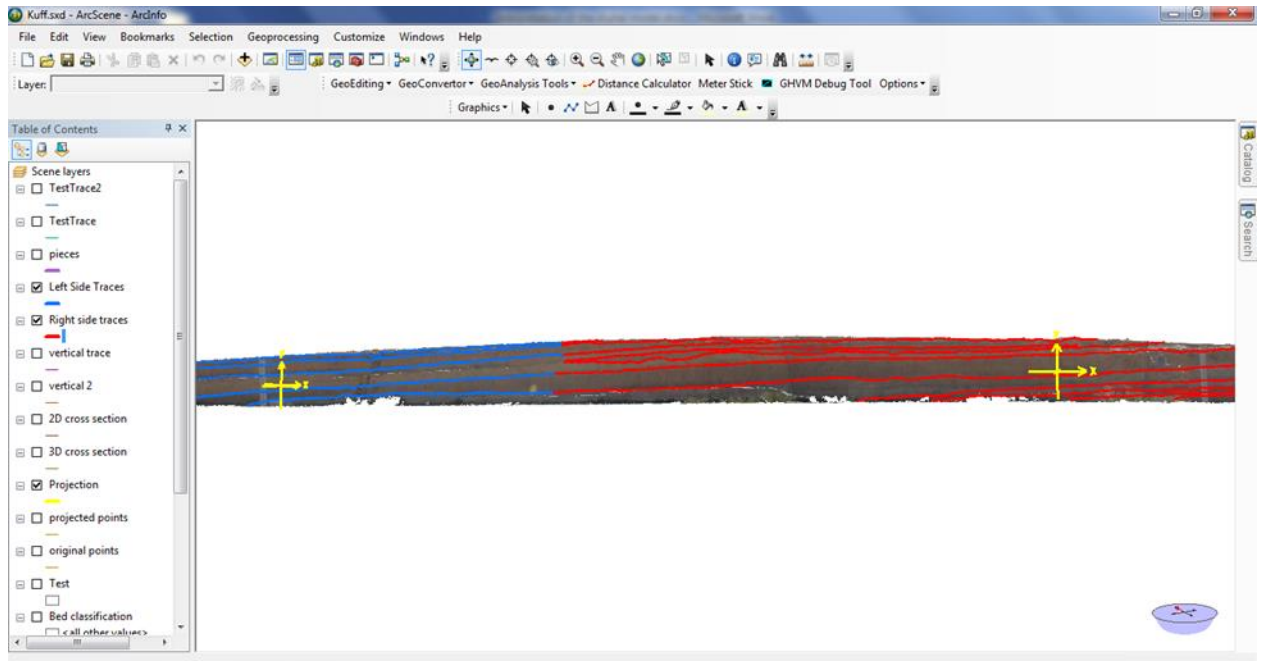


**Figure 5.26** The two groups of traces are colored by red and blue, the axial projection systems are illustrated in yellow

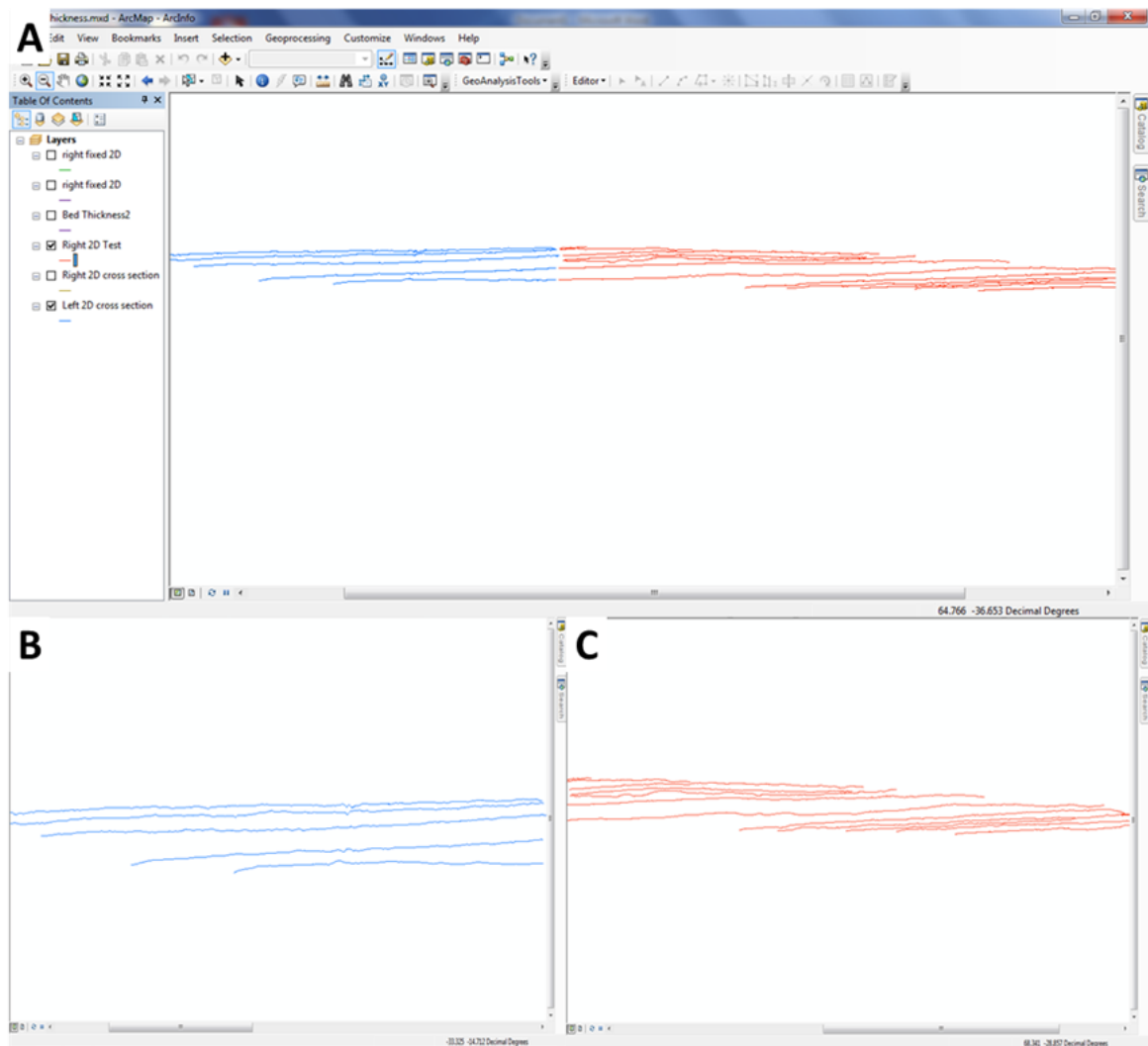


**Figure 5.27** The extracted traces from the model; A: ArcMap interface display of the imported shape file for the whole traces from the model; B: zoom in to the western blue traces; C: zoom in to the eastern red traces

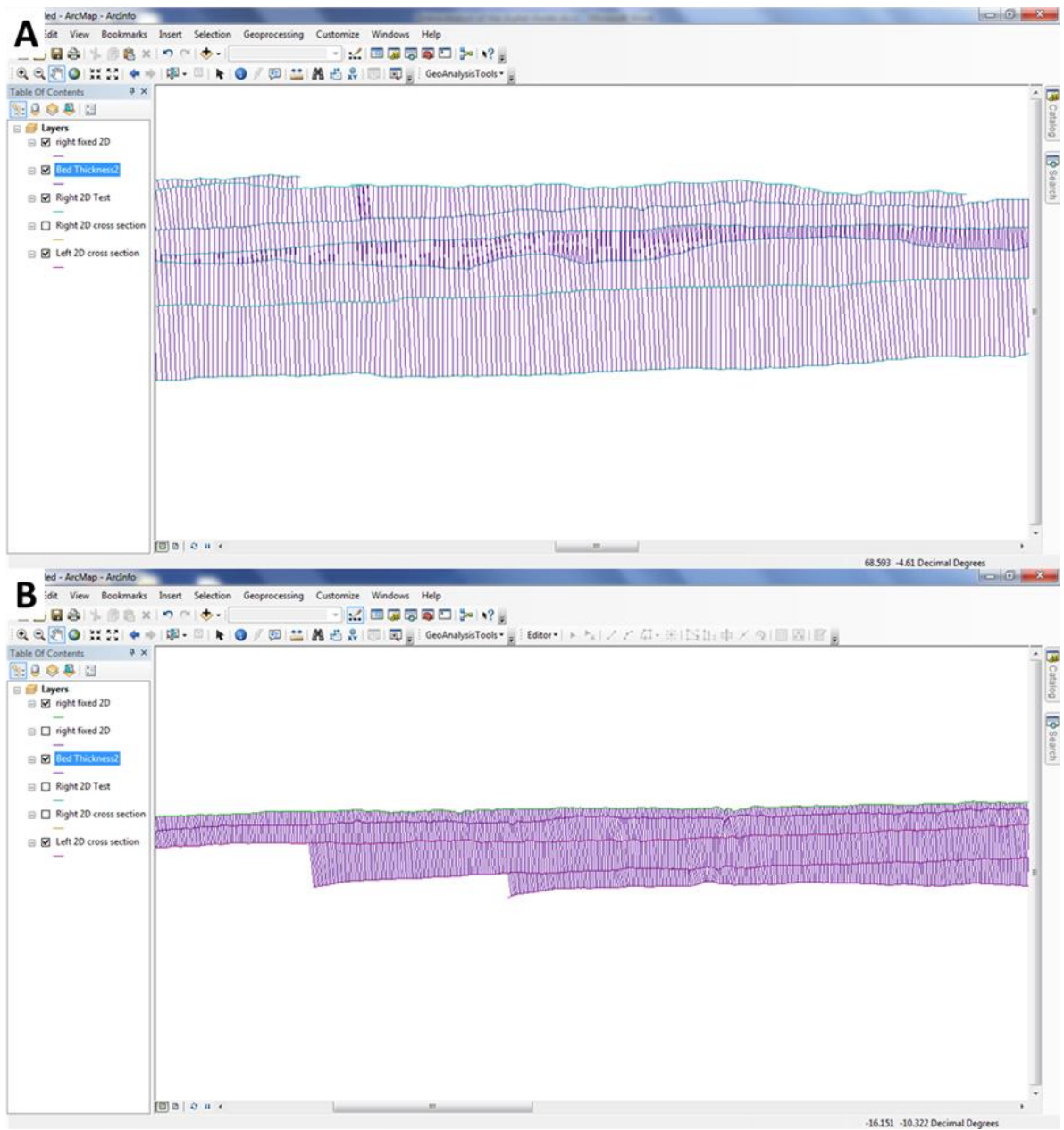


**Figure 5.28 Bed thickness measurements; A: the thickness measurements along the eastern part of the outcrop; B: the thickness measurements along the western part of the outcrop**

Then, the average thicknesses were calculated for all the beds and compared with the thicknesses from the field to validate the ArcMap measurements (Table 5.1).

The workflow from the acquisition to the interpretation of the digital model can be summarized in (Figure 5.29).

**Table 5.1 Average thickness for every bed from the field and from the ArcMap software.**

<b>Lithofacies</b>	<b>Thickness (m) from field</b>	<b>Thickness (m) from ArcMap</b>
Mudstone	2	1.8794
Grainstone lens	0.6	0.5442
Graded mud- to wacke- stone	3	3.1079
Well sorted thick oolitic grainstone	3	2.6435
Wackestone	0.7	0.6989
Skeletal oolitic grainstone	0.6	0.7266
Graded wacke- to pack- stone	1.5	1.6750
Skeletal peloidal dolomitic grainstone	1.0	0.9897

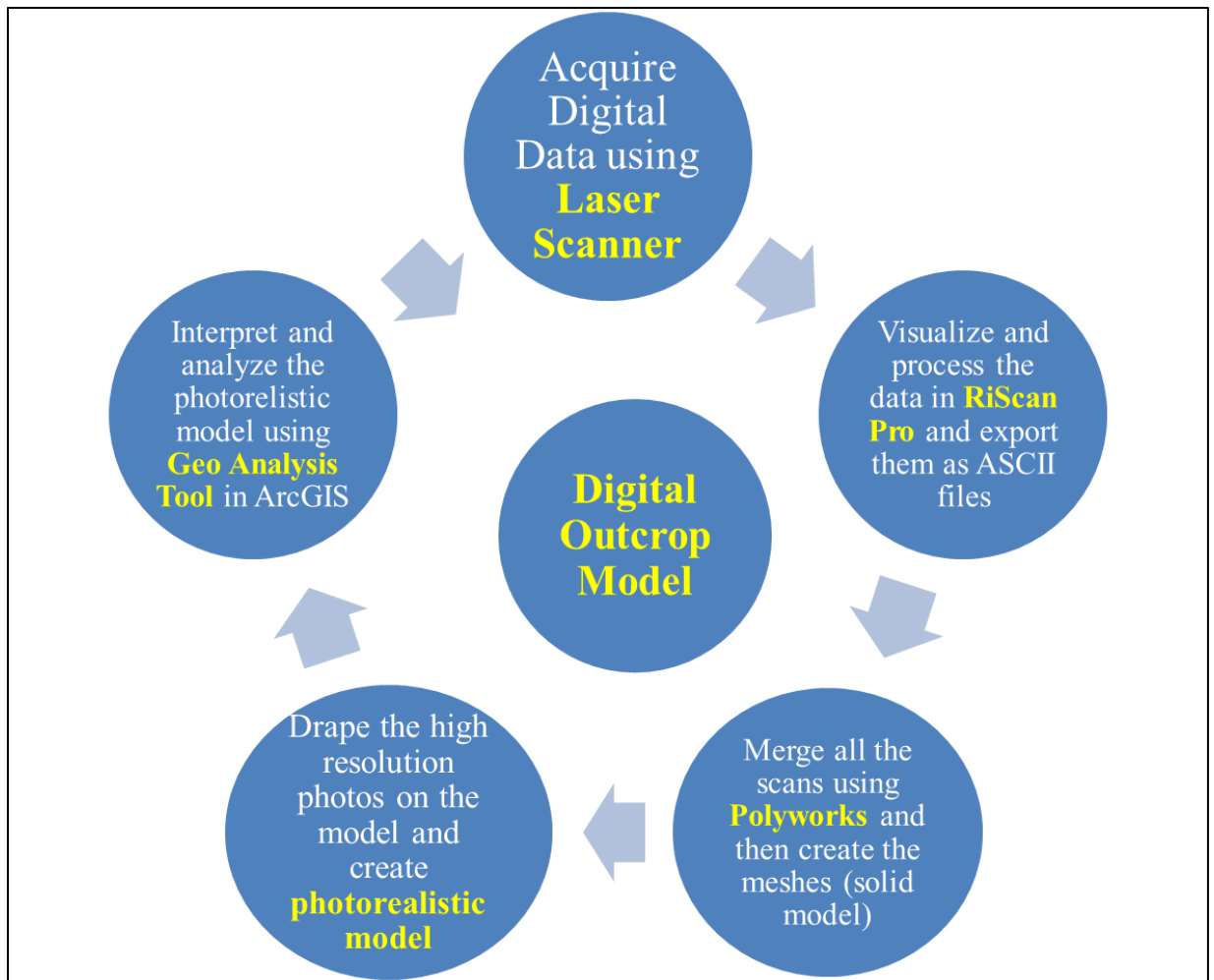


**Figure 5.29 Summary of the workflow from the acquisition of the digital data to the build and interpretation of the photorealistic model**

## 5.6 Interpretation and Discussion

The using of LiDAR for the digital modeling for part of the Upper Khartam Member revealed the benefits that might be very useful for the geologists. The digital model gives the opportunity to integrate a large amount of data in one model. In the present study the integration of the sedimentology and stratigraphy along with some statistical parameters has been perfectly done and the results were good. The LiDAR is very useful for the collection of geological data and it can really bring the outcrop with real dimensions, colors, high resolution and vertical and lateral continuity to your office.

The main differences between the LiDAR and the high resolution external camera can be summarized as follows:

- The LiDAR gives a high resolution colored model without distortion in the images like what happens in the digital camera.
- LiDAR instruments can give a high resolution model from large distances up to 4 km but for the normal digital camera the resolution decreases with the increasing of the distance.
- In the digital modeling the model will be geo-referenced to the global coordinate system and this option is absent for the digital camera.
- The 3D option for the outcrop modeling is available by using LiDAR but not for the digital camera. The final product of the 3D model is a photorealistic model that provides a good environment to interpret the model in a 3D sense.



- The projections and protrusions that appear in the outcrop face can be precisely delineated in the digital model which is impossible from the normal digital photograph.
- The delineation of the horizons between the beds and the population of the lithofacies or depositional sequences on the digital LiDAR model can be done more easily and with higher precision than in the normal digital model.
- The structural measurements such as; strike, dip, plunge and others can be perfectly estimated from the digital LiDAR model but cannot even be approximated from the normal digital photos.
- The statistical parameters can be calculated with high confidence from the digital LiDAR model while these calculations are quite difficult from the normal digital photo.
- The digital model provides the chance to precisely estimate the thickness of the beds continuously from the beginning to the end of the bed which is not accurate in the normal digital photo.

From the comparison between the digital model constructed by using LiDAR and the normal digital photo from camera, it is clear that the LiDAR is a very useful tool for geology in different approaches. There is a comparison in this study between the measurements of the thickness of the beds from the field and from the model and the results were highly correlatable with negligible differences. This might also support the utilizing of LiDAR to save time in measuring the bed thicknesses in the field.

## CHAPTER 6

# RESERVOIR HETEROGENEITY AND QUALITY

### 6.1 Introduction

The carbonate reservoirs reflect intrinsic heterogeneities in different scales from micro- to giga- scale which make them challenging (Pranter et al., 2006; Fitch et al., 2013). These heterogeneities might be depositional or diagenetic and are caused by several factors such as; lithology, lithofacies, depositional environment, mineralogy, pore type and diagenesis. The typical datasets from subsurface are generally not sufficient to characterize the variations in the petrophysical properties and the lithofacies and hence the reservoir heterogeneity (Pranter et al., 2006). The Khuff-A reservoir in the subsurface which is equivalent to the Upper Khartam Member outcrop is known for its complex vertical and lateral sub-seismic heterogeneity (Janson et al., 2013; Osman et al, 2014b). These small scale heterogeneities can be determined and evaluated by using equivalent strata from the outcrop of Upper Khartam.

The techniques that measure the heterogeneity are geostatistical techniques and therefore they provide a single value for the heterogeneity in a dataset. These techniques are the homogeneity index, Lorenz coefficient and the Dykstra – Parsons coefficient. Here, the focus is on the Lorenz coefficient and a modified version of it (Fitch et al., 2013; Adam et al., 2014). There are some basic measures used to study the reservoir quality, such as:

Reservoir Quality Index (RQI), pore volume to grain volume ratio ( $\Phi_z$ ,  $\text{PHI}_z$ ) and the Flow Zone Indicator (FZI) (Amaefule et al., 1993).

In this study, from the same selected outcrop for the digital modelling three potential reservoir units were selected for detailed description of their heterogeneity and quality. These units are given the names A, B and C from the bottom to the top. The units are deposited above each other, unit A is at the bottom and unit C is at the top. The selection of these units depended on several factors: the intervals that contain grainstone texture associated with higher porosity and permeability from the vertical sections have been investigated in the same outcrop, the good correlation between the vertical sections, the good lateral continuity of these units along the whole outcrop and the spatial occurrence of the units.

After the selection of these units I made a detailed description and sampling of them laterally. The horizontal sampling was made with 5 m spacing between samples for the reservoir units A and B, and with 2.5 m spacing for unit C. The difference in the spacing was made just to see the effect of resolution. Core plugs were made for all samples collected from these units I measured the porosity and permeability values for all of them. The porosity was measured using the saturation method while the liquid permeability was measured from Gas permeability with the verification of Klinkenberg effect using TKA – 209 Permeameter using air and helium as the flowing gases. Representative samples according to different zones of porosity and permeability values were selected from these units. Thin sections, X-Ray Diffraction Analysis and Scanning Electron Microscopy (SEM) were performed for the same selected samples.

The three potential reservoir units were selected to assess their heterogeneity and quality and make a comparison and ranking for all of them. The basic statistics for the porosity and permeability values include; Mean (m), Maximum Value (max.), Standard Deviation (S), Minimum Value (min.), Median (M) and Variance (S<sup>2</sup>). Histograms for the porosity and permeability values were constructed to evaluate the nature of their distribution. Cross plots were made between the porosity and permeability measurements versus the sampling intervals to examine their vertical and lateral variability. Also, for each reservoir unit a cross plot of porosity vs permeability measurements were conducted to see the relation between them and a correlation coefficient was calculated. Then, the previously mentioned parameters; RQI,  $\Phi_z$  and FZI were also calculated using the following equations:

$$RQI = 0.0314 \times \sqrt{\frac{k}{\Phi_e}}$$

$$\Phi_z = \frac{\Phi_e}{(1 - \Phi_e)}$$

$$FZI = \frac{RQI}{\Phi_z}$$

Where; k is permeability and  $\Phi_e$  is the effective porosity.

After that, cross plots of RQI vs  $\Phi_z$  were constructed and then their correlation coefficients extracted. These coefficients were used to evaluate the heterogeneity of each reservoir unit according to the following proposed key (Table 6.1):

**Table 6.1 The key used to evaluate the reservoir heterogeneity**

<b>Correlation Coefficient</b>	<b>Heterogeneity Evaluation</b>
1.0 – 0.85	Extremely Homogeneous
0.85 – 0.60	Very Homogenous
0.60 – 0.45	Moderately Homogeneous
0.45 – 0.30	Moderately Heterogeneous
0.30 – 0.15	Very Heterogeneous
< 0.15	Extremely Heterogeneous

## 6.2 Data from Reservoir Unit A

The length of this unit is 135 m and the sampling was with 5 m spacing and the total samples collected from this unit are 28 samples. The average thickness for this unit is 0.54 m. Table 6.2 shows the measurements of the statistical parameters and the heterogeneity. Figure 6.1 shows the histograms of porosity and permeability along with number of cross plots used to evaluate the lateral variability.

The average porosity in unit A is 10 % while the average permeability in the same unit is 0.4 mD. The standard deviation is 4.8 % for porosity and 0.2 mD for the permeability. The variance value reflects that the variability degree in the porosity is more than in the permeability values. From the distribution of the porosity and permeability values it is clear that the trend of the variability of them is coincident, each peak in the variability curve for the porosity corresponds to a peak in the permeability one. The variability degree is high in both of them (Figures 6.1A and 6.1B). The histograms show that both of them are slightly positively skewed but the skew is negligible and can be considered as normal distribution (Figures 6.1C and 6.1D).

The cross plot of the porosity values vs permeability values revealed a strange behavior in the carbonate reservoir which is a strictly linearly proportional relation between them with  $R^2 = 0.92$  (Figure 6.2A). The cross plot of the RQI values against the  $\Phi_z$  values in a logarithmic scale show clustering of the data in the middle in a straight line. According to this plot, no flow units can be defined (Figure 6.2B).

**Table 6.2 A: The measurements of the first reservoir unit A; B: statistical parameters of the reservoir unit A**

<b>A</b>	Sample Location (m)	Fractional $\Phi$	$\Phi$ (%)	Ka (md)	RQI	$\phi_z$	FZI
	0	0.0383	3.8270	0.2103	0.0736	0.0398	1.8498
	5	0.0691	6.9100	0.2432	0.0589	0.0742	0.7936
	10	0.0867	8.6730	0.3083	0.0592	0.0950	0.6234
	15	0.0409	4.0910	0.1432	0.0587	0.0427	1.3773
	20	0.1363	13.6340	0.4885	0.0594	0.1579	0.3765
	25	0.0719	7.1920	0.2852	0.0625	0.0775	0.8069
	30	0.1513	15.1310	0.5496	0.0598	0.1783	0.3357
	35	0.1705	17.0540	0.6673	0.0621	0.2056	0.3021
	40	0.1276	12.7620	0.4544	0.0593	0.1463	0.4050
	45	0.0703	7.0290	0.2458	0.0587	0.0756	0.7767
	50	0.1587	15.8680	0.5804	0.0601	0.1886	0.3184
	55	0.1683	16.8300	0.6283	0.0607	0.2024	0.2998
	60	0.1636	16.3580	0.6300	0.0616	0.1956	0.3151
	65	0.0757	7.5710	0.2574	0.0579	0.0819	0.7068
	70	0.0736	7.3630	0.2599	0.0590	0.0795	0.7422
	75	0.1177	11.7740	0.4361	0.0604	0.1335	0.4528
	80	0.0252	2.5190	0.0947	0.0609	0.0258	2.3560
	85	0.0559	5.5930	0.2099	0.0608	0.0592	1.0268
	90	0.0891	8.9130	0.2739	0.0550	0.0979	0.5625
	95	0.1680	16.7970	0.6214	0.0604	0.2019	0.2992
	100	0.1381	13.8120	0.5505	0.0627	0.1603	0.3912
	105	0.0912	9.1200	0.2936	0.0563	0.1004	0.5614
	110	0.0777	7.7650	0.2541	0.0568	0.0842	0.6747
	115	0.1107	11.0690	0.4292	0.0618	0.1245	0.4968
	120	0.2111	21.1140	1.1014	0.0717	0.2677	0.2679
	125	0.1323	13.2330	0.4677	0.0590	0.1525	0.3871
	130	0.0638	6.3760	0.2529	0.0625	0.0681	0.9183
	135	0.0570	5.6960	0.2290	0.0630	0.0604	1.0424

<b>B</b>	Statistical Parameters	$\Phi$ statistics	K statistics
	m	10.5026	0.3988
	S	4.8619	0.2154
	Max.	21.1140	1.1014
	M	9.0165	0.3010
	Min.	2.5190	0.0947
	S <sup>2</sup>	23.6385	0.0464

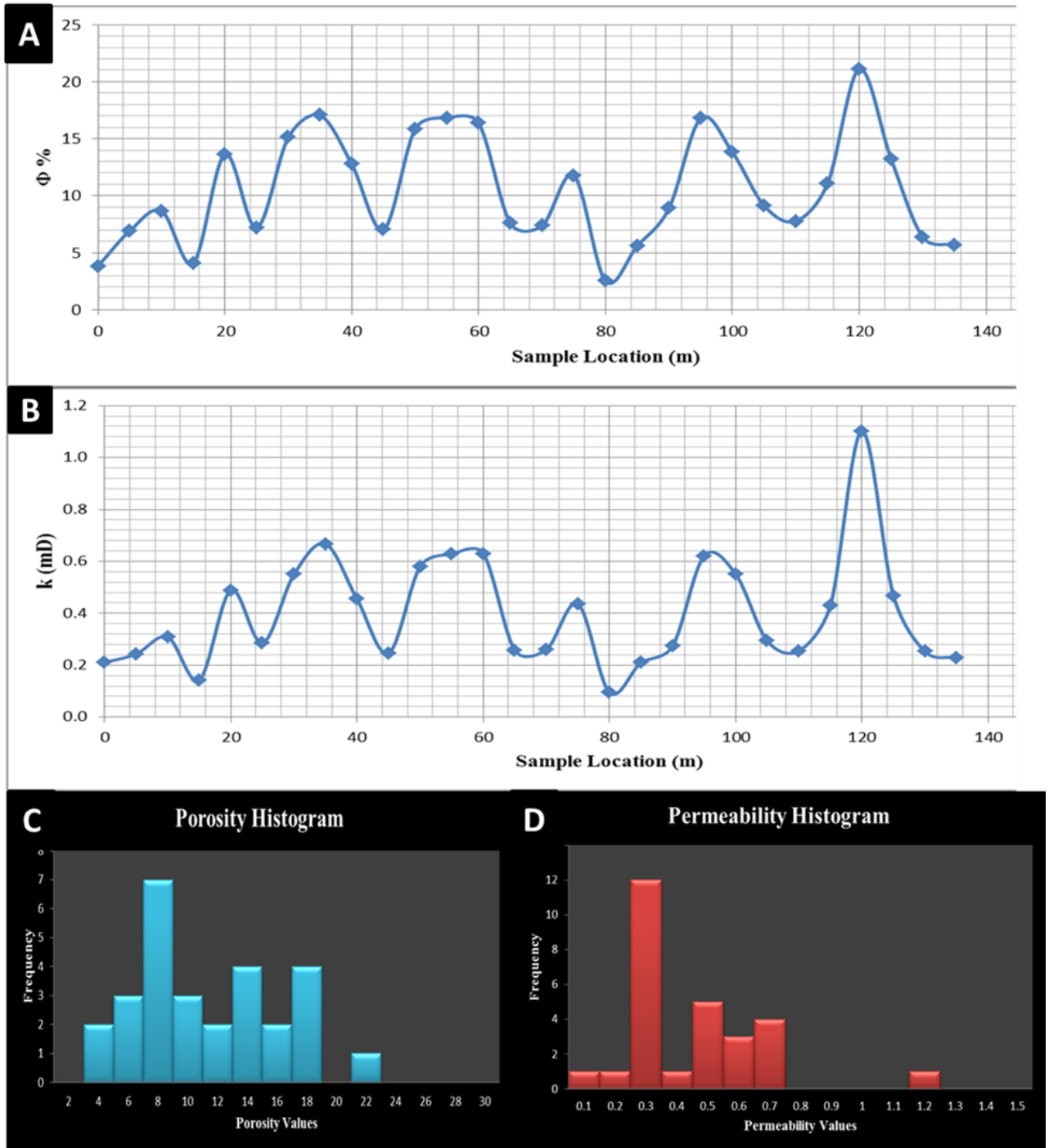


**Figure 6.1** Cross plots for unit A; A: the distribution of the porosity values along the lateral profile; B: the distribution of the permeability values along the lateral profile; C: histogram for the porosity data; D: histogram for the permeability data



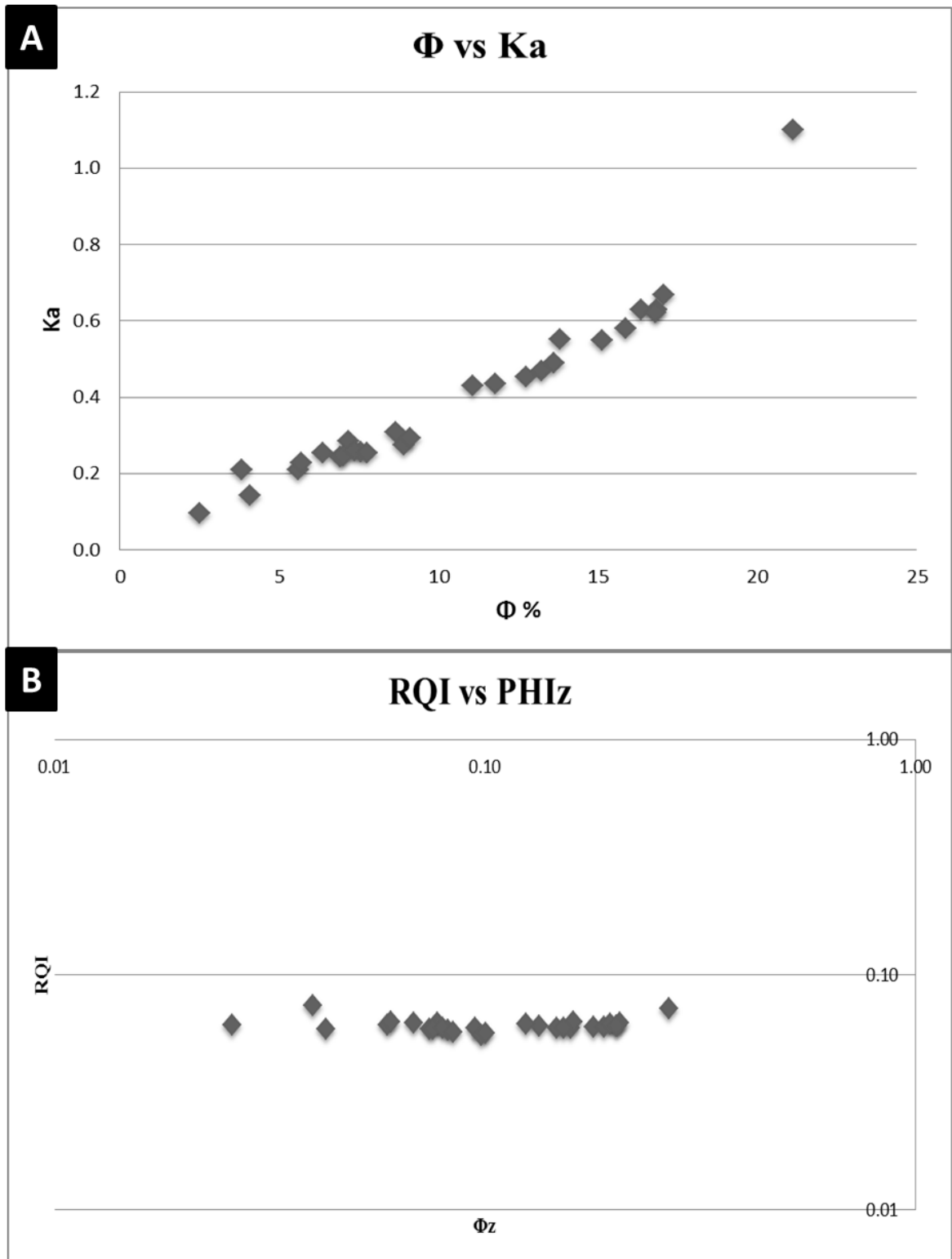


Figure 6.2 Cross plots for unit A; A: porosity vs permeability data; B: RQI vs  $\Phi_z$  data

The porosity – permeability cross plots showed that there are different relationships between them and hence different populations. Therefore, four samples were selected to represent different highs and lows in their porosity and permeability values. These samples are: A-25, A-50, A-80 and A120 where A is the reservoir name and the number refers to the sample location within the reservoir. A-25 represents the low porosity (7.2 %) and permeability (0.28 mD) zone, A-50 represents the medium porosity (15.8 %) and permeability (0.58 mD) zone, A-80 represents the very low porosity (2.5 %) and permeability (0.09 mD) zone and A-120 represents the high porosity (21 %) and permeability (1.1 mD) zone. These four samples were carefully examined by thin sections, SEM and XRD analysis (Figure 6.3).

[illegible][illegible]

144

### 6.3 Data from Reservoir Unit B

The length of this unit is 155 m and the sampling was with 5 m spacing and the total samples collected from this unit are 32 samples. The average thickness for this unit is 2.46 m. Table 2.1 shows the measurements of the statistical parameters and the heterogeneity. Figure 6.4 shows the histograms of porosity and permeability along with cross plots used to evaluate the lateral variability.

The average porosity in unit B is 26 % while the average permeability in the same unit is 4 mD. The standard deviation is 9.5 % for porosity and 14.4 mD for the permeability. The variance value reflects that the variability degree in the porosity is less than in the permeability values; this is because there are two very high permeability values of 21 and 78 mD. From the distribution of the porosity and permeability values it is clear that the trend of the variability of them is coincident, each peak in the variability curve for the porosity corresponds to a peak in the permeability one. The variability degree is high in both of them (Figures 6.4A and 6.4B). The histograms show that the porosity values are negatively skewed with two populations while the permeability values are positively skewed (Figures 6.4C and 6.4D).

The cross plot of the porosity against permeability shows some populations with high porosity and low permeability and others with high porosity and permeability with  $R^2$  about 0.3 (Figure 6.5A). The cross plot of the RQI values versus the  $\Phi_z$  values in a logarithmic scale show scattering of the data in the right and most of them are high RQI and  $\Phi_z$  values. The plot suggests several distinct flow units (Figure 6.5B).

**Table 6.3 A: The measurements of the second reservoir unit B; B: statistical parameters of the reservoir unit B**

<b>A</b>	Sample Location (m)	Fractional $\Phi$	$\phi$ (%)	Ka (md)	RQI	$\phi z$	FZI
	0	0.0638	6.3760	1.2810	0.1407	0.0681	2.0667
	5	0.0572	5.7240	0.4122	0.0843	0.0607	1.3878
	10	0.2010	20.1040	2.2956	0.1061	0.2516	0.4217
	15	0.1945	19.4545	1.6804	0.0923	0.2415	0.3821
	20	0.1881	18.8050	1.0651	0.0747	0.2316	0.3227
	25	0.1567	15.6680	0.5832	0.0606	0.1858	0.3261
	30	0.3226	32.2570	3.2061	0.0990	0.4762	0.2079
	35	0.3453	34.5255	1.8870	0.0734	0.5273	0.1392
	40	0.3679	36.7940	0.5678	0.0390	0.5821	0.0670
	45	0.3800	38.0020	0.3056	0.0282	0.6130	0.0459
	50	0.1814	18.1350	0.3760	0.0452	0.2215	0.2041
	55	0.2707	27.0680	0.5779	0.0459	0.3711	0.1236
	60	0.3600	36.0010	0.7797	0.0462	0.5625	0.0821
	65	0.2717	27.1660	3.1057	0.1062	0.3730	0.2846
	70	0.1921	19.2140	1.0636	0.0739	0.2378	0.3106
	75	0.2833	28.3340	1.2909	0.0670	0.3954	0.1695
	80	0.3745	37.4540	1.5181	0.0632	0.5988	0.1056
	85	0.3909	39.0890	78.4389	0.4448	0.6417	0.6931
	90	0.2102	21.0190	2.3965	0.1060	0.2661	0.3984
	95	0.1901	19.0080	1.1086	0.0758	0.2347	0.3231
	100	0.2158	21.5780	0.7391	0.0581	0.2752	0.2112
	105	0.3033	30.3330	2.1247	0.0831	0.4354	0.1909
	110	0.3116	31.1570	0.1785	0.0238	0.4526	0.0525
	115	0.3270	32.7010	0.1819	0.0234	0.4859	0.0482
	120	0.1369	13.6920	0.2755	0.0445	0.1586	0.2808
	125	0.3347	33.4700	29.1496	0.2930	0.5031	0.5825
	130	0.2218	22.1830	2.5333	0.1061	0.2851	0.3722
	135	0.1597	15.9690	0.3681	0.0477	0.1900	0.2509
	140	0.3872	38.7200	3.8611	0.0992	0.6319	0.1569
	145	0.3604	36.0350	1.9216	0.0725	0.5634	0.1287
	150	0.3731	37.3090	1.3104	0.0588	0.5951	0.0989
	155	0.2261	22.6100	7.0778	0.1757	0.2922	0.6013

<b>B</b>	Statistical Parameters	$\Phi$ statistics	k statistics
	m	26.1236	4.8019
	S	9.5555	14.3629
	Max.	39.0890	78.4389
	M	27.1170	1.2859
	Min.	5.7240	0.1785
	S <sup>2</sup>	91.3073	206.2934

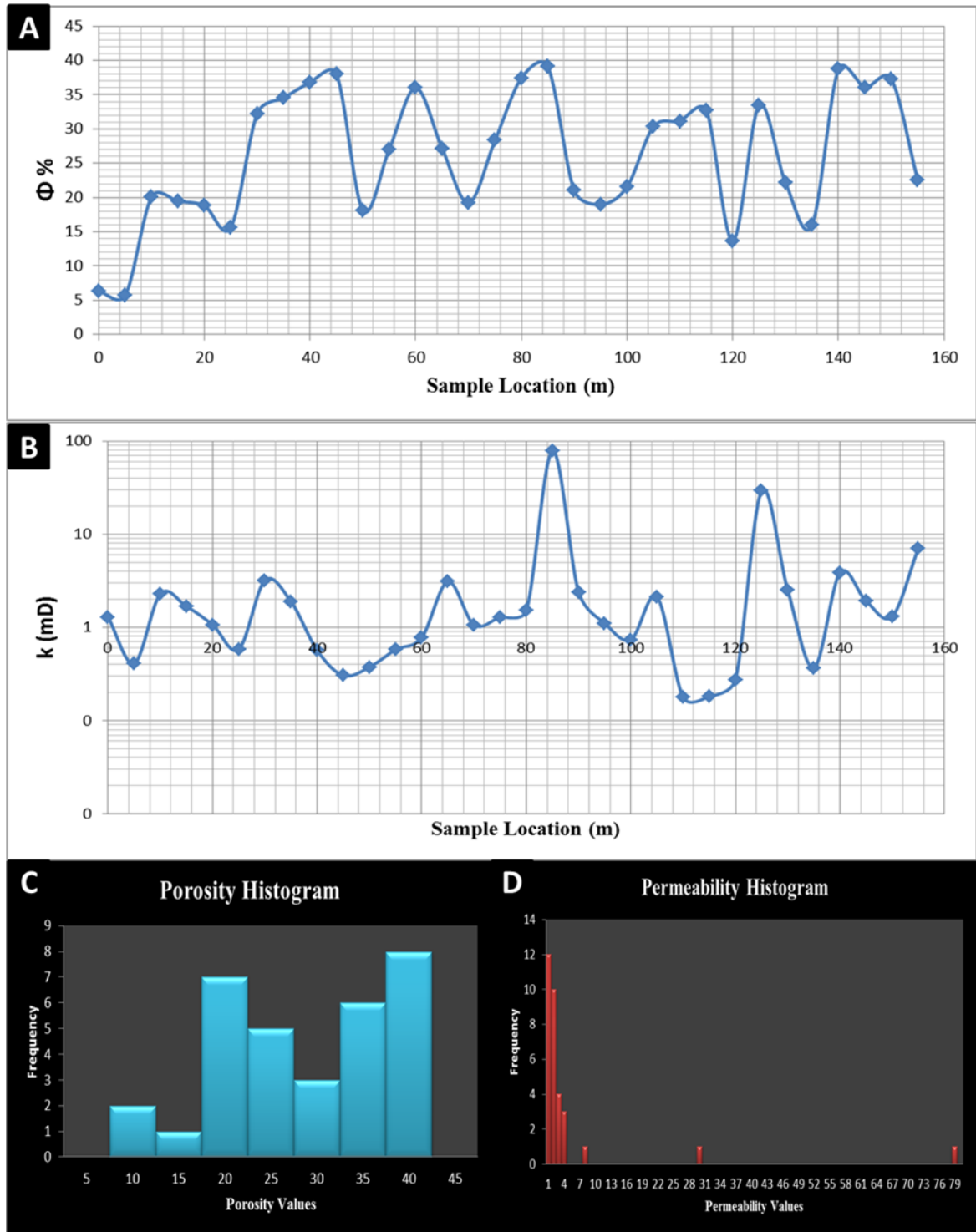


Figure 6.4 Cross plots for unit B; A: the distribution of the porosity values along the lateral profile; B: the distribution of the permeability values along the lateral profile; C: histogram for the porosity data; D: histogram for the permeability data

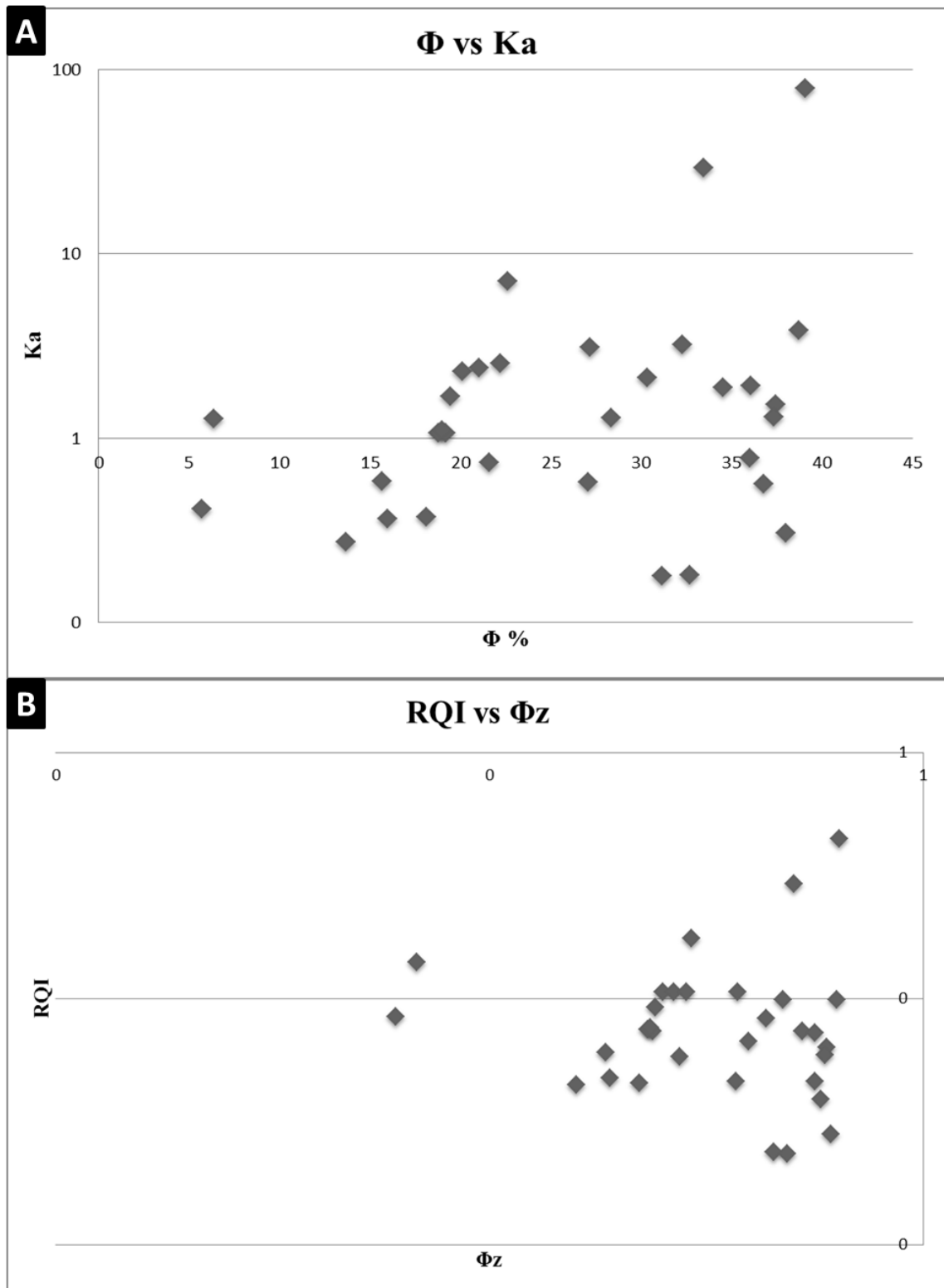


Figure 6.5 Cross plots for unit B; A: porosity vs permeability data; B: RQI vs  $\Phi_z$  data

The porosity – permeability cross plot showed that there is no any linear relationship between them and hence scattered values are dominant. Therefore, five samples have been selected to represent different highs and lows in their porosity and permeability values. These samples are: B-0, B-85, B-125, B-145 and B-155 where B is the reservoir name and the number indicates the sample location within the reservoir. B-0 represents the low porosity (6.4 %) and permeability (1.2 mD) zone, B-85 represents the high porosity (39 %) and permeability (78.4 mD) zone, B-125 also represents high porosity (33.5 %) and permeability (29 mD) zone, B-145 represents the high porosity (36 %) and low permeability (1.9 mD) zone and B-155 represents the medium porosity (22.6 %) and permeability (7.1 mD) zone. These five samples were examined by thin sections, SEM and XRD analysis (Figure 6.6).



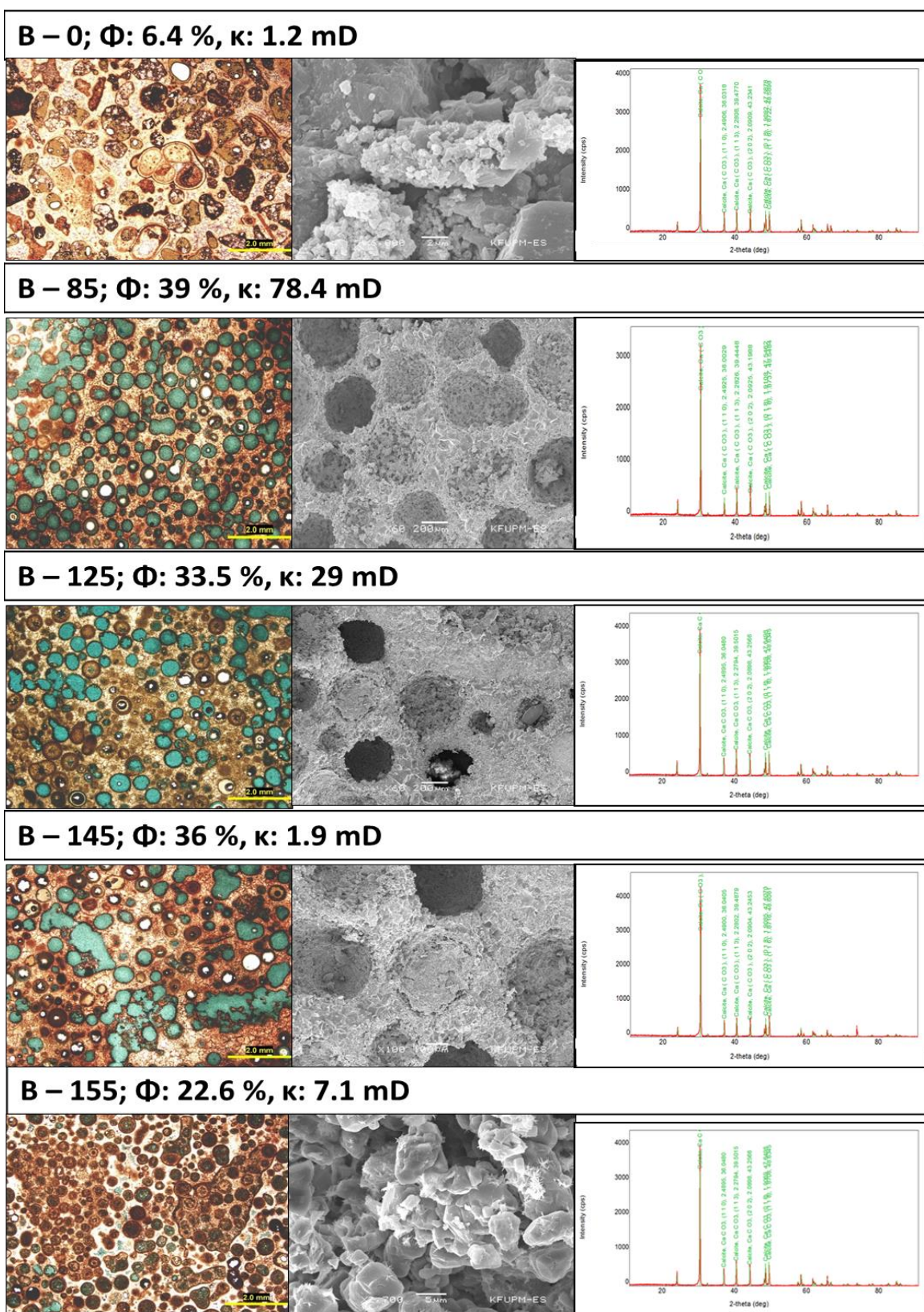


Figure 6.6 Thin sections, SEM and XRD analysis for the selected samples from the reservoir unit B

## 6.4 Data from Reservoir Unit C

The length of this unit is 65 m and the sampling was with 2.5 m spacing and the total samples collected from this unit are 27 samples. The average thickness for this unit is 1 m. Table 6.4 shows the measurements of the statistical parameters and the heterogeneity. Figure 6.7 shows the histograms of porosity and permeability along with number of cross plots used to evaluate the lateral variability.

The average porosity in unit C is 22.6 % while the average permeability in the same unit is 1.7mD. The standard deviation is 6.5 % for porosity and 3.2mD for the permeability. From the distribution of the porosity and permeability values it is clear that the trend of the variability of them is not similar like the previous cases. The variability degree is higher in the porosity; it decreases laterally for the permeability until it shows almost similar readings (Figures 6.7A and 6.7B). The histograms show that the porosity values are more or less normally distributed while the permeability values are positively skewed (Figures 6.7C and 6.7D).

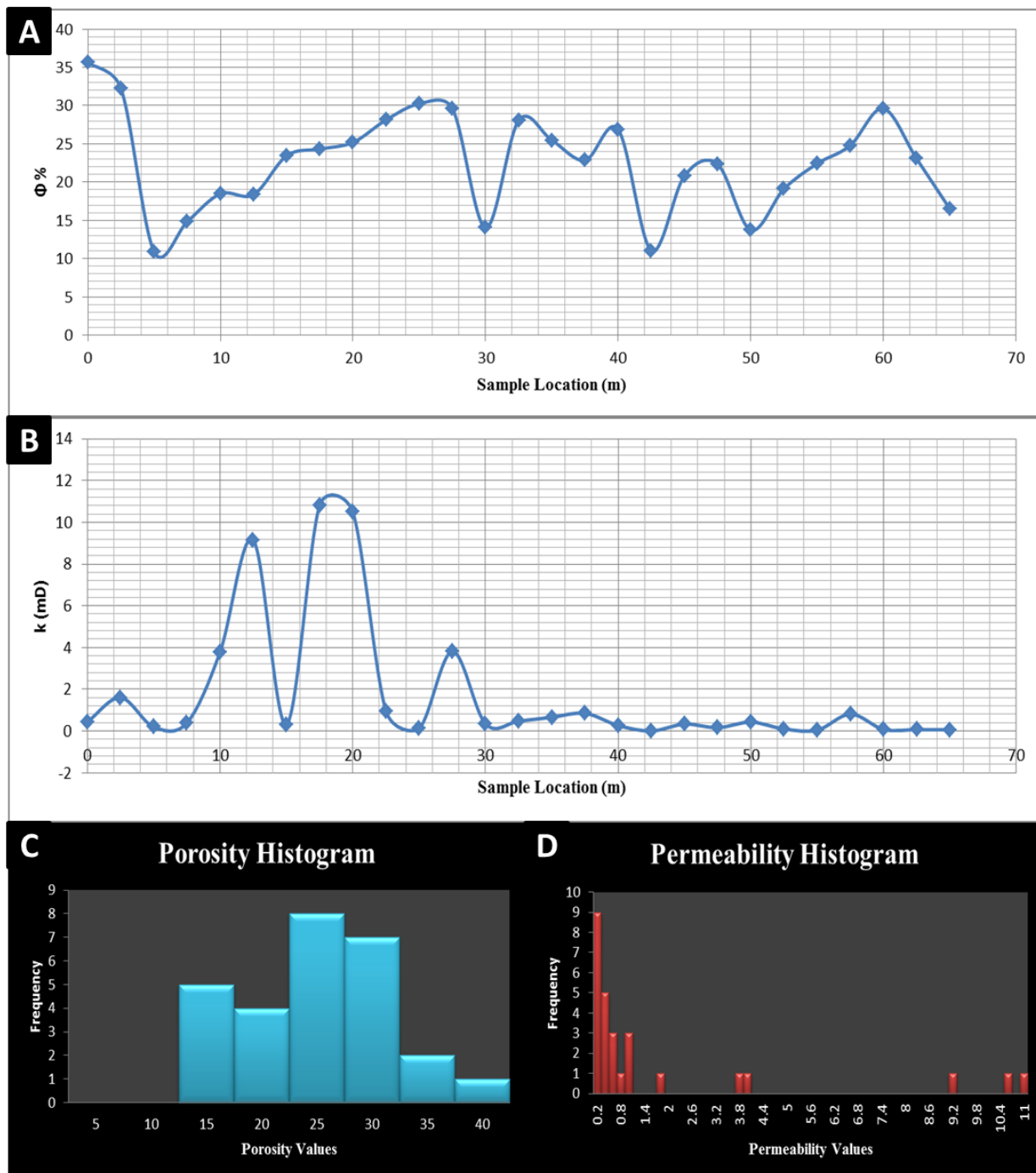
The cross plot of the porosity against permeability shows some populations with high porosity and low permeability and others with high porosity and permeability with correlation coefficient about 0.069 (Figure 6.8A). The cross plot of the RQI values versus the  $\Phi_z$  values in a double logarithmic scale shows several distinct flow units (Figure 6.8B).

**Table 6.4 A: The measurements of the third reservoir unit C; B: statistical parameters of the reservoir unit C**

<b>A</b>	Sample Location (m)	Fractional $\Phi$	$\Phi$ (%)	Ka (md)	RQI	$\phi z$	FZI
	0	0.3563	35.6280	0.4373	0.0348	0.5535	0.0629
	2.5	0.3222	32.2170	1.6006	0.0700	0.4753	0.1473
	5	0.1088	10.8760	0.1987	0.0424	0.1220	0.3478
	7.5	0.1484	14.8430	0.3902	0.0509	0.1743	0.2921
	10	0.1849	18.4850	3.7866	0.1421	0.2268	0.6267
	12.5	0.1837	18.3710	9.1524	0.2216	0.2251	0.9848
	15	0.2346	23.4600	0.3107	0.0361	0.3065	0.1179
	17.5	0.2433	24.3275	10.8113	0.2093	0.3215	0.6511
	20	0.2520	25.1950	10.5006	0.2027	0.3368	0.6019
	22.5	0.2814	28.1390	0.9615	0.0580	0.3916	0.1482
	25	0.3024	30.2390	0.1240	0.0201	0.4335	0.0464
	27.5	0.2958	29.5840	3.8164	0.1128	0.4201	0.2684
	30	0.1404	14.0370	0.3476	0.0494	0.1633	0.3026
	32.5	0.2808	28.0830	0.4774	0.0409	0.3905	0.1048
	35	0.2547	25.4680	0.6635	0.0507	0.3417	0.1483
	37.5	0.2285	22.8530	0.8496	0.0605	0.2962	0.2044
	40	0.2687	26.8680	0.2673	0.0313	0.3674	0.0852
	42.5	0.1105	11.0470	0.0065	0.0076	0.1242	0.0613
	45	0.2082	20.8170	0.3331	0.0397	0.2629	0.1511
	47.5	0.2234	22.3360	0.1617	0.0267	0.2876	0.0929
	50	0.1373	13.7320	0.4288	0.0555	0.1592	0.3486
	52.5	0.1910	19.1030	0.0975	0.0224	0.2361	0.0950
	55	0.2241	22.4070	0.0471	0.0144	0.2888	0.0499
	57.5	0.2479	24.7910	0.8099	0.0568	0.3296	0.1722
	60	0.2962	29.6230	0.0781	0.0161	0.4209	0.0383
	62.5	0.2308	23.0805	0.0683	0.0171	0.3001	0.0569
	65	0.1654	16.5380	0.0585	0.0187	0.1982	0.0942

<b>B</b>	Statistical Parameters	$\Phi$ statistics	k statistics
	m	22.6721	1.7328
	S	6.4790	3.1944
	Max.	35.6280	10.8113
	M	23.0805	0.3902
	Min.	0.0692	0.0065
	S <sup>2</sup>	41.9772	9.8265



**Figure 6.7** Cross plots for unit C; A: the distribution of the porosity values along the lateral profile; B: the distribution of the permeability values along the lateral profile; C: histogram for the porosity data; D: histogram for the permeability data

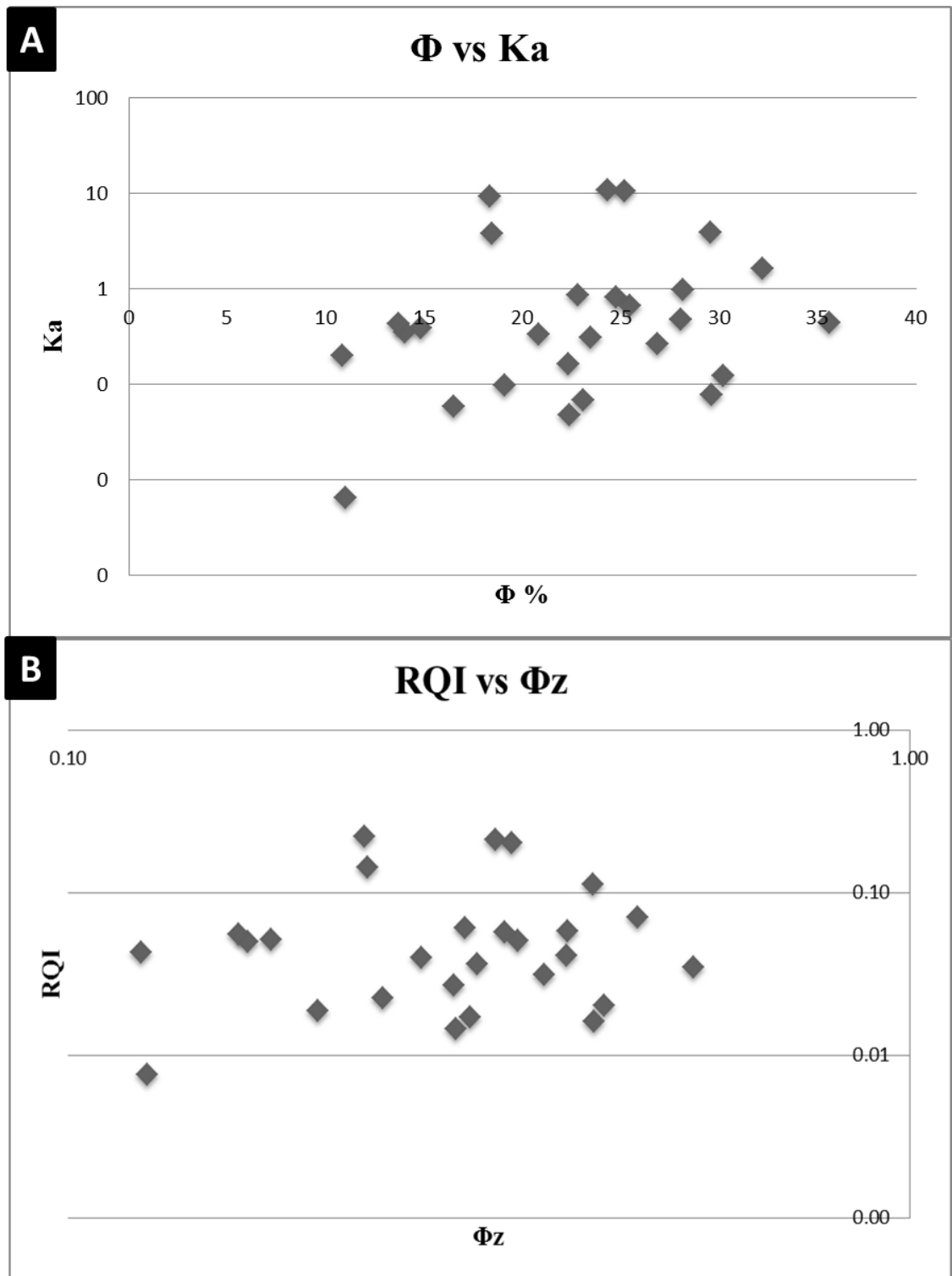


Figure 6.8 Cross plots for unit C; A: porosity vs permeability data; B: RQI vs  $\Phi_z$  data

The porosity – permeability cross plot showed that there is no any linear relationship between them and hence it reflects different populations. Therefore, four samples have been selected to represent different highs and lows in their porosity and permeability values. These samples are: C-0, C-5, C-10 and C-20 where C is the reservoir name and the number pointed to the sample location within the reservoir. C-0 represents the high porosity (35.6 %) and low permeability (0.43 mD) zone, C-5 represents the medium porosity (10.8 %) and low permeability (0.19 mD) zone, C-10 represents the medium porosity (18.5 %) and permeability (3.7 mD) zone and C-20 represents the high porosity (25.2 %) and permeability (10.5 mD) zone. These four samples were examined by thin sections, SEM and XRD analysis (Figure 6.9).



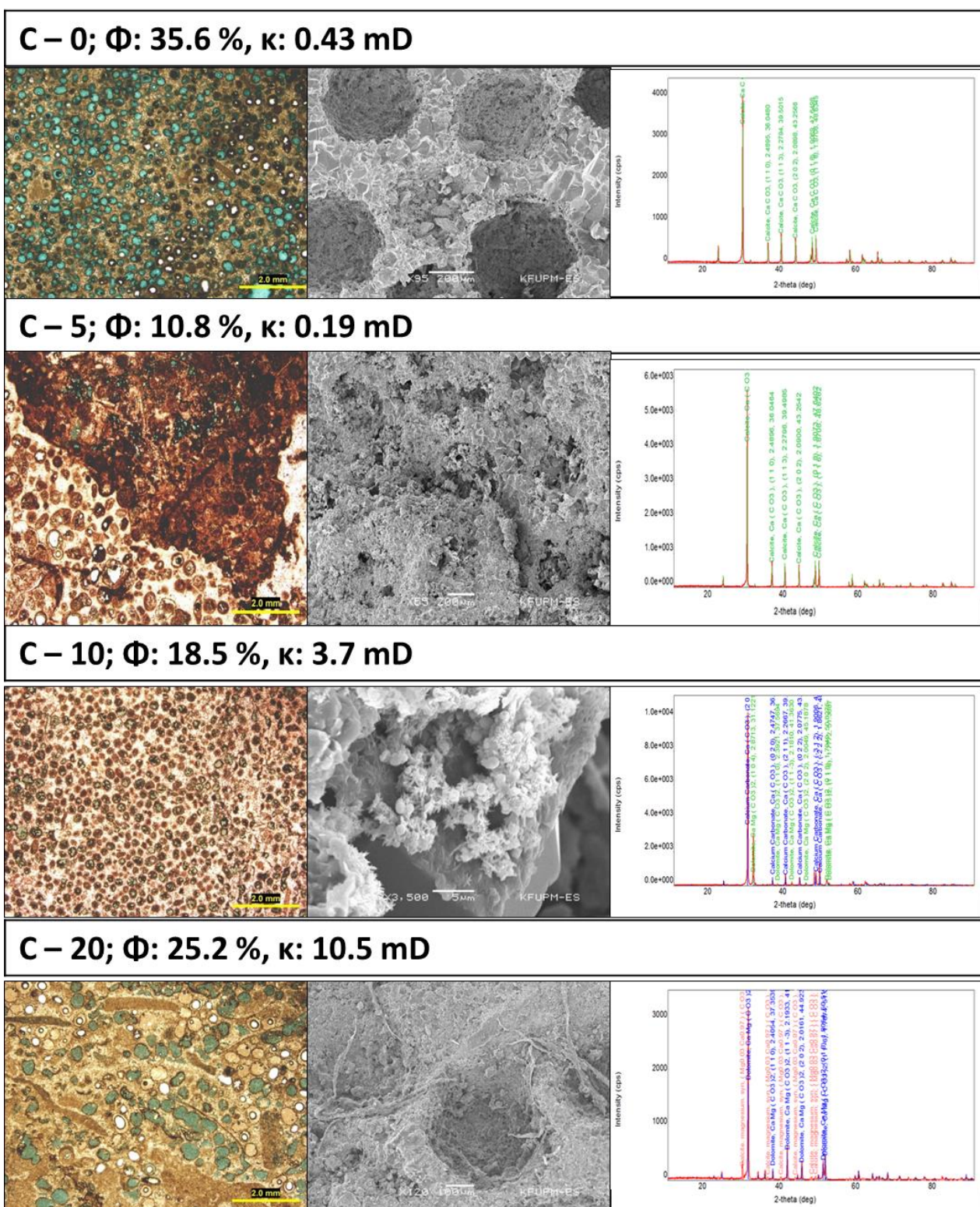


Figure 6.9 Thin sections, SEM and XRD analysis for the selected samples from the reservoir unit C

## 6.5 Interpretation and Discussion

A comparison between the reservoir units in term of their statistical parameters, lateral variability, histograms, cross plots and their correlation coefficients has been made to evaluate their quality and heterogeneity (Table 6.5). The average porosity for the reservoir units A, B and C were 10 %, 26 % and 22.6 % respectively while the average permeability for them were 0.4 mD, 4 mD and 1.7 mD. The standard deviation in porosity values for them were 4.8 %, 9.5 % and 6.5 % and were 0.2 mD, 14.4 mD and 3.2 mD for the permeability. The variability graph according to the lateral distribution of the values showed higher variability in unit B than the other units in both the porosity and permeability values. The variance degree is higher in unit B because of the anomalies in the porosity and permeability values occurring within this unit. In terms of quality the reservoir unit B is considered to be the best because it has the highest porosity and permeability values. Then, unit C in the second rank and unit A is the worst among them.

To examine the small scale heterogeneity and the causes of it, 12 samples collected from the three units (4 from each) and they have been prepared for thin sections, SEM and XRD analysis. The results from this detailed analysis showed that the three reservoir units are heterogeneous in the micro-scale. In reservoir A, the thin sections revealed that there is a change in the microfacies laterally from highly cemented peloidal oolitic dolomitic packstone to oomoldic porosity oolitic grainstone with increasing in the permeability and the presence of shell fragments. The SEM inferred the bad permeability and the high cement material between the grains in the samples. XRD analysis confirmed the existence of dolomite beside the original calcite in this reservoir unit. In reservoir unit



B, the thin sections revealed that there is a change in the microfacies laterally from highly cemented skeletal grainstone to peloidal oolitic grainstone with the presence of respective amounts of aggregates. Note also that the permeability decreases with the increasing of the skeletal fragments and the aggregate grains. The SEM inferred the good porosity and the ooids were clear in the SEM images and there also appeared some clayey material which may be the cause of the low permeability in two samples. XRD analysis confirmed the existence of the original calcite in this reservoir unit and no dolomite was detected. In reservoir unit C, the thin sections revealed that there is a change in the microfacies laterally from leached oolitic grainstone to cemented skeletal oolitic grainstone with the presence of skeletal fragments and intraclasts. The SEM inferred the high porosity and low permeability of some samples and this may be caused by the high cement material between the ooids and by the pores which are not connected. XRD analysis confirmed the existence of dolomite beside the original calcite in this reservoir unit.

The detailed analysis of the samples from the reservoir units showed that there is noticeable small scale heterogeneity within them. To rank the units according to their heterogeneity level a comparison between all the previous results gives the following reservoir units ranking. Unit C is considered to be the most heterogeneous unit, then reservoir unit B and the less heterogeneous one would be unit A.

**Table 6.5 A comparison between the three reservoir units**

<b>Reservoir Name</b>	<b>Average <math>\Phi</math> (%)</b>	<b>S for <math>\Phi</math></b>	<b>Average k (mD)</b>	<b>S for k</b>	<b>R<sup>2</sup> for <math>\Phi</math> vs k</b>	<b>R<sup>2</sup> for RQI vs <math>\Phi_z</math></b>
A	10	4.8	0.4	0.2	0.92	0.177
B	26	9.5	4	14.4	0.3	0.162
C	22.6	6.5	1.7	3.2	0.069	0.004

## **CHAPTER 7**

# **CONCLUSIONS AND RECOMMENDATIONS**

### **7.1 Conclusions**

I studied four vertical stratigraphic outcrop sections of Upper Khartam Member in Central Saudi Arabia. A composite section was constructed for the Upper Khartam Member which is bounded at the bottom by the Permian\Triassic boundary and at the top by a sequence boundary within the Upper Khartam Member. The sedimentological and stratigraphical investigations revealed that the composite sequence comprises of 6 lithofacies associations for the Upper Khartam. These lithofacies were deposited into the following environments: 1) ravinement marine transgression, 2) foreshoal, and 3) shoal complex. The Upper Khartam Member is composed of three High Frequency Sequences (HFSs) in the studied outcrop. These HFSs exhibit general shallowing upward pattern. The bottoms of HFS-1 and HFS-2 represent the shallowest environments (marine transgression). The tops of HFS-1 and HFS-2 and the entire HFS-3 represent relatively deep water.

I applied LiDAR scanning on part of the studied outcrop using Riegl VZ-4000 instrument. The digital model produced was integrated with the sedimentology and stratigraphy data to build facies model and stratigraphic model. The stratigraphic horizons were accurately picked from the digital model along with the bed thicknesses. Packages of software were used from the acquisition to the interpretation of the digital

model. These software include RiScan, Polyworks, VRGS, Draping software and ArcGIS. I summarized the recommended workflow for the digital modelling and the benefits and limitations for this recent technique. The detailed study for the lateral profiles of the reservoir units revealed that the reservoir unit B is the best in term of quality but it is the worst in term of variability. The reservoir unit C is considered the most heterogeneous unit because of the variation in the microfacies, petrophysical properties and mineral composition. The least heterogeneous unit is A because of the small differences in term of microfacies and petrophysical properties.

## **7.2 Recommendations**

Since Saudi Arabia has good outcrop analogs for the subsurface reservoirs it is promising to apply the digital outcrop modeling approach on them. This will result in what can be called digital outcrop models library for the reservoir analogs in Saudi Arabia. The digital modelling should be integrated with traditional field investigations.

The data from such an integrated study will be enhanced through the combination with the data from subsurface to increase the confidence and make accurate results.

## References

- Adams, E.W., Grélaud, C., Pal, M., Csoma, A. E., Al Ja'aidi, O. S. and Al Hinai, R. 2011. Improving reservoir models of Cretaceous carbonates with digital outcrop modelling (Jabal Madmar, Oman): static modelling and simulating clinoforms. *Petroleum Geoscience*, v. 17, p. 309–332.
- Adams, E.W., Grotzinger, J.P., Watters, W.A., Schroder, S., McCormick, D.S. and Al-Siyabi, H.A. 2005. Digital characterization of thrombolite-stromatolite reef distribution in a carbonate ramp system (terminal Proterozoic, Nama Group, Namibia). *AAPG Bulletin*, v. 89, no. 10, p. 1293 – 1318.
- Aigner, T. 1982. Calcareous tempestites: storm-dominated stratification in Upper Muschelkalk limestones (Middle Trias, SW-Germany). In, G. Einsele and A. Seilacher (Eds.), *Cyclic and Event Stratification*. Springer-Verlag, Berlin, p. 180-198.
- Al-Anazi, H.A., Al-Baqawi, A.M., Abdul Aziz, A.A. and Al-Kanaan, A.A. 2010. Effective Strategies in Development of Heterogeneous Gas Condensate Carbonate Reservoirs. *Saudi Aramco Journal of Technology*, 3.
- Al-Aswad, A.A. 1997. Stratigraphy, sedimentary environment and depositional evolution of the Khuff formation in south-central Saudi Arabia. *Journal of petroleum geology*, v. 20, no. 3, p. 307-326.
- Al-Aswad, A.A. and Kamel, S. M. 1992. Late Permian microfossils from the southern Khuff Formation, southern Saudi Arabia. In " *Geology of the Arab World: Proceedings*

of the First International Conference on Geology of the Arab World". Edited by A. Sadek.p. 345- 365.

Alway, R. H. S., Broomhall, R. W., Hulstrand, R. F., Al-Mansoori, A., Abdalla, A. A., and Al-Aidarous, A. 2002. Sequence Stratigraphy of the Khuff Formation Comparing Subsurface and Outcrop Data (Arabian Plate, U.A.E.). Society of Petroleum Engineers.doi:10.2118/78535-MS.

Al-Dukhayyil, R.K. 2007. High-resolution sequence stratigraphy of the Khuff A and B carbonates in the subsurface of Haradh area, Southern ghawar field, Saudi Arabia. MSc thesis, King Fahd University of Petroleum and Minerals.

Al-Dukhayyil, R.K., and Al-Tawil, A.A. 2007. Reservoir architecture of the Triassic Khartam carbonate sequence, Khuff outcrop analogue in Al-Qasim, central Saudi Arabia. 7th Middle East Geosciences Conference, GEO 2006. GeoArabia, Abstract, v. 12, no. 3, p. 136.

Al-Farhan, M.S. 2010. Geosciences Information System (GeoIS): A Geospatial Paradigm for Real and Virtual 3D Worlds. PhD Dissertation, The University of Texas at Dallas.

Al-Farhan, M., White, L., Tuck, D., Aiken, C. 2008. Laser rangefinders and ArcGIS combined with three-dimensional photorealistic modeling for mapping outcrops in the Slick Hills, Oklahoma. Geosphere,v. 4, p. 576-587.

Al-Farhan, M., Deng, J., White, L., Meyer, R., Oldow, J., Krause, F., Aiken, C. and Aguilera, R. 2009. LiDAR Technology as a Means of Improving Geologic, Geophysical

and Reservoir Engineering Evaluations: From Rocks to Realistic Fluid Flow Models. Canadian International Petroleum Conference (CIPC) Calgary, Alberta, Canada.

Al-Husseini, M.I. 2004. Pre-Unayzah unconformity, Saudi Arabia. In M.I. Al-Husseini (Ed.), Carboniferous, Permian and Early Triassic Arabian Stratigraphy. GeoArabia Special Publication 3, Gulf PetroLink, Bahrain, p. 15-59.

Al-Husseini, M.I. 2000. Origin of the Arabian Plate structures: Amar collision and Najd rift. GeoArabia, v. 5, no. 4, p. 527-542.

Al-Jallal, A.I. 1995. The Khuff Formation: Its Reservoir potential in Saudi Arabia and other gulf countries; Depositional and stratigraphic approach. Middle East Petroleum Geosciences, v. I. p. 103-119.

Al-Khalifah, F.A., Abdullatif, O. M. and Makkawi, M.H. 2004. Sedimentology and geostatistical modeling of Quwarah Member, Qasim Formation: Paleozoic sandstone reservoir outcrop analog, Saudi Arabia. 6th Middle East Geosciences Conference, GEO 2004. GeoArabia, Abstract, v. 9, no. 1, p. 30.

Alsharhan, A.S. and Narin, A. E. M. 2003. Sedimentary Basins and Petroleum Geology of the Middle East: Elsevier Pub., Chap. 5-6, p. 141-178.

Amaefule, J.O., Altunbay, M., Tiab, D., Kersey, D.G. and Keelan D.K. 1993. Enhanced Reservoir Description: Using Core and Log Data to Identify Hydraulic (Flow) Units and Predict Permeability in Uncored Intervals/Wells. Society of Petroleum Engineers, SPE 26436.

Angiolini, L., Vaslet, D., Le Nindre, Y.M. and Zarbo, M. 2006. New records and new taxa of Permian brachiopods from the Khuff Formation, Midhnab Member, Central Saudi Arabia, *Geoarabia*, v. 11, no. 1, p. 45 -58.

Bellian, J.A., Jennette, D.C., Kerans, C., Gibeaut, J., Andrews, J., Yssldyk, B. and Larue, D. 2002.3-Dimensional Digital Outcrop Data Collection and Analysis Using Eyesafe Laser (LIDAR) Technology.Poster session at AAPG Convention, Houston, Texas.

Bellian, J. A., Kerans, C. and Jennette, D.C. 2005. Digital outcrop models: applications of terrestrial scanning lidar technology in stratigraphic modeling. *Journal of Sedimentary Research*, v. 75, no. 2, p. 166–176.

Bendias, D., Koehrer, B., Obermaier, M. and Aigner, T. 2013. Mid-Permian Khuff Sequence KS6: Paleorelief-influenced facies and sequence patterns in the Lower Khuff time-equivalent strata, Oman Mountains, Sultanate of Oman. *GeoArabia*, v. 18, no. 3, p. 135-178.

Beydoun, Z.R. 1989. Petroleum Geology of the Red Sea – Gulf of Aden I (Scientific Editor).*Journal of Petroleum Geology*, v. 12, no. 2.

BP Statistical Review of World Energy June 2013.

Bryant, I., Carr, D., Cirilli, P., Drinkwater, N., McCormick, D., Tilke, P. and Thurmond, J. 2000. Use of 3D digital analogues as templates in reservoir modelling. *Petroleum Geoscience*, v. 6, p. 195 – 201.

Buckley, S.J., Schwarz, E., Terlaky, V., Howell, J. A. and Arnott, R.W. 2009. Terrestrial laser scanning combined with photogrammetry for digital outcrop modelling. Bretar F,



Pierrot-Deseilligny M, Vosselman G (Eds) Laser scanning 2009, IAPRS, Vol. XXXVIII, Part 3/W8 – Paris, France, September 1-2.

Buckley, S. J., Schwarz, E. and Terlaky, V. 2010. Combining aerial photogrammetry and terrestrial lidar for reservoir analog modeling. *Photogrammetric Engineering and Remote Sensing*, v. 76, p. 953 – 963.

Chirat, R., Vaslet, D. and Le Nindre, Y.M. 2006. Nautiloids of the Permian-Triassic Khuff Formation, central Saudi Arabia. *GeoArabia*, v. 11, no. 1, p. 81-92.

Crasquin-Soleau, S., Vaslet, D. and le Nindre, Y.M. 2006. Ostracods of the Permian Triassic khuff Formation, Saudi Arabia. *Palaeoecology and palaeobiography*, *GeoArabia*, v. 11, no. 1, p. 55 – 76.

Dasgupta, S.N., Hong, M. R. and Al-Jallal, I.A. 2002. Reservoir characterization of Permian Khuff-C carbonate in the supergiant Ghawar Field of Saudi Arabia. *The leading edge journal*, v. 20, no. 7, p. 706 – 717.

Delfour, J., Dhellemmes, R., Elsass, P., Vaslet, D., Brosse, J., Le Nindre, Y. M. and Dottin, O. 1982. Explanatory notes to the geologic map of the Ad Dawadimi Quadrangle, Kingdom of Saudi Arabia. *Geoscience Map GM-60C*, scale 1:250,000, sheet 24G. Deputy Ministry for Mineral Resources, Ministry of Petroleum and Mineral Resources, Kingdom of Saudi Arabia. p. 36.

Dunham, R.J. 1962. Classification of carbonate rocks according to depositional textures. *American Association of Petroleum Geologists*.

Eltom, H., Makkawi, M., Abdulatif, O. and Alramadan, K. 2012. High-resolution facies and porosity models of the upper Jurassic Arab-D carbonate reservoir using an outcrop analogue, central Saudi Arabia. *Arabian Journal of Geosciences*, v. 6, no. 11, p. 4323 – 4335.

Eltom, H., Abdulatif, O., Makkawi, M. and Abdulraziq A. 2014a. Characterizing and modeling the Upper Jurassic Arab-D reservoir using outcrop data from Central Saudi Arabia. *GeoArabia*, v. 19, no. 2, p. 53 – 84.

Eltom, H., Abdulatif, O., Babalola, L., Bashari, M., Yassin, M., Osman, M. and Abdulraziq, A. 2014b. Characterization of the Late Permian - Early Triassic Upper Khuff Formation: Outcrop study and implications for Hydrocarbon Reservoirs. *Geo Arabia*, In press in review.

Enge, H.D., Buckley, S. J., Rotevatn, A. and Howell, J.A. 2007. From outcrop to reservoir simulation model: workflow and procedures. *Geosphere*, v. 3, p. 469 – 490.

Fabuel-Perez, I., Hodgetts, D. and Redfern, J. 2009. A new approach for outcrop characterization and geostatistical analysis of a low-sinuosity fluvial-dominated succession using digital outcrop models: upper triassic oukaïmeden sandstone formation, central high Atlas, Morocco. *AAPG Bulletin*, v. 93, p. 795 – 827.

Fabuel-Perez, I., Hodgetts, D. and Redfern, J. 2010. Integration of digital outcrop models (DOMs) and high resolution sedimentology workflow and implications for geological modelling: oukaïmeden Sandstone Formation, High Atlas (Morocco). *Petroleum Geoscience*, v. 16, p. 133 – 154.

Fitch, P., Davies, S. and Lovell, M. 2013. Reservoir Quality and Reservoir Heterogeneity: Petrophysical Application of the Lorenz Coefficient. *Petrophysics*, v. 54, p. 465 – 474.

Haase, M.M. and Aigner, T. 2013. High-resolution anatomy of a grainstone package in Khuff Sequence KS4, Oman Mountains, Sultanate of Oman. *GeoArabia*, v. 18, no. 4, p. 17 – 44.

Hodgetts, D. 2013. Laser scanning and digital outcrop geology in the petroleum industry: A review. *Marine and Petroleum Geology*, v. 46, p. 335 – 354.

Howell, J., Vassel, A. and Aune, T. 2008. Modeling of dipping clinoform barriers within deltaic outcrop analogues from the Cretaceous Western Interior Basin USA. *Geological Society, London, Special Publications*, v. 309, no. 1, p. 99 – 121.

Hughes, G.W. 2004. Middle to Upper Jurassic Saudi Arabian carbonates petroleum reservoirs: biostratigraphy, micropalaeontology and palaeoenvironments. *GeoArabia*, v. 9, no. 3, p. 79 – 114.

Hughes, G.W. 2005. Saudi Arabian Permo-Triassic biostratigraphy, micropalaeontology and palaeoenvironment. Recent developments in applied biostratigraphy, The micropalaeontological society. *Special publications*, p. 91 – 108.

Insalaco, E., Virgone, A., Courme, B., Gaillot, J., Kamali, M., Moallemi, A., Lotfpour, M. and Monibi, S. 2006. Upper Dalan Member and Kangan Formation between the Zagros Mountains and offshore Fars, Iran: Depositional system, biostratigraphy and stratigraphic architecture. *GeoArabia*, v. 11, no. 2, p. 75 – 176.

Janson, X., Lucia, F. J., Jennings, J. W., Bellian, J. A., AbuBshait, A. A., Al-Dukhayil, R. K., Mueller, H. W. and Cantrell, D. 2013. Outcrop-based 3D geological and reservoir model of the uppermost Khuff Formation in central Saudi Arabia, in Pöppelreiter, M., ed., Permo-Triassic Sequence of the Arabian Plate: EAGE Special Publication, p. 269 – 302.

Jia, A., He, D. and Jia, C. 2012. Advances and Challenges of Reservoir Characterization: A Review of the Current State-of-the-Art. Chapter 9, Earth Sciences book. DOI: 10.5772/26404.

Koehrer, B., Zeller, M., Aigner, T., Pöppelreiter, M., Milroy, P., Forke, H. and Al-Kindi, S. 2010. Facies and stratigraphic framework of a Khuff outcrop equivalent: Saiq and Mahil formations, Al Jabal al-Akhdar, Sultanate of Oman. *GeoArabia*, v. 15, no. 2, p. 91 – 156.

Koehrer, B., Aigner, T. and Pöppelreiter, M. 2011. Field-scale geometries of Upper Khuff reservoir geobodies in an outcrop analogue (Oman Mountains, Sultanate of Oman). *Petroleum Geoscience*, v. 17, p. 3–16.

Koehrer, B., Aigner, T., Forke, H. and Pöppelreiter, M. 2012. Middle to Upper Khuff (Sequences KS1 to KS4) outcrop-equivalents in the Oman Mountains: Grainstone architecture on a subregional scale. *GeoArabia*, v. 17, no. 4, p. 59 – 104.

Konert, G., Affi, A.M., Al-Hajri, S.A. and Droste, H.J. 2001. Paleozoic Stratigraphy and Hydrocarbon Habitat of the Arabian Plate. *GeoArabia*, v. 6, no. 3, p. 407 – 442.

Kurz, T.H., Buckley, S. J. and Howell, J.A. 2012. Close range hyperspectral imaging integrated with terrestrial lidar scanning applied to rock characterisation at centimetre scale, International Archives of the Photogrammetry, Remote Sensing and Spatial Information Sciences, v. XXXIX-B5, XXII ISPRS Congress.

Labourdette, R. and Jones, R.R. 2007. Characterization of fluvial architectural elements using a three-dimensional outcrop data set: Escanilla braided system, south – Central Pyrenees, Spain. *Geosphere*, v. 3, p. 422 – 434.

Lapponi, F., Casini, G., Sharp, I., Blendinger, W., Fernández, N., Romaine, I. and Hunt, D. 2011. From outcrop to 3D modelling: a case study of a dolomitized carbonate reservoir, Zagros Mountains, Iran. *Petroleum Geoscience*, v. 17, p. 283–307.

Lindsay, R.F. and Hughes, G.W. 2010. Saudi Arabian Jurassic outcrops and reservoir equivalents. A pictorial Review. *The oil Drop*, v. 22, no. 2, p. 6 – 11.

Lindsay, R. F., Hughes, W. and Aba Al-Hassan, S. 2010. Khuff-A reservoir porosity creation and destruction; a product of depositional and diagenetic processes. Abstracts: Annual Meeting - American Association of Petroleum Geologists.

Manivit, J., Vaslet, D., Berthiaux, A., Le Strat, P. and Fourniguet, J. 1986. Explanatory Notes of the Geological map of the Buraydah Quadrangle Sheet 26 G, kingdom of Saudi Arabia. Ministry of Petroleum and Mineral Resources. Deputy Ministry for Mineral Resources, p. 32.

Martinius, A. W., Elfenbein, C., Jacobsen, T., Keogh, K. J., Morriss, S., Nordahl, K., Næss, A. and Ringrose, P. S. 2007. Geo to Flow – Linking Multiscale Digital

OutcropLibraries to Dynamic Reservoir Behaviour.I026, EAGE 69th Conference & Exhibition — London, UK.

Maurer, F., Martini, R., Rettori, R., Hillgärtner, H. and Cirilli, S. 2009. The geology of Khuff outcrop analogues in the Musandam Peninsula, United Arab Emirates and Oman. *GeoArabia*, v. 14, no. 3, p. 125 – 158.

McCaffrey, K. J., Jones, R.R., Holdsworth, R.E., Wilson, R.W., Clegg, P., Imber, J., Holliman, N. and Trinks, I. 2005. Unlocking the spatial dimension: digital technologies and the future of geoscience fieldwork. *Journal of the Geological Society*, v. 162, p. 927 – 938.

Mohaghegh, S., Arefi, R., Ameri, S. and Hefner, M. H. 1994.A Methodological Approach for Reservoir Heterogeneity Characterization Using Artificial Neural Networks. SPE Annual Technical Conference & Exhibition held in New Orleans, LA, U.S.A.

Osman, M., Abdullatif, O., Al-Farhan, M. Eltom, H. Adam, A. and Bashri, M. 2014a.High Resolution Stratigraphy and Reservoir Heterogeneity of Khartam Member of Khuff Formation from Outcrop, Saudi Arabia. Published abstract from the EAGE 76<sup>th</sup> annual conference and exhibitions.

Osman, M, Abdullatif, O., Eltom, H. and Adam, A. 2014b.Outcrop-Scale Geometry and Architecture of the Reservoir Units from an Analog to the Early Triassic Khuff-A Reservoir, Central Saudi Arabia. Published abstract from the AAPG conference

- Pérez-López, A. 2001. Significance of pot and gutter casts in a Middle Triassic carbonate platform, Betic Cordillera, southern Spain, *Sedimentology*, v. 48, no. 6, p. 1371 – 1388.
- Powers, R.W. 1968. Saudi Arabia (excluding the Arabian Shield), *Lexique Stratigraphique International*, Paris, vol. III, Asie.
- Powers, R. W., Ramirez, L. F., Redmond, C. D. and Elberg, E. L. 1966. Geology of the Arabian Peninsula. Sedimentary geology of the Saudi Arabia. U. S. Geological Survey Professional Paper 560-D. p. 147.
- Pranter, M.J., Reza, Z.A. and Budd, D.A. 2006. Reservoir-scale characterization and multiphase fluid-flow modeling of lateral petrophysical heterogeneity within dolomite facies of the Madison Formation, Sheep Canyon and Lysite Mountain, Wyoming, USA. *Petroleum Geoscience*, v. 12, p. 29 – 40.
- Pringle, J.K., Brunt, R.L., Hodgson, D.M. and Flint, S.S. 2010. Capturing stratigraphic and sedimentological complexity from submarine channel complex outcrops to digital 3D models, Karoo Basin, South Africa. *Petroleum Geoscience*, v. 16, p. 307–330.
- Pringle, J.K., Howell, J.A., Hodgetts, D., Westerman, A. R. and Hodgson, D.M. 2006. Virtual outcrop models of petroleum reservoir analogues: a review of the current state-of-the-art. *First Break*, v. 24, p. 33 – 42.
- Pringle, J.K., Westerman, A.R., Clark, J.D., Drinkwater, N. J. and Gardiner, A.R. 2004. 3D high-resolution digital models of outcrop analogue study sites to constrain reservoir model uncertainty: an example from Alport Castles, Derbyshire, UK. *Petroleum Geoscience*, v. 10, p. 343–352.

- Rankey, E.C. 2013. Contrasts between wave- and tide-dominated oolitic systems: Holocene of Crooked–Acklins Platform, southern Bahamas. *Facies*, v. 60, no. 2, p. 405 – 428.
- Rankey, E.C. and Reeder, S.L. 2011. Holocene Oolitic Marine Sand Complexes of the Bahamas, *Journal of Sedimentary Research*, v. 81, p. 97–117.
- Sharland, P.R., Archer, R., Casey, D.M., Davies, R.B., Hall, S.H., Heward, A.P., Horbury, A.D. and Simmons, M.D. 2001. Arabian Plate sequence Stratigraphy. *GeoArabia Special Publication 2*, Gulf PetroLink, Bahrain, p. 371.
- Steineke, M. and Bramkamp, R.A. 1952. Mesozoic Rocks Eastern Saudi Arabia (Abstract). *AAPG*, v. 36, p. 909.
- Steineke, M., Bramkamp, R.A. and Sander, N.J. 1958. Stratigraphic relations of Arabian Jurassic Oil, habitat of oil. *AAPG*, p. 1294 – 1329.
- Vachard, D., Gaillot, J., Vaslet, D. and Le Nindre, Y. M. 2005. Foraminifers and algae from khuff Formation late Middle Permian – Early Triassic of Central Saudi Arabia. *GeoArabia*, v. 10, no. 4, p. 137 – 186.
- Vaslet, D., Le Nindre, Y.M., Vachard, D., Broutin, J., Crasquin-Soleau, S., Berthelin, M., Gaillot, J., Halawani, M. and Al-Husseini, M. 2005. The Permian-Triassic Khuff Formation of Central Saudi Arabia. *GeoArabia*, v. 10, no.4, p. 77 – 134.
- White, L.S. 2010. The Development of Computer Algorithms for the Construction and Analysis of Photorealistic 3D Virtual Models of Geological Outcrops. Master Thesis, The University of Texas at Dallas.



Wilson, C.E., Aydin, A., Karimi-Fard, M., Durlofsky, L.J., Sagy, A., Brodsky, E. E., Kreylos, O. and Kellogg, L.H. 2011. From outcrop to flow simulation: constructing discrete fracture models from a LIDAR survey. AAPG Bulletin, v. 95, p. 1883 – 1905.

Zeller, M., Koehrer, B., Adams, E. W., Pöppelreiter, M. and Aigner, T. 2011. Near well scale heterogeneities of a Khuff outcrop equivalent, Saiq Plateau, Oman. Journal of Petroleum Geology, v. 34, no. 3, p. 241 – 260.

Ziegler, M. A. 2001. Late Permian to Holocene paleofacies evolution of the Arabian Plate and its hydrocarbon occurrences. GeoArabia, v. 6, no. 3, p. 445 – 504.

## Vitae

**Name:** Mutasim Sami Mutasim Osman.

**Date of Birth:** 17<sup>th</sup> January 1987.

**Religion:** Muslim.

**Gender & Marital Status:** Male, Single.

**Address:** King Fahd University of Petroleum and Minerals, Dhahran, Saudi Arabia.

**Email:** [smutasim@hotmail.com](mailto:smutasim@hotmail.com)

**Mobile Number:** +966566526805

**Driving License:** Valid License.

### - Education and Academic Qualifications

**Jan. 2012 – May 2014:** Awarded Master of Science (in Geology) in Earth sciences Department, King Fahd University of Petroleum and Minerals, Saudi Arabia. (CGPA: 3.75).

**Sep. 2004 – Nov. 2009:** Awarded the degree of Bachelor of Science (Honours) First Class in Geology, Specializing in Petroleum Geology, Department of Geology, Faculty of Science, University of Khartoum, Sudan. (CGPA: 7.22).

**October 2009:** Obtained a Certificate in English language Communication from Sudan National Centre for Languages.

## **- Projects and Field Experience**

**May 2014:** Master thesis with title “Digital Outcrop Modelling of the Early Triassic Upper Khartam Member of Khuff Formation; Implications for Reservoir Heterogeneity and Quality, Central Saudi Arabia”.

**February 2014:** Application of laser scanning LiDAR and hyper-spectral camera on the outcrop of Khartam member, Qasim, Central Saudi Arabia.

**May and July 2013:** High resolution sedimentological and stratigraphical studies applied on Khartam Member of Khuff Formation in Qasim, Central Saudi Arabia.

**December 2012:** Sedimentological and stratigraphical studies on Minjur and Marat Formations exposed west of Riyadh, Saudi Arabia.

**April 2011:** Training with the ministry of Petroleum in Baleela oil Field, South Kordofan State, SW Sudan.

**August 2009:** BS graduation project title was “Source rock evaluation of Abu Gabra, Muglad basin, SW Sudan”. In this project one well was selected for systematic combination of organic geochemistry and palynofacies techniques. The purpose was to evaluate the potentiality of the source rock by assessing both the quality and generation capacity of the organic matter constituents.

## **- Training and Work Experience**

**Jan. 2012 – May 2012:** Teaching Assistant in petrology and paleontology labs, Earth sciences department, King Fahd University of Petroleum and Minerals.

**March 2011 – May 2011:** Training period in the Ministry of Petroleum specifically in the Oil Exploration and Production Administration. Khartoum, Sudan.

**January 2011 –February 2011:** Training Period in Red Rock Company for Mining. Khartoum, Sudan.

## **- Conferences and Participation**

**September 2014:** Outcrop-Scale Geometry and Architecture of the Reservoir Units from an Analog to the Early Triassic Khuff-A Reservoir, Central Saudi Arabia. Accepted as oral presentation in the AAPG 2014 International Conference & Exhibition in Istanbul.

**June 2014:** High Resolution Stratigraphy and Reservoir Heterogeneity of Khartam Member of Khuff Formation from Outcrop, Saudi Arabia. Accepted to be presented as E – Poster in the 76th EAGE Conference & Exhibition 2014 in Amsterdam.

**March 2014:** High Resolution Sedimentology and Digital Outcrop Analog Modeling of the Late Triassic Minjur and Early Jurassic Marrat Formations: Implication to Sequence Development and Reservoir Architecture, Central Saudi Arabia. Presented as poster in the international GEO 2014 conference in Bahrain.

**April 2013:** Sedimentology and Stratigraphy of the Late Triassic Minjur and Early Jurassic Marrat Formations: Implication to Sequence Development and Reservoir Architecture, Central Saudi Arabia. Oral presentation during the 10th Meeting of the Saudi Society for Geosciences.

## **- Publications**

- High Resolution Sedimentology and Digital Outcrop Modelling of the Early Triassic Upper Khartam Member of Khuff Formation, Central Saudi Arabia.

Under preparation to be submitted in Petroleum Geoscience Journal in July 2014.

- Inter-well Scale Heterogeneity of the Upper Khuff Reservoir Units from an equivalent outcropping strata, Central Saudi Arabia.

Under preparation to be submitted to GeoArabia in July 2014.

## **- Additional Information**

### **• Languages:**

- Arabic: Mother Tongue.
- English: very good written and spoken.

### **• Computer Knowledge:**

- Master some of the useful geological software's such as; surfer, ArcGIS, Coreldraw, VRGS and Polyworks.
- Experienced user of Microsoft Office Products and many other applications.
- Keen user of the Internet.

## **References:**

Available on Request.